LBL-27246

Lawrence Berkeley Laboratory
UNIVERSITY OF CALIFORNIA

Physics Division

Two Jet Differential Cross Section and Structure Functions in $\bar{p}p$ Collisions at $\sqrt{s}$ = 1.8 TeV

R.M. Harris
(Ph.D. Thesis)

August 1989

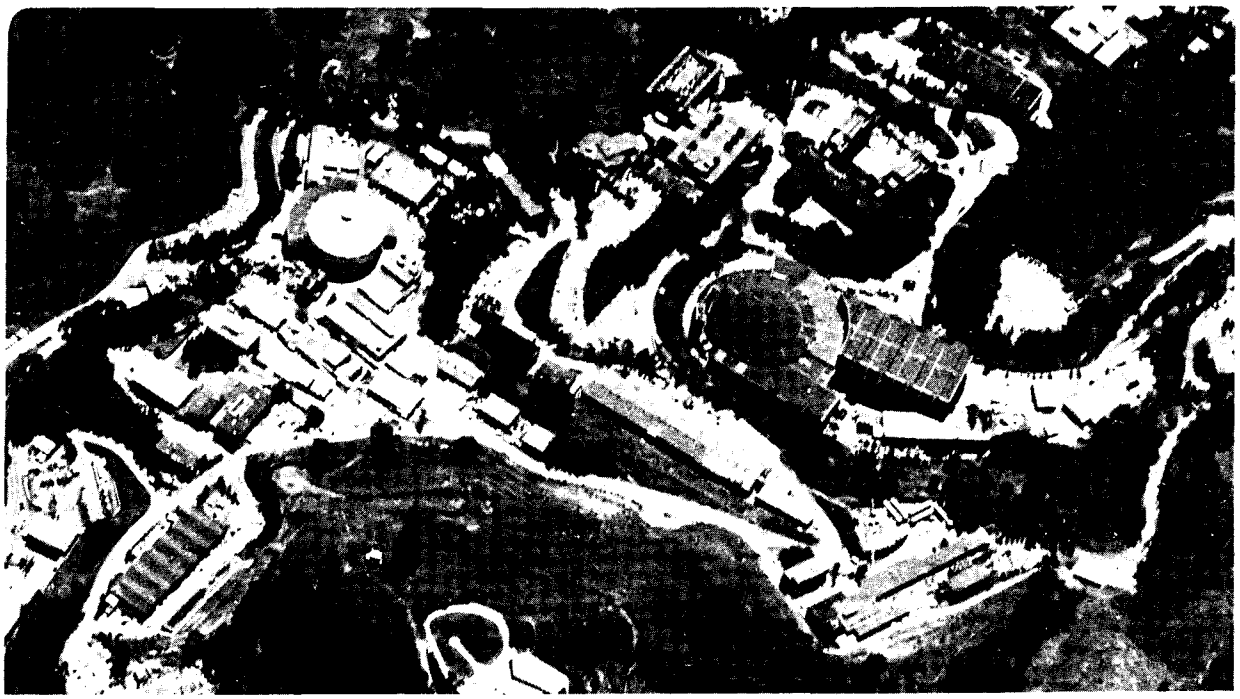

Prepared for the U.S. Department of Energy under Contract Number DE-AC03-76SF00098.

DISCLAIMER

LBL-27246

Two Jet Differential Cross Section and Structure Functions in $\bar{p}p$ Collisions at $\sqrt{s} = 1.8$ TeV.

Robert M. Harris
(Ph.D. Thesis)

Department of Physics
University of California at Berkeley
and
Physics Division
Lawrence Berkeley Laboratory
1 Cyclotron Road
Berkeley, California 94720

August 1989

This work was supported by the Director, Office of Energy Research, Office of High Energy and Nuclear Physics, Division of High Energy Physics of the U.S. Department of Energy under Contract Number DE-AC03-76SF00098.

Two Jet Differential Cross Section and Structure Functions in $\bar{p}p$ Collisions at $\sqrt{s} = 1.8$ TeV.

Robert M. Harris

Two Jet Differential Cross Section and Structure Functions in $\bar{p}p$ Collisions at $\sqrt{s} = 1.8$ TeV.

by
Robert M. Harris

Abstract

Data from the 1987 run of the Collider Detector at Fermilab has been used to measure the two jet differential cross section $d^3\sigma/dE_t d\eta_1 d\eta_2$ in proton antiproton collisions at $\sqrt{s} = 1.8$ TeV. For this measurement, one jet was restricted to the central region $|\eta_1| < 0.6$, where η_1 and η_2 are the pseudorapidity of the two jets with largest transverse energy in the event, and E_t is the transverse energy of the centrally produced jet. Leading order QCD and the similarity of subprocess scattering angular distributions in a modified "single effective subprocess" approximation have been used to extract the "proton effective structure function" in parametric form. Using lowest order QCD, and quark and anti-quark structure functions evolved from deep inelastic scattering measurements, the gluon structure function of the proton has been estimated from the measured two jet differential cross section. The two jet differential cross section, effective structure function, and gluon structure function from CDF are all in agreement with the predictions of lowest order QCD and structure functions evolved from deep inelastic scattering measurements.

Acknowledgements

I would like to thank the entire Lawrence Berkeley Laboratory group of the CDF collaboration for their suggestions and help. In particular, Michael Gold for his patient help in the development of the maximum likelihood E_t and η_2 smearing method, and Jim Siegrist for his enthusiasm and support throughout the course of this analysis. I would also like to thank Hans Jensen for suggesting this analysis topic, my advisor William Chinowsky for guiding me towards using the likelihood method, and Ian Hinchliffe for his help with the details of QCD calculations. This thesis would not have been possible without the efforts of the CDF collaboration, in particular the important work of David Brown, Steve Kuhlmann and Rick St. Denis.

A special acknowledgement goes to my wife Deborah, who left Cornell and came to U.C. Berkeley so we could be together while I worked on this thesis. For this, and much more, I thank her.

My most important acknowledgement is for the love and support of my father, Laurence Harris, who has inspired and encouraged me in all intellectual pursuits.

THE CDF COLLABORATION

F.Abe[p], D.Amidei[c], G.Apollinari[k], G.Ascoli[g], M.Atac[d], P.Auchincloss[n], A.R.Baden[f], A. Barbaro-Galtieri[i], V.E.Barnes[l], F.Bedeschi[k], S.Belforte[k],G.Bellettini[k], J.Bellinger[q], J.Bensinger[b], A.Beretvas[n],P.Berge[d], S.Bertolucci[e],S.Bhadra[g], M.Binkley[d], R.Blair[a], C.Blocker[b], J.Bofill[d], A.W.Booth[d], G.Brandenburg[f], D.Brown[f], A.Byon[l], K. L. Byrum[q], M. Campbell[c], R.Carey[f], W.Carithers[i], D.Carlsmith[q], J.T.Carroll[d], R.Cashmore[d], F.Cervelli[k], K.Chadwick[d,l], T.Chapin[m], G.Chiarelli[k], W.Chinowsky[i], S.Cihangir[o], D.Cline[q], D.Connor[j],M. Contreras[b], J.Cooper[d], M.Cordelli[e], M.Curatolo[e], C.Day[d], R.DelFabbro[k], M.Dell'Orso[k], L.DeMortier[b],T.Devlin[n], D.DiBitonto[o], R. Diebold[a], F.Dittus[d], A.DiVirgilio[k], J.E.Elias[d], R.Ely[i], S.Errede[g], B.Esposito[e], A. Feldman[f], B.Flaugher[n], E.Focardi[k], G.W.Foster[d], M.Franklin[f,g], J.Freeman[d], H.Frisch[c], Y.Fukui[h], A.F.Garfinkel[l],P.Giannetti [k], N.Giokaris[m], P.Giromini[e], L.Gladney[j],M.Gold[i], K.Goulianos[m], C.Grosso-Pilcher[c], C.Haber[i], S.R.Hahn[j], R.Handler[q], R.M.Harris[i], J.Hauser[c], T.Hessing[o], R.Hollebeek[j], L.Holloway[g], P.Hu[n], B.Hubbard[i], P.Hurst[g], J.Huth[d], H.Jensen[d], R.P.Johnson[d], U.Joshi[n], R.W.Kadel[d], T.Kamon[o], S.Kanda[p], D.A.Kardelis[g], I.Karliner[g], E.Kearns[f], R.Kephart[d], P.Kesten[b], H.Keutelian[g], S.Kim[p], L.Kirsch[b], K.Kondo[p], U. Kruse[g], S.E.Kuhlmann[l], A.T.Laasanen[l], W.Li[a], T.Liss[c], N.Lockyer[j], F.Marchetto[o], R.Markeloff[q], L. A. Markosky[q], P.McIntyre[o], A.Menzione[k], T.Meyer[o],S.Mikamo[h], M.Miller[j], T.Mimashi[p],S.Miscetti[e], M.Mishina[h], S.Miyashita[p], N.Mondal[q], S.Mori[p], Y.Morita[p], A.Mukherjee[d], C.Newman-Holmes[d],J. Ng[f],L.Nodulman[a], R.Paoletti[k], A.Para[d], J.Patrick[d], T.J.Phillips[f], H.Piekarz[b], R.Plunkett[m], L.Pondrom[q], J.Proudfoot[a], G.Punzi[k], D.Quarrie[d], K.Ragan[j], G.Redlinger[c], J.Rhoades[q], F.Rimondi[d], L.Ristori[k], T.Rohaly[j], A.Roodman[c], A.Sansoni[e], R.Sard[g], V.Scarpine[g], P.Schlabach[g], E.E.Schmidt[d], P.Schoessow[a], M.H.Schub[l], R.Schwitters[f], A.Scribano[k], S.Segler[d], M.Sekiguchi[p],P.Sestini[k], M.Shapiro[f], M.Sheaff[q], M.Shibata[p], M.Shochet[c], J.Siegrist[i], P.Sinervo[j], J.Skarha[q], D.A.Smith[g], F.D.Snider[c], R.St.Denis[f], A.Stefanini[k], Y.Takaiwa[p], K.Takikawa[p], D.Theriot[d], A.Tollestrup[d], G.Tonelli[k], W. Trischuk[f], Y.Tsay[c], F.Ukegawa[p], D.Underwood[a], R.Vidal[d], R.G.Wagner[a], R.L.Wagner[d], J.Walsh[j], T.Watts[n], R.Webb[o], T.Westhusing[g], S.White[m], A.Wicklund[a], H.H.Williams[j], T.Yamanouchi[d], A.Yamashita[p], K.Yasuoka[p], G.P.Yeh[d], J.Yoh[d], F.Zetti[k]

[a] Argonne National Laboratory- [b] Brandeis University- [c] University of Chicago
[d] Fermi National Accelerator Laboratory- [e] INFN, Laboratori Nazionali di Frascati, Italy
[f] Harvard University- [g] University of Illinois- [h] KEK, Japan
[i] Lawrence Berkeley Laboratory-[j] University of Pennsylvania
[k] INFN, University and Scuola Normale Superiore of Pisa, Italy-[l] Purdue University
[m] Rockefeller University- [n] Rutgers University- [o] Texas A&M University
[p] University of Tsukuba, Japan- [q] University of Wisconsin

This work was supported by the U.S. Department of Energy and Lawrence Berkeley Laboratory under Contract DE-AC03-76SF00098.

Contents

List of Tables

List of Figures

Chapter 1

Introduction

Early in the twentieth century, Rutherford *et al.* observed alpha particles elastically scattered by the dense nuclei of gold atoms, which revealed the structure of the atom. Near the middle of the twentieth century, Hofstadter *et al.* observed electrons scattered by protons in helium nuclei, and measured the structure of the nucleus. In the late 1960's and early 1970's, deep inelastic lepton scattering experiments probed the structure of the proton with even more energetic beams of electrons, muons, and neutrinos. They revealed partons within the proton, and partons would later be identified as quarks and gluons. Deep inelastic scattering experiments measured the detailed quark and antiquark structure of the proton, but only indirectly measured its gluon structure. Now, at the end of the twentieth century, the Collider Detector at Fermilab (CDF) has probed the structure of the proton at the highest energy to date. Following the lead of the UA2[1] and UA1[2] experiments at the CERN S$\bar{p}p$S collider, we have collided protons and antiprotons and observed the production of jets of particles that result from parton-parton elastic scattering. In this thesis we report measurements of parton interactions, the "effective" parton structure of the proton, and the gluon structure of the proton. These measurements follow and complement prior elastic scattering measurements at lower energies, and are the precursor to even higher energy measurements at the Superconducting Super Collider, a proposed proton-proton collider for the twenty-

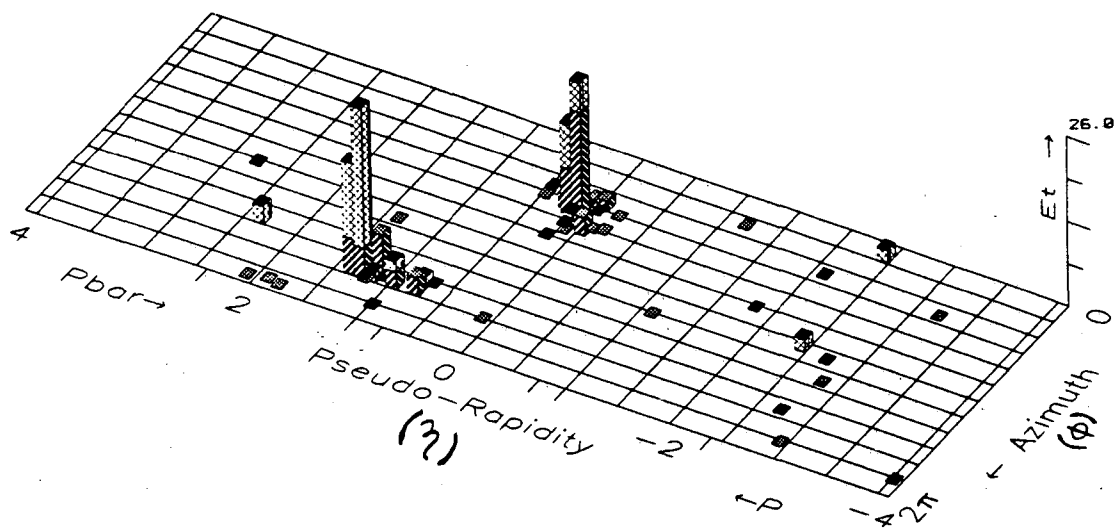

Figure 1.1: A clean two jet event is shown in $\eta\phi$ space in this E_t "lego" plot. The height of each box is transverse energy (E_t) in GeV: the energy of particles measured by CDF calorimeters times the sine of the angle θ with respect to the proton beam. The two large "clusters" of transverse energy in the lego plot are two high E_t jets. The jets result from elastic scattering of partons within the proton and antiproton. The measured jet E_t and η are directly related to the E_t and angle θ of a scattered parton ($\eta \equiv -\ln\tan\frac{\theta}{2}$).

first century.

We measure the interactions of partons by measuring jets of particles. A two jet event, shown in figure 1.1, is the result of parton-parton elastic scattering within a proton-antiproton collision. Two jets are clearly visible in this E_t lego plot. We examine events in which one jet is found in a restricted angular interval at 90° to the proton beam ($\eta_1 \approx 0$), and measure the angular position η_2 of the other jet. By counting the number of such events as a function of angular position and E_t we measure the two jet differential cross section $d^3\sigma/dE_t d\eta_1 d\eta_2$. This cross section is a basic measurement of the scattering probability, which is simply the product of the

probability of partons interacting times the probability of finding a given parton in the proton. This measurement studies both parton interactions and the parton structure of the proton.

In chapter 2 the parton model of proton-antiproton collisions is introduced and we discuss our analysis method. Then, a theoretical calculation of the two jet differential cross section is presented and a simple approximation to the full calculation is discussed. In chapter 3 aspects of the Collider Detector at Fermilab which are relevant to this thesis are described. Particular attention is paid to the calorimeters which measure the energy and trajectory of jets. In chapter 4 the data sample from the 1987 CDF run is described, the calorimeter energy reconstruction is outlined, jets are defined, and important jet energy corrections are given. Also, the event selection procedure is described and simple distributions characterizing the jet event sample are presented. Chapter 5 reports our measurement of E_t and η_2 resolution. Then, the procedure for measuring and correcting for the effect of the resolution on the produced two jet differential cross section is described. Finally, in chapter 6, the two jet differential cross section is presented. The measured and corrected two jet differential cross section is compared to theoretical expectations and good agreement is found. The effective structure function of the proton and an estimate of the gluon structure function of the proton are presented in parametric form, and compared with expectations from deep inelastic lepton scattering. This thesis concludes that high transverse energy jet production in $\bar{p}p$ collisions at $\sqrt{s} =$ 1.8 TeV is well described by theoretical calculations in the parton model.

Chapter 2

Theory

2.1 The QCD Parton Model

2.1.1 Naive Parton Model

The *parton model* [3] is the theoretical framework we use to understand two jet production in proton-antiproton collisions. The basic ideas of the parton model are pictured in figure 2.1. The colliding proton and antiproton are composed of many pointlike particles called *partons*, and there are more than one possible species of parton. A $\bar{p}p$ collision which produces large transverse energy jets is a collision of a single parton in the proton and a single parton in the antiproton. The remaining partons in the proton and antiproton, called *spectator* partons, do not participate in the interaction. The probability of finding a parton of a given species (i) inside the proton (p) is given by the *parton distribution function* f_i^p. The interaction cross section of parton i with parton j is called a *subprocess cross section* and is written $\hat{\sigma}(ij \rightarrow 12)$. The interaction transforms the ingoing partons i and j into the outgoing partons 1 and 2. The outgoing partons 1 and 2 appear as *jets* 1 and 2, which are collections of hadrons obeying approximately the same kinematics as partons 1 and 2. Measurements of the angular and energy distributions of jets, tell us about the parton interaction cross sections $\hat{\sigma}$ and the parton distribution functions of the proton and antiproton.

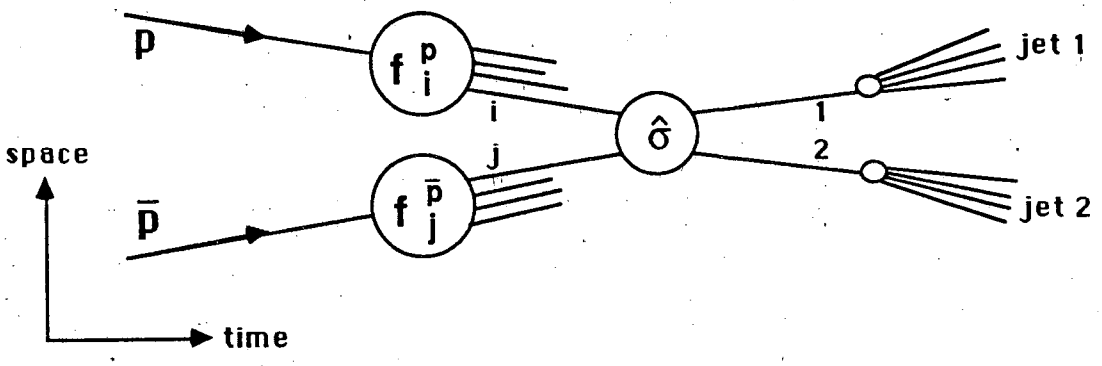

Figure 2.1: The parton model of $\bar{p}p$ collisions in its simplest form. A collision between a proton and antiproton is an interaction between constituent partons i and j, found with probability f_i^p and $f_j^{\bar{p}}$, in which i and j are transformed into partons 1 and 2. Partons 1 and 2 then appear as jets of particles, which we observe in the detector.

The momenta of the proton and antiproton in these collisions are fixed, equal, and opposite, so the lab frame is the center of mass frame of the proton and antiproton. The center of mass energy is $\sqrt{s}$ = 1.8 TeV (1800 GeV). According to the naive parton model, the partons inside the proton and antiproton have approximately zero mass and approximately zero transverse momentum with respect to the beamline. A parton's longitudinal momentum (along the beamline) ranges between zero and the proton momentum. The variable x_p ($x_{\bar{p}}$) is the fractional longitudinal momentum of a parton within the proton (antiproton), and hence ranges between the values zero and one. Thus, the lab frame is not the center of mass frame of the interacting partons. Two body scattering kinematics can be used to determine x_p and $x_{\bar{p}}$ from the angles and energies of the two jets. Then, assuming we know $\hat{\sigma}(ij \rightarrow 12)$, we can use our measured two jet distributions to determine the probability of finding a parton inside the proton (antiproton) as a function of x_p ($x_{\bar{p}}$).

2.1.2 Parton Structure Functions of the Proton

In the naive parton model the probability of finding a parton inside the proton, the parton distribution function f_i^p, is only a function of x_p. A less naive model, using the theory of *quantum chromodynamics* (QCD) [4] for the basic parton interactions, predicts that the probability is also a function of the momentum transfer squared (Q^2) in the interaction. The Q^2 dependence results from gluon *bremsstrahlung*, and is predicted by QCD *evolution* of parton distribution functions [5]. The Q^2 dependence has been observed in both *deep inelastic lepton scattering* (DIS) experiments [6] and in comparisons of $\bar{p}p$ collision experiments [7]. The variation of f_i^p with Q^2 is small compared to the variation with x, so the basic picture of finding a pair of partons which then interact is still reasonable. We use the abbreviated notation

$$f_i(x) = f_i^p(x_p, Q^2) \tag{2.1}$$

for the parton distribution function; $f_i(x)dx$ is the probability of finding a parton (i) inside the proton (p) with fractional momentum between x and $x + dx$ immediately before an interaction with momentum transfer squared Q^2. The i refers to the parton species which, in QCD, are quarks, antiquarks, and gluons. The $SU(3)_{FLAVOR}$ theory of baryon structure [8], predicts that the proton is composed of three *valence* quarks; two up quarks and one down quark. The theory of quantum chromodynamics predicts that the valence quarks in a proton are held together by exchanging gluons, the *gauge bosons* of the QCD $SU(3)_{COLOR}$ symmetry. DIS experiments indicate that about half of the momentum of the proton is carried by gluons. In addition to valence quarks and gluons, the proton contains *sea* quarks and *sea* anti-quarks originating from the Dirac sea of virtual quark-antiquark pairs. In the *standard model* [9] of particle physics, the quarks and antiquarks can come in six flavors (up, down, strange, charm, bottom, and top abbreviated by u, d, s, c, b, and t). There is direct evidence for the existence of all flavors of quarks except for the top quark, and all existing flavors should contribute to the sea, though u and d are by far the most prevalent.

The parton distribution functions of the proton are simply related to the parton distribution functions of the antiproton by charge conjugation invariance and the charge independence of quantum chromodynamics

$$f_i^{\bar{p}} = f_{\bar{i}}^{p} \tag{2.2}$$

where the index i runs over six quarks, six antiquarks and the gluon (the gluon is its own antiparticle in the above expression). Henceforth, when we refer to a parton distribution function we mean that of the proton, and we drop the superscript p. Multiplying $f_i(x)$ by the fractional momentum x we obtain the *parton structure functions*. We use upper case letters for parton structure functions and lower case letters for parton distribution functions. The quark and antiquark structure functions are

$$Q_i(x) = x f_i(x) \quad where \quad i = u, \bar{u}, d, \bar{d}, s, \bar{s}, c, \bar{c}, \ldots \tag{2.3}$$

and the gluon structure function is

$$G(x) = x f_g(x). \tag{2.4}$$

We shall also use the abbreviated notation $Q(x)$ (not to be confused with Q^2) for the sum of quark structure functions and $\overline{Q}(x)$ for the sum of antiquark structure functions

$$Q(x) = \sum_i Q_i(x) \quad where \quad i = u, d, s, c, \ldots$$
$$\overline{Q}(x) = \sum_i Q_i(x) \quad where \quad i = \bar{u}, \bar{d}, \bar{s}, \bar{c}, \ldots .$$

A convenient quantity for simplifying QCD calculations (section 2.3.2) is the *proton effective structure function*

$$F(x) = G(x) + \frac{4}{9}(Q(x) + \overline{Q}(x)). \tag{2.5}$$

There currently exist a number of different algorithms for predicting $f_i(x, Q^2)$ for any i, x and Q^2. These algorithms start with structure functions

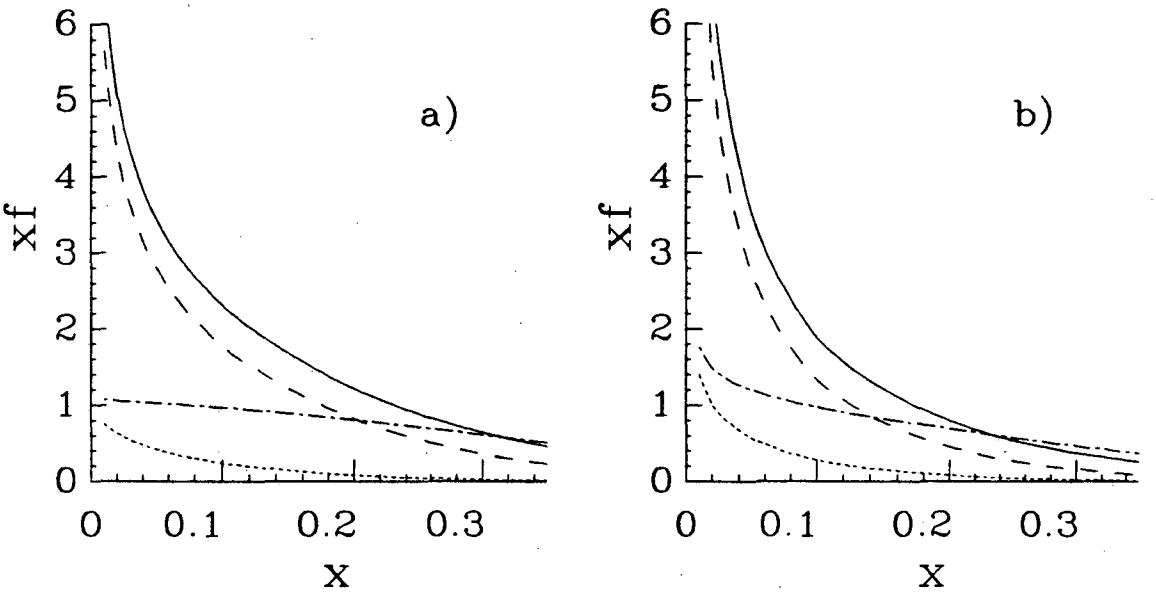

Figure 2.2: Example structure function predictions from EHLQ set 1. The structure functions $G(x)$ (dashes), $Q(x)$ (dot-dash), $\overline{Q}(x)$ (dots), and $F(x) = G(x) + \frac{4}{9}(Q(x) + \overline{Q}(x))$ (solid) are shown for **a)** $Q^2 = 50$ GeV^2 and **b)** $Q^2 = 5000$ GeV^2.

measured in DIS experiments and evolve them to higher Q^2. Commonly used algorithms are those of Eichten-Hinchliffe-Lane-Quigg (EHLQ[10]) and Duke-Owens (DO[11]), deduced from experimental data available up to the early 1980's, and using lowest order QCD evolution. The recently produced algorithms of Diemoz-Ferroni-Longo-Martinelli (DFLM[12]) and Martin-Roberts-Stirling (MRS[13]), were deduced from newer experimental data, and use next to lowest order QCD evolution. These algorithms give the quark and antiquark structure functions with a systematic uncertainty of $\sim 10\%$. The uncertainty on the gluon structure function, $G(x)$, is much larger. This is because DIS experiments use weak and electromagnetic probes which do not couple directly to gluons; they only measure the gluon structure function indirectly[14] via its contribution to the quark and antiquark sea.

In figure (2.2) we show example structure functions from EHLQ for two values of Q^2: low Q^2 at which they were measured, and high Q^2 typical of CDF jet events. Note that the evolution of the structure functions over this large range of Q^2 is small compared to the variation of the structure functions with x. In the majority

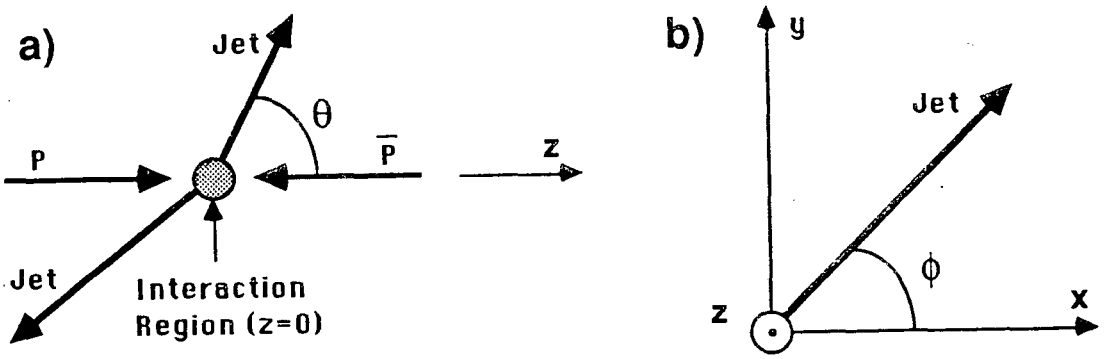

Figure 2.3: The laboratory coordinate system for $\bar{p}p$ collisions. **a)** The z-axis and polar angle θ. **b)** The transverse plane and azimuthal angle ϕ.

of CDF two jet events the ingoing partons have x between .05 and .15, a region in which figure (2.2) predicts that the gluon structure function is dominant. The large gluon structure function, combined with increased probability of gluon interactions (gluons have more color charge than quarks), leads to the QCD prediction that the majority of two jet events observed at CDF are from gluon-gluon and gluon-quark interactions. This allows us to make a direct measurement of the gluon structure function.

2.1.3 Pseudorapidity and Transverse Energy

The lab coordinate system is shown in figure 2.3. The lab frame variables *transverse momentum*

$$P_t = P \sin\theta \tag{2.6}$$

and *rapidity*

$$y = \frac{1}{2} \ln\left(\frac{E + P_Z}{E - P_Z}\right) \tag{2.7}$$

and azimuthal angle ϕ are used to characterize the kinematics of each jet in the $2 \rightarrow 2$ process of two jet production.

These variables are convenient for a number of reasons:

- They have very simple Lorentz transformation properties. P_t and ϕ are invariant under a Lorentz transformation along the z-axis. The rapidity in the

primed frame, moving with velocity βc along the z-axis, is

$$y' = y + \tanh^{-1}(\beta) \tag{2.8}$$

and hence the difference between two rapidities is invariant under a Lorentz boost along the z-axis. This implies that the differential dy is invariant under a Lorentz boost.

- The Lorentz invariant phase space element is

$$\frac{d^3P}{E} = P_t dP_t dy d\phi. \tag{2.9}$$

Each of the differential elements dP_t, dy, and $d\phi$ are Lorentz invariant. Structure functions are clearly not Lorentz invariant, and will cause the two jet differential cross section to fall with increasing $|y|$.

- The locus of points in $y\phi$ space of a particle having constant transverse momentum with respect to a jet axis and constant transverse momentum with respect to the z-axis is approximately a circle in $y\phi$ space. Thus a natural method of clustering particles into a jet is to collect all the particles inside a cone of radius $\alpha = \sqrt{(\Delta y)^2 + (\Delta\phi)^2}$, or equivalently all the energy within that cone. For this reason, the CDF calorimeters were segmented in approximately fixed units of y and ϕ, and hence rapidity is an experimentally convenient variable to work with.

Let E be the total energy of an outgoing parton. Then its transverse energy E_t is defined as

$$E_t = E \sin\theta \approx P_t \tag{2.10}$$

and its pseudorapidity is defined as

$$\eta = -\ln tan\frac{\theta}{2} \approx y. \tag{2.11}$$

Energy and polar angle θ are easy to measure, making E_t and η more convenient variables than P_t and y, and for massless partons they are equivalent. Considering

Variables	Comment
16	Four fourvectors of the $2 \rightarrow 2$ process
-4	Initial two partons have $P_x = P_y = 0$
-4	All four partons are massless.
-4	Conservation of total fourvector
-1	Azimuthal symmetry of collision
3	Remaining independent kinematic variables

Table 2.1: The kinematics of a $2 \rightarrow 2$ process in the parton model.

the high energies of the jets we measure compared to the low mass of the partons, this relativistic approximation is valid. Henceforth when we refer to the variables E_t and η, the theoretically inclined reader should feel free to make the mental substitutions $E_t = P_t$ and $\eta = y$.

2.1.4 Kinematics

For a $2 \rightarrow 2$ process, in which the incoming massless partons have no transverse momentum with respect to the z-axis and the outgoing partons are also massless, the kinematics are completely specified by three independent variables. The kinematic accounting is given in table 2.1.

We chose the transverse energy of the outgoing partons E_t, the pseudorapidity of one outgoing parton η_1 and the pseudorapidity of the other outgoing parton η_2, as the three lab frame kinematic variables to completely characterize the $2 \rightarrow 2$ process. As discussed in section 2.1.3 these variables are experimentally practical, being most naturally suited to our measuring apparatus. They are also theoretically interesting, revealing the rapid decrease of structure functions with x. In terms of these three variables the parton fractional momenta are

$$x_p = \frac{E_t}{\sqrt{s}}(e^{\eta_1} + e^{\eta_2}) \tag{2.12}$$

$$x_{\bar{p}} = \frac{E_t}{\sqrt{s}}(e^{-\eta_1} + e^{-\eta_2}). \tag{2.13}$$

The subprocess center of mass energy squared, $\hat{s}$, is related to the proton-antiproton

center of mass energy squared, s, by

$$\hat{s} = s x_p x_{\bar{p}}. \tag{2.14}$$

Define

$$\eta^* = \frac{1}{2}(\eta_1 - \eta_2) \tag{2.15}$$

which is related to the subprocess center of mass scattering angle θ^* by

$$\sin\theta^* = \frac{1}{\cosh\eta^*}. \tag{2.16}$$

In the parton subprocess center of mass the outgoing partons have momentum p^*. Let the initial state fourvectors be p_i and p_j, and the final state four vectors be p_1 and p_2. The subprocess Mandelstam variables are given below as a function of four vectors. We also give equivalent expressions using center of mass variables p^* and θ^*, and equivalent expressions using our chosen lab variables E_t, η_1 and η_2.

$$\begin{aligned}
\hat{s} \equiv (p_i + p_j)^2 = &\quad (2p^*)^2 &&= 4{E_t}^2\cosh^2\eta^* \\
\hat{t} \equiv (p_i - p_1)^2 = &\quad -2(p^*)^2(1-\cos\theta^*) &&= -2{E_t}^2(\cosh^2\eta^*)(1-\tanh\eta^*) \\
\hat{u} \equiv (p_j - p_1)^2 = &\quad -2(p^*)^2(1+\cos\theta^*) &&= -2{E_t}^2(\cosh^2\eta^*)(1+\tanh\eta^*)
\end{aligned} \tag{2.17}$$

The Mandelstam variables obey the simple relation

$$\hat{s} + \hat{t} + \hat{u} = 0. \tag{2.18}$$

A useful angular variable is

$$\chi = \frac{\hat{u}}{\hat{t}} = e^{(\eta_1 - \eta_2)}. \tag{2.19}$$

Using equations (2.18) and (2.19) it is easy to show that the $t-channel$ gluon exchange angular distribution (combined with a $\hat{t} \leftrightarrow \hat{u}$ interchange term because final state jets are indistinguishable) is written as

$$\frac{1}{2}\left(\frac{\hat{s}^2+\hat{u}^2}{\hat{t}^2} + \frac{\hat{s}^2+\hat{t}^2}{\hat{u}^2}\right) = \chi^2 + \chi + 1 + \chi^{-1} + \chi^{-2} \equiv J_t(\chi). \tag{2.20}$$

2.1.5 Lowest Order QCD

The subprocess cross sections and the evolution of the structure functions with Q^2 are predicted by perturbative quantum chromodynamics (QCD). The Feynman rules, for calculating the cross section in terms of a perturbation expansion in the strong coupling α_s, are determined from the QCD Lagrangian[15]. This is analogous to perturbative quantum electrodynamics (QED)[16]. However, unlike QED, QCD is a *non-abelian* field; consequentially, for low energy interactions α_s is large and the perturbation expansion diverges. Fortunately, non-abelian theories possess the property of *asymptotic freedom*[17]: as the Q^2 of the interaction increases the coupling decrease until the quarks and gluons are only weakly bound to each other (asymptotically free). For our jet events $\alpha_s \approx .1$, so it is plausible that the perturbation expansion converges, though whether it does converge is not presently known. Theoretical ignorance of higher order terms in the perturbation expansion is generally represented by an ambiguity in the Q^2 scale at which α_s is evaluated. We choose the definition $Q^2 = {E_t}^2$. In appendix A.2 we give an expression for α_s as a function of Q^2 and discuss the uncertainty in the Q^2 scale.

The lowest order expressions for the subprocess cross sections have been calculated[18] for all contributing Feynman diagrams, shown in figure 2.4. The results of the calculation are given in table 2.2 for both distinguishable partons and indistinguishable jets.

2.1.6 QCD Radiation and Higher Order Processes

In previous sections we have treated two jet production as originating exclusively from a $2 \rightarrow 2$ process. This is approximately correct, however there are some important exceptions which modify the basic parton model of figure (2.1) to look more like figure (2.5). The basic $2 \rightarrow 2$ interaction, or *hard scatter*, is a QCD interaction. In QCD the interacting quarks and gluons can radiate gluons in both the initial state, before the hard scatter, and in the final state, after the hard scatter. The frequency of occurrence of this *initial and final state QCD radiation*

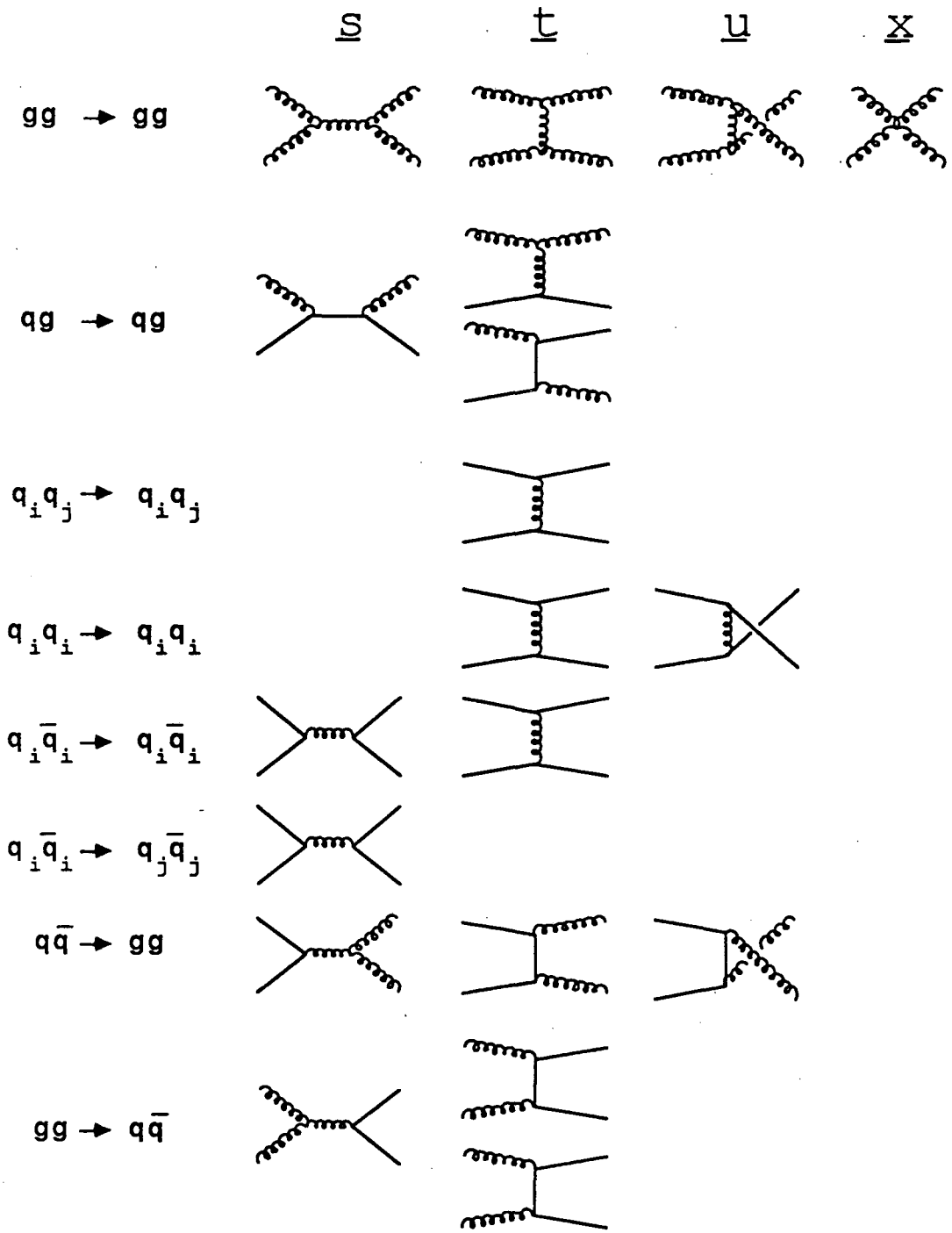

Figure 2.4: Lowest order QCD Feynman diagrams for all contributing subprocesses (gluon-gluon, quark-gluon and quark-quark interactions). Rows are distinct subprocesses and columns are s, t, u and x channel contributing diagrams.

Parton Subprocess ($i \neq j$)	Differential Cross Section $\frac{d\hat{\sigma}}{d\hat{t}} \times \left(\frac{9\hat{s}^2}{8\pi\alpha_s^2}\right)$		
	For Distinguishable Partons		For Indistinguishable Jets
$gg \to gg$	$\left(\frac{9}{4}\right)^2\left[3 - \frac{\hat{u}\hat{t}}{\hat{s}^2} - \frac{\hat{u}\hat{s}}{\hat{t}^2} - \frac{\hat{s}\hat{t}}{\hat{u}^2}\right]$	$\Rightarrow$	$\left(\frac{9}{4}\right)^2\left[J_t(\chi) + 2 - \frac{\chi}{(1+\chi)^2}\right]$
$qg \to qg$	$\left(\frac{9}{4}\right)\left[\frac{1}{2}\frac{\hat{s}^2+\hat{u}^2}{\hat{t}^2} - \frac{2}{9}(\frac{\hat{s}}{\hat{u}} + \frac{\hat{u}}{\hat{s}})\right]$	$\Rightarrow$	$\left(\frac{9}{4}\right)\left[J_t(\chi) + \frac{2}{9}(\chi+3+\chi^{-1})\right]$
$q_iq_j \to q_iq_j$ $q_i\bar{q}_j \to q_i\bar{q}_j$	$\frac{1}{2}\frac{\hat{s}^2+\hat{u}^2}{\hat{t}^2}$	$\Rightarrow$	$J_t(\chi)$
$q_iq_i \to q_iq_i$	$\frac{1}{2}\frac{\hat{s}^2+\hat{u}^2}{\hat{t}^2} + \frac{1}{2}\frac{\hat{s}^2+\hat{t}^2}{\hat{u}^2} - \frac{1}{3}\frac{\hat{s}^2}{\hat{u}\hat{t}}$	$\Rightarrow$	$J_t(\chi) - \frac{1}{3}(\chi+2+\chi^{-1})$
$q_i\bar{q}_i \to q_i\bar{q}_i$	$\frac{1}{2}\frac{\hat{s}^2+\hat{u}^2}{\hat{t}^2} + \frac{1}{2}\frac{\hat{t}^2+\hat{u}^2}{\hat{s}^2} - \frac{1}{3}\frac{\hat{u}^2}{\hat{s}\hat{t}}$	$\Rightarrow$	$J_t(\chi) - \frac{1}{3}(\chi-1+\chi^{-1}) + \frac{\chi^2+1}{(\chi+1)^2}$
$q_i\bar{q}_i \to q_j\bar{q}_j$	$\frac{1}{2}\frac{\hat{t}^2+\hat{u}^2}{\hat{s}^2}$	$\Rightarrow$	$\frac{\chi^2+1}{(\chi+1)^2}$
$q\bar{q} \to gg$	$\frac{4}{3}(\frac{\hat{t}}{\hat{u}} + \frac{\hat{u}}{\hat{t}}) - 3\frac{\hat{t}^2+\hat{u}^2}{\hat{s}^2}$	$\Rightarrow$	$\frac{4}{3}(\chi+\chi^{-1}) - 3\frac{\chi^2+1}{(\chi+1)^2}$
$gg \to q\bar{q}$	$\frac{3}{16}(\frac{\hat{t}}{\hat{u}} + \frac{\hat{u}}{\hat{t}}) - \frac{27}{64}\frac{\hat{t}^2+\hat{u}^2}{\hat{s}^2}$	$\Rightarrow$	$\frac{3}{8}(\chi+\chi^{-1}) - \frac{27}{32}\frac{\chi^2+1}{(\chi+1)^2}$

Table 2.2: Lowest order QCD subprocess cross sections for all contributing subprocesses. The result for distinguishable partons is expressed in terms of Mandelstam variables. The result for jets is expressed in terms of χ and the $t-channel$ angular distribution $J_t(\chi) = \chi^2 + \chi + 1 + \chi^{-1} + \chi^{-2}$. Measuring jets we do not distinguish between parton species in the final state, so we have added $(\hat{t} \leftrightarrow \hat{u})$ terms in the subprocesses with different final state partons.

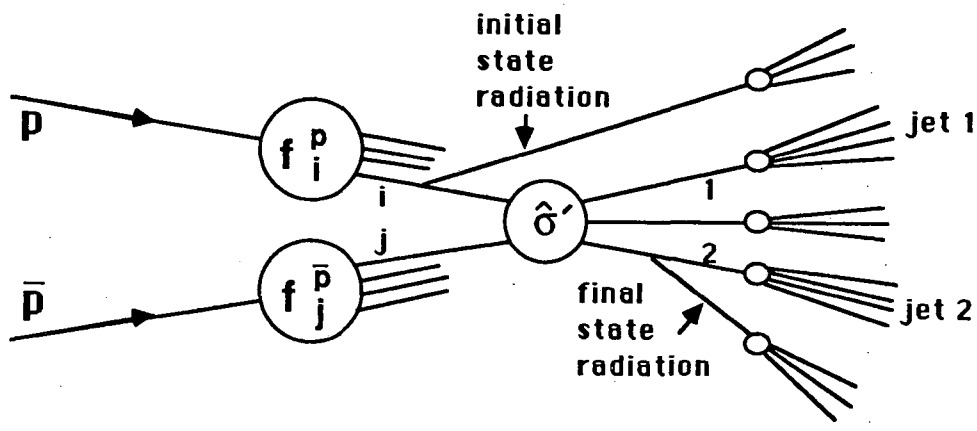

Figure 2.5: The parton model of $\bar{p}p$ collisions, schematically modified to account for energetic *initial state radiation*, energetic *final state radiation*, and *higher order processes* (such as $2 \rightarrow 3$, or $2 \rightarrow 4$, etc.). The final state picture can become quite complicated, but the $2 \rightarrow 2$ process is still dominant.

falls sharply with the transverse momentum $p_\perp$ of the radiated gluon with respect to the parent parton direction. In addition, there can be one or more extra partons produced within the hard scatter itself, in which case we are dealing with parton subprocesses of the form $2 \rightarrow 3$, $2 \rightarrow 4$, etc. Energetic *higher order processes* are rare compared to the basic $2 \rightarrow 2$ interaction of partons. As a very crude rule of thumb they are produced with relative frequency α_s^n where n is the number of partons in the final state minus 2. The dividing line between initial and final state gluon radiation and hard higher order processes is theoretically and experimentally ambiguous. For ease of discussion we may refer to their combined effect as QCD *deviations from* $2 \rightarrow 2$ *production.*

2.2 Analysis Method

We want to measure the two jet differential cross section

$$\frac{d^3\sigma}{dE_t d\eta_1 d\eta_2} \tag{2.21}$$

where one jet is near $\eta_1 \approx 0$ ($\theta \approx 90°$) and the other jet is anywhere within the detector. We do this to study the basic $2 \rightarrow 2$ interactions of partons and the parton structure functions. The analysis is complicated by the fact that the cross section for a *clean two jet event*, one in which two jets and only two jets are produced, is theoretically and experimentally ambiguous because there is usually some radiation. Most initial state radiation has insufficient $p_\perp$ to reach our detector, and simply goes down the beam pipe. Most final state radiation has insufficient $p_\perp$ to escape association with the outgoing parton's jet. Some of the intial and final state radiation have enough $p_\perp$ to reach the detector and be counted as a separate jet. Generally these jets have little transverse energy E_t, so selecting the two highest transverse energy jets (two leading jets) is a good approximation to the "original" two outgoing partons. The dominant high transverse energy event is *inclusive two jet production*, $\bar{p}p \rightarrow$ jet1 + jet2 + X. Here jet 1 and jet 2 are the two leading jets and X is anything else. As we have indicated, X could be nothing at all, but is more likely to be one or more low E_t jets. Our *analysis method* is to assume that events of the type $\bar{p}p \rightarrow$ jet1 + jet2 + X come predominantly from $2 \rightarrow 2$ interactions, and the effects of QCD deviations from $2 \rightarrow 2$ interactions are small enough to be treated as a perturbation and corrected for in the data.

The observed E_t and η_2 distribution of events of the type $\bar{p}p \rightarrow$ jet1 + jet2 + X, has been interpreted as a convolution of the QCD $2 \rightarrow 2$ subprocess cross sections, structure functions, and E_t and η_2 *resolution functions*. The *resolution functions* contain all deviations from $2 \rightarrow 2$ kinematics present in the data, and hence contain both detector resolution effects and the effects of QCD deviations from $2 \rightarrow 2$ production (section 5.1). The effect of the resolution functions on the original $2 \rightarrow 2$ distributions (section 5.2) has been determined, and the raw data has been corrected to remove this effect. The data has been corrected for the

effects of QCD radiation and higher order processes, as well as the effects of detector resolution. It is this corrected two jet differential cross section which we compare to a lowest order QCD prediction (section 6.1) to study the $2 \rightarrow 2$ interactions of partons and structure functions.

The observed properties of proton-antiproton collisions, and the analysis goal of extracting structure functions, has naturally lead to our chosen analysis method. The observation that the two *leading jets* (highest E_t) in $\bar{p}p$ jet data from UA2[1], UA1[2], and CDF (see section 4.8.4) are primarily 180° apart azimuthally indicates that the $2 \rightarrow 2$ process is dominant. The long smooth tails on these distributions indicate that QCD deviations from $2 \rightarrow 2$ production are present and must be taken into account (see section 5.1), however this radiation is only a perturbation on the basic $2 \rightarrow 2$ kinematics of the events. Our analysis method is different from one which attempts to "cut" events which contain "more than two jets" and study the exclusive process $\bar{p}p \rightarrow$ jet1 + jet2. Cutting events in an unbiased way as a function of E_t and η_2 is very difficult, and there is no theoretical calculation for this exclusive process. Leading order QCD predicts inclusive jet rates, and since we sought to measure a cross section and then extract the structure functions using QCD as the theory of the strong interaction, this analysis measured an inclusive jet rate. The analysis of the inclusive single jet cross section [7] has shown that the inclusive rate for jet production agrees with lowest order $2 \rightarrow 2$ QCD predictions, suggesting that hard higher order processes may be a negligible contribution to the overall rate. In summary, we kept all events with two or more jets and analysed them with a $2 \rightarrow 2$ model, using resolution functions derived from the data to correct for perturbations from this model with were present in the data.

2.3 The Two Jet Differential Cross Section

2.3.1 Lowest Order QCD Calculation

In the parton model, to lowest order in QCD, the cross section[19] for $\bar{p}p \rightarrow$ jet1 + jet2 + X in terms of the three lab frame variables P_t, y_1, and y_2 is

$$\frac{d^3\sigma}{dP_t dy_1 dy_2} = 2P_t \sum_{ij} x_p f_i^p(x_p, Q^2) x_{\bar{p}} f_j^{\bar{p}}(x_{\bar{p}}, Q^2) \frac{d\hat{\sigma}}{d\hat{t}}(ij \rightarrow 12). \qquad (2.22)$$

The sum in equation (2.22) is taken over all parton species (quarks, antiquarks and gluons). The sum also implies a symmetrization under $\hat{t}$ and $\hat{u}$ interchange for non-identical final state partons, necessary because we are calculating the total jet rate and do not distinguish different parton species. The subprocess differential cross sections are given in table 2.2.

The measurement is made in the experimental variables E_t, η_1, and η_2. The assumption of massless partons leads to $E_t = P_t$, $\eta_1 = y_1$, and $\eta_2 = y_2$ at the parton level, relating the QCD prediction directly to the measured jet quantities:

$$\frac{d^3\sigma}{dE_t d\eta_1 d\eta_2} = \frac{d^3\sigma}{dP_t dy_1 dy_2} \qquad (2.23)$$

The primary goal of this analysis is to measure the two jet differential cross section and compare with the expectation of the lowest order QCD calculation given in equation (2.22). A secondary goal is to use the lowest order QCD subprocess differential cross sections and the measured two jet differential cross section to determine parton structure functions.

2.3.2 SES Approximation

The complexity of summing over many different subprocess differential cross sections terms in equation (2.22) makes it appear difficult to extract the parton structure functions from a measurement of the two jet differential cross section. Fortunately however, the parton subprocess cross sections $d\hat{\sigma}/d\hat{t}$ are predicted to be quite similar, and we can approximate leading order QCD with a single effective subprocess (SES) as was first done by Combridge and Maxwell[20].

The angular distributions of the three dominant subprocesses are all dominated by $J_t(\chi)$, as shown in the first three rows of table 2.2. $J_t(\chi)$, defined in equation 2.20, comes from the $t-$ *channel* gluon exchange diagram. If we neglect processes other than those of the first three rows of table 2.2, and neglect angular terms other than $J_t(\chi)$, the magnitudes of the three basic subprocess differential cross sections are a simple geometrical progression

$$qq \to qq : qg \to qg : gg \to gg \approx 1 : \frac{9}{4} : \left(\frac{9}{4}\right)^2 \tag{2.24}$$

Noting this approximation, Combridge and Maxwell introduced the proton effective structure function

$$F(x) = G(x) + \frac{4}{9}(Q(x) + \overline{Q}(x)). \tag{2.25}$$

The motivation for defining $F(x)$ was that $F(x) \times F(x)$ contains the simple geometrical progression of equation (2.24). Combridge and Maxwell then approximated the two jet differential cross section by the *original* SES *approximation*

$$\frac{d^3\sigma}{dP_t dy_1 dy_2} \approx F(x_p)F(x_{\bar{p}})\frac{9\pi\alpha_s^2}{\hat{s}^2}P_t J_t(\chi). \tag{2.26}$$

Note that the sum over subprocesses explicit in equation (2.22) has disappeared into the definition of the proton effective structure function. Equation (2.26) uses the single effective angular distribution $J_t(\chi)$ for all parton subprocesses. This approximation was used by UA1[22] and UA2[23].

The angular distributions for $gg \to gg$, and $qg \to qg$, and $J_t(\chi)$ are plotted as a function of $|\eta_2|$ in figure 2.6. Note that $J_t(\chi)$ underestimates the angular distributions of $gg \to gg$ and $qg \to qg$. This discrepancy is most noticeable at $\eta_2 = 0$. Since $\bar{p}p$ collisions at $\sqrt{s} = 1.8$ TeV are dominated by the two processes $qg \to qg$ and $gg \to gg$ [21], using $J_t(\chi)$ for the single effective angular distribution is not the best idea. The SES approximation is improved by using the $qg \to qg$ angular distribution

$$J(\chi) = J_t(\chi) + \frac{2}{9}(\chi + 3 + \chi^{-1}) \tag{2.27}$$

in place of $J_t(\chi)$ in equation (2.26). This *modified SES approximation*, appropriate

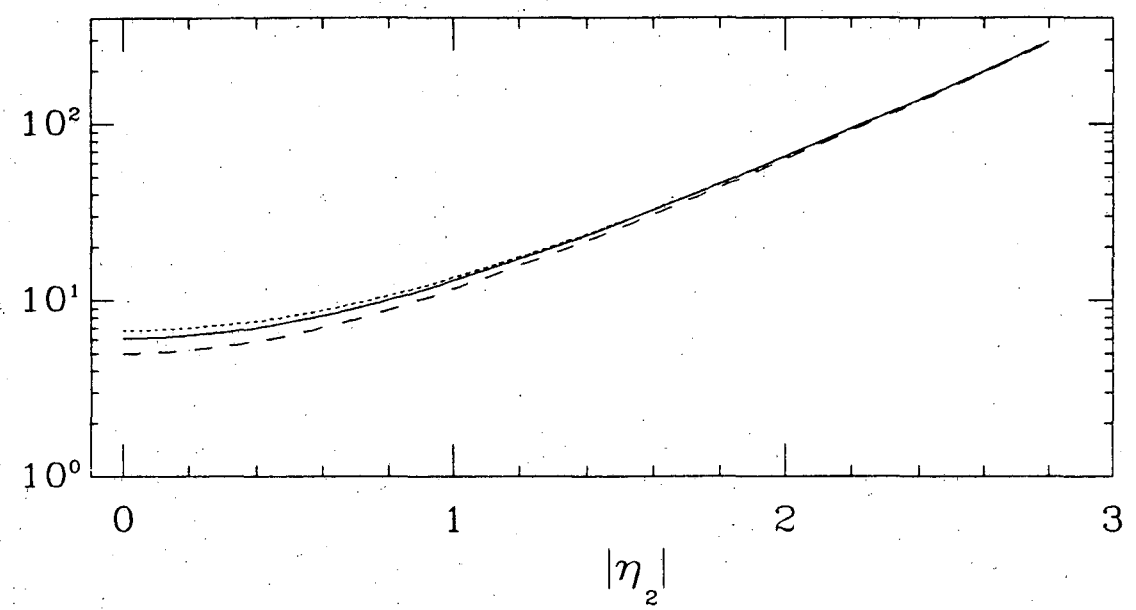

Figure 2.6: Subprocess angular distributions. Here η_2 is the pseudorapidity of the second parton while the first parton is at $\eta_1 = 0$. The dashed curve is $J_t(\chi)$, the solid curve is the $qg \to qg$ angular distribution, and the dotted curve is the $gg \to gg$ angular distribution. Note the similarity of the three distributions over two orders of magnitude.

for the range of x in the CDF data sample, is

$$\begin{aligned} \frac{d^3\sigma}{dP_t dy_1 dy_2} &\approx F(x_p)F(x_{\bar{p}})\hat{\sigma}_{SES}(\bar{p}p \to 12) \\ &\approx F(x_p)F(x_{\bar{p}})\frac{9\pi\alpha_s^2}{\hat{s}^2}P_t J(\chi). \end{aligned} \tag{2.28}$$

The accuracy of this approximation is discussed in appendix A.1. We use the modified SES approximation of equation (2.28) and the parameterization

$$F(x) = \frac{A(1-x)^{P_1}}{x^{P_2}} \tag{2.29}$$

to extract the proton effective structure function, $F(x)$, from the measured two jet differential cross section, as described in section 5.2.2.

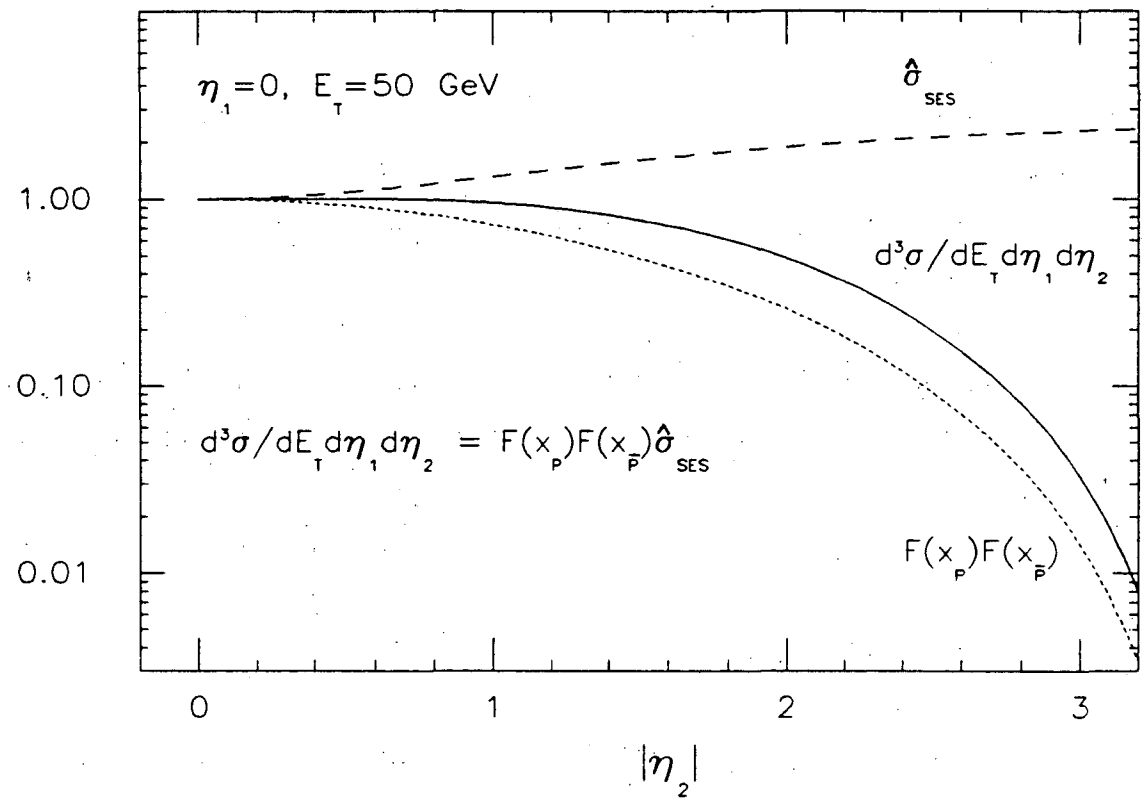

Figure 2.7: The two jet cross section decomposed into a single effective subprocess cross section and an effective structure function product.

2.3.3 Understanding the Two Jet Cross Section

In our measurement, because of trigger conditions and energy measurement considerations, we were only able to accurately measure events where the pseudorapidity of one of the jets was near zero. Specifically, the jet axis was restricted to the pseudorapidity interval $|\eta_1| < 0.6$. For fixed η_1, the two jet differential cross section is a function of the lab variables E_t and η_2. The cross section must fall with increasing E_t, that decrease being caused by both the decrease in the subprocess cross section and the decrease in the structure functions [7]. Figure 2.7 shows the η_2 dependence of the two jet differential cross section, decomposed into the single effective subprocess cross section and the proton effective structure function product. The curves have been normalized to 1 at η_2=0, so that the relative change in the different components of the cross section can be examined.

To obtain figure 2.7 we used equations (2.28), (2.12) and (2.13), with $\sqrt{s} = 1800$ GeV, $E_t = 50$ GeV and $\eta_1 = 0$. The final results of this analysis (see figure 6.6) were used for $F(x)$, so the behavior of the two lower curves is the actual behavior determined by CDF. The behavior is the same if the structure functions from DIS[10,11,12,13] are used.

The dominant feature of figure 2.7 is that the structure functions decrease with increasing $|\eta_2|$, causing the total cross section to decrease with increasing $|\eta_2|$. Equation (2.12) shows that for large η_2 the fractional momentum of one of the partons, x_p, has increased greatly, and the corresponding structure functions have decreased, pulling down the total cross section. It is also true that the fractional momentum of the other parton, $x_{\bar{p}}$, has decreased, though this decrease is slight compared to the relative increase in x_p. Since the subprocess cross section is relatively constant as a function of $|\eta_2|$ (see figure 2.7), the variation of the two jet differential cross section with $|\eta_2|$ is primarily caused by the structure functions.

Chapter 3

Collider Detector at Fermilab

The Collider Detector at Fermilab (CDF) is a multipurpose detector at the Fermilab Tevatron $\bar{p}p$ collider. A perspective view and a side view of CDF is given in figure 3.1. Only the necessary detector components for jet analysis will be described; a description of the complete detector can be found in reference [24]. *Calorimeters*, devices which measure energies and trajectories of particles, were the most important detectors for this analysis. A vertex tracking chamber was used to measure the event vertex, necessary for precise calculation of jet trajectories. The central tracking chamber was used to measure the response of the central calorimeters to low energy charged particles. The beam-beam counters were used in the hardware trigger and were also used to estimate the luminosity. The hardware trigger made the decision during data acquisition (online) to retain an event for later (offline) analysis.

3.1 Sampling Calorimeters with Tower Geometry

This analysis uses the CDF calorimeters to measure the energy and direction of jets. Calorimeters are not the only means available. The most precise measurement of momenta and trajectories of charged particles comes from tracking chambers in magnetic fields. However, to maintain a constant resolution, the size

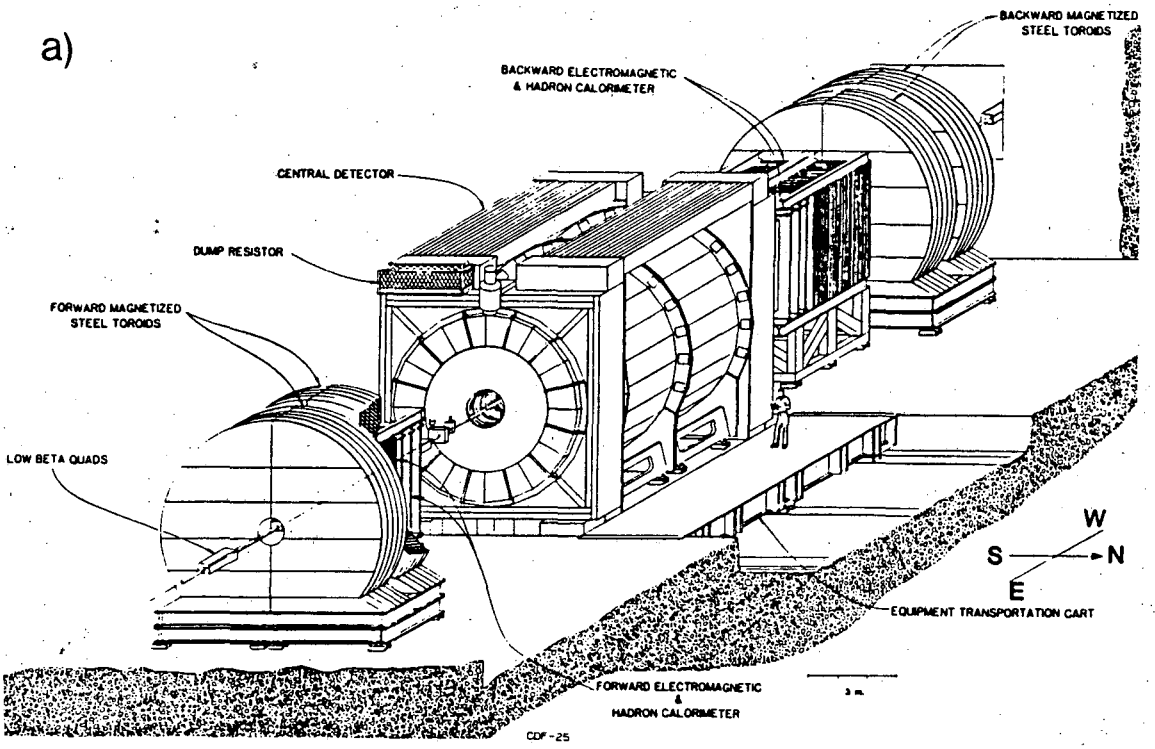

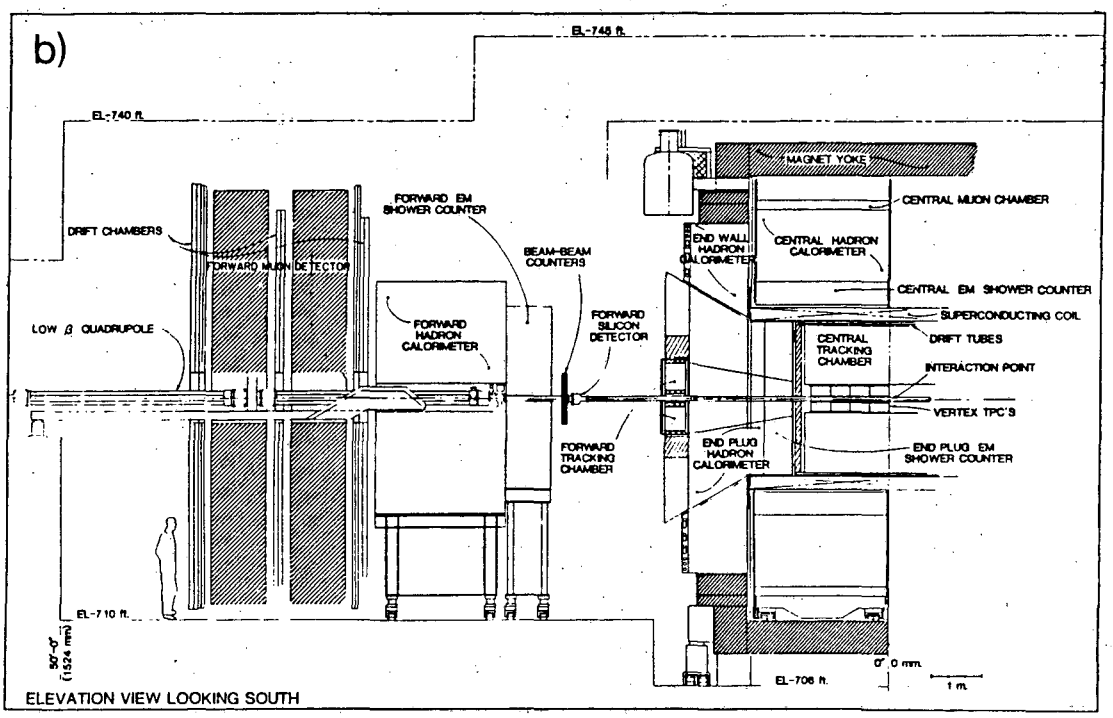

Figure 3.1: Collider Detector at Fermilab. a) Perspective view. b) Side view.

of such devices increase with $\sqrt{E}$ while the size of calorimeters scale with $\ln E$. To measure high energy particles with good resolution requires prohibitively large tracking chambers, yet can be achieved affordably with calorimeters. In addition, calorimeters measure neutral particles which tracking chambers miss. To measure the energy of all high energy particles, which interact electromagnetically or strongly, CDF employs sampling calorimeters.

Sampling calorimeters, as opposed to total absorption calorimeters, only sample a fraction of the energy deposited by an incoming particle. Layers of sampling material are interleaved with layers of absorber in a sandwich. Incoming primary particles produce showers of secondary particles in the absorber. The showers deposit a fraction of their energy in the sampling material, and that energy produces a signal which is registered and summed over all sampling layers. The ratio between this sampled energy signal and the true energy of the incident particle was determined in a *test beam* of particles of known energy, and was later used in the *online calibration* to convert a measured signal to a measured energy. This *initial calibration* was maintained over the course of the experiment.

All the calorimeters at CDF have been designed with projective *towers* which point towards the nominal interaction region, as shown in figure 3.2. By measuring the energy deposited in a projective tower by a particle, we also simultaneously measure the angle at which the particle emerged from the interaction. Each tower is approximately 0.1 units of η . For $|\eta| < 1.3$ the hadron calorimeter towers are 15° degrees in ϕ, and for $|\eta| > 1.3$ all the towers are 5° in ϕ, as shown in figure 3.2b.

The calorimeters at CDF are of two types. Scintillator calorimeters are in the *central* region ($|\eta| < 1.3$) and gas calorimeters are closer to the beam. Scintillator was chosen in the central region for its good resolution. Closer to the beam the towers are smaller in θ (fixed width in η), making the construction of a scintillator calorimeter impractical. In addition, the high multiplicities in the forward direction would age scintillator too quickly. Gas calorimeters are easily segmented into small towers using pads in the cathode plane, and robustly withstand

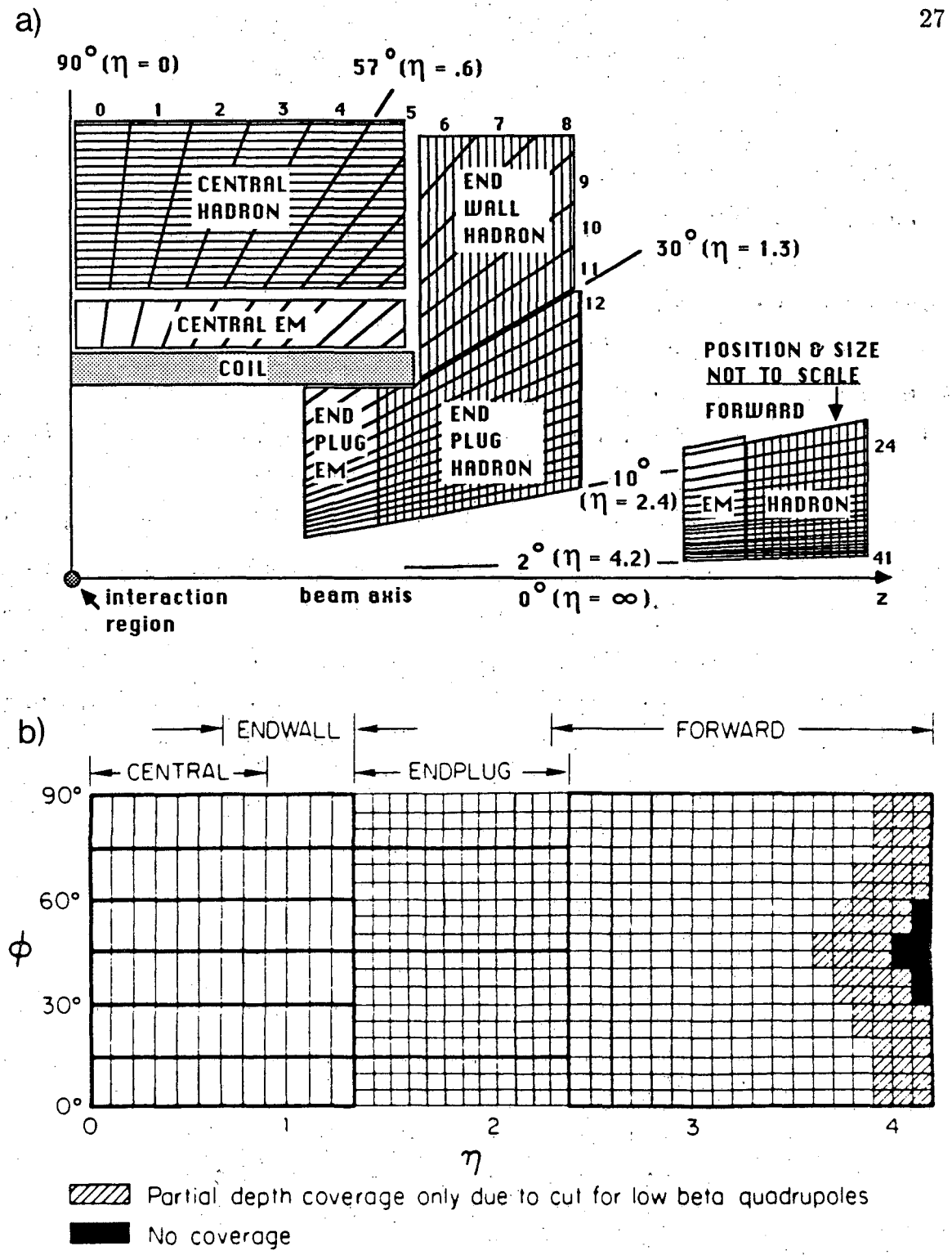

Figure 3.2: CDF Calorimeters **a)** Side view of the CDF calorimeters displaying projective tower geometry and η segmentation. **b)** Schematic $\eta\phi$ segmentation of CDF calorimeters.

high multiplicities, making them a natural choice for the forward region. In addition gas calorimeters are relatively cheap to construct. Unfortunately, gas calorimeters typically have worse resolution than scintillator calorimeters, and are subject to gain variations produced by changing ambient conditions.

The construction and calibration of the CDF calorimeters will be described in the following sections. Years of effort, coming from a large fraction of the collaboration, was spent on achieving and maintaining the calibration of the central calorimeters. A smaller fraction of the collaboration worked tirelessly on the calibration of the gas calorimeters. Unfortunately our understanding of the gas calorimeter calibrations is not as good as our understanding of the central calorimeter calibrations. Both central and gas calorimeters have been employed by this analysis to measure jet directions. Unfortunately, none of the hadronic gas calorimeters participated in the trigger which selected high transverse energy jets. For this reason, and to minimize systematic uncertainties in the jet energy, this analysis used events in which one high E_t jet was in the central calorimeter region. The other high E_t jet in the event could be anywhere within the CDF calorimeters, and only its direction was used.

3.2 Central Calorimeters

3.2.1 Central Electromagnetic Calorimeter (CEM)

Tower Geometry

The CEM[25] is azimuthally arranged in 48 physically separate 15° modules called *wedges*, 24 wedges at positive z and likewise at negative z. Each wedge is segmented into ten towers in η; each tower is 15° in ϕ and approximately 0.11 units of η. Figure 3.2 shows the towers at positive z of the CEM which cover the angular range $90° > \theta > 37°$ ($0.0 < \eta < 1.1$). The towers are numbered 0 through 9 consecutively, where tower 0 is closest to $\theta = 90°$

Construction

The CEM is a sandwich of lead and scintillator layers. It has a thickness for electromagnetic and hadronic showers of approximately eighteen radiation lengths and one interaction length respectively, except for tower 9 which is only ten radiation lengths deep. The beam pipe, tracking systems, and superconducting magnet coil provide an additional 0.9 radiation lengths. The lead-scintillator stack consists of 30 layers of lead sheets (3.2 mm thick and clad on each side with 0.38 mm of aluminum) and 31 layers of plastic scintillator (polystyrene, SCSN-38 [26] 0.5 cm thick). Constant radiation length and sampling fraction as a function of η is achieved by substituting acrylic layers for lead layers; increasing layers of acrylic with increasing $|\eta|$. Only light from scintillator layers behind lead sheets contributes to the observed signal, because the sides of scintillator layers behind acrylic are painted black. A strip chamber at the position of shower maximum improves the position resolution for electrons and photons.

Signal Collection

The signal collection technique is the same for each tower of each module of the CEM. Wavelength shifters receive light from the scintillator and transmit it to light guides which run radially out of the calorimeter to photomultiplier tubes (PMT's) on both sides of each tower as shown in figure 3.3. The rectangular light guides are glued to rectangular-to-round transmission pieces, which pass light to PMT's and also receive calibration light signals. The PMT redundancy, one PMT reading out the "right" side and the other reading out the "left" side as shown in figure 3.3, proved useful in rejecting unphysical signals. The PMT's were tested in an automated procedure [27], and their gain-quantum efficiency product was set to be 1.2×10^4. The PMT response was found to be linear to better than 1%.

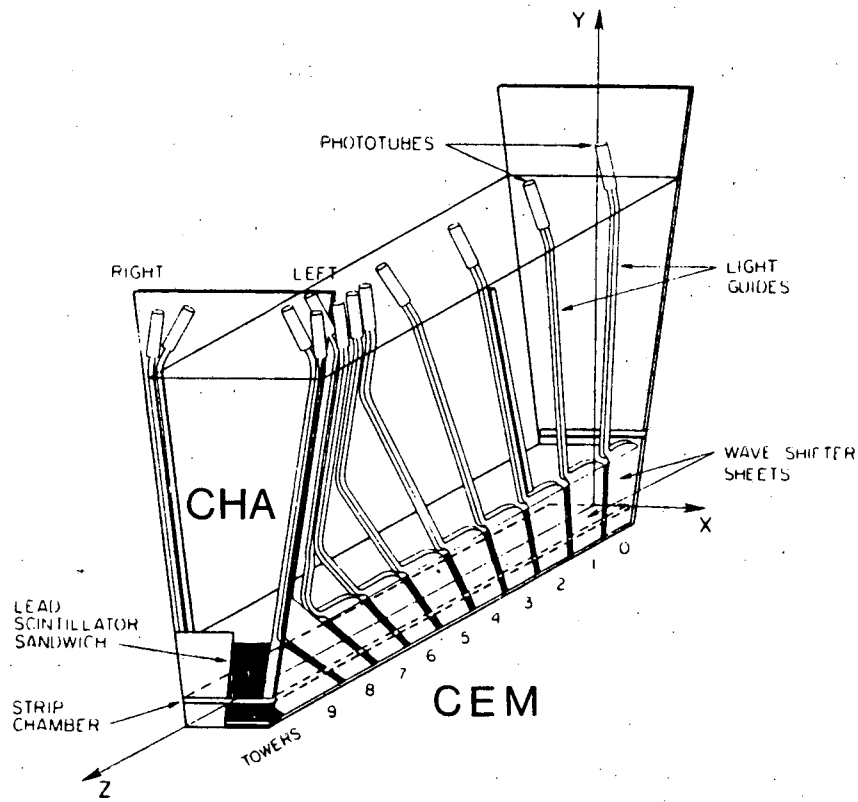

Figure 3.3: Layout of the CEM light-gathering system in a single wedge of the CEM and CHA. The light guides run along the side of the CHA which sits directly above the CEM lead-scintillator sandwich.

Initial Calibration

All modules were initially tested with cosmic rays [28]. Each tower of each module was calibrated with a beam of 50 GeV electrons at the NWest test beam at Fermilab. Electrons beams were used to determine the response and resolution of position, including the phi crack regions (see section 3.2.4). The response of a typical tower to electron beams between 10 and 100 GeV was measured. The electron energy resolution was $\sigma/E = 0.135/\sqrt{E \sin\theta} \pm 0.005$. The $\sin\theta$ term accounts for the decreased total sampling with decreasing $\sin\theta$. The error is the systematic uncertainty in the resolution measurement, caused by uncertainties in the energy of the electron beam.

Maintenance of Calibration

Three separate calibration systems ensure that the initial calibration of the central electromagnetic calorimeter is maintained[29].

1. Cs^{137} Source System. A computer controlled system moves $Cs^{137}\gamma$ point sources across the towers of each module. The sources move parallel to the beam in two brass tubes which straddle the tower centerlines in the eighth scintillator layer. During a source run, PMT currents are recorded at more than 100 lateral positions per tower as the point source traverses the ten towers in a module. The resulting current profiles for each tower are fit to determine the peak current. This measures the combined response of the scintillator, wavelength shifters, light guides and PMT's for each tower. Source runs were performed concurrently with initial testbeam calibration and repeated periodically throughout the experiment. Testbeam calibrations and source runs were repeated one month later on three modules. The ratio of the tower response to 50 GeV electrons and sources was reproduced to 0.4% RMS.

2. Xenon Flasher System. For each module a xenon bulb produces flashes of light illuminating a scintillator rod. The rod is connected to a bundle of quartz

fibers which lead to acrylic prisms mounted on the wavelength shifters for each tower. Three PIN Diodes monitor the light output of the scintillator rod. The ratio of PMT output to PIN diode output measures the response of wavelength shifter, light guides, and PMT to 2% RMS. Results are reproducible to 0.4% RMS over a single day.

3. LED Flasher System. For each module three LED's flash green light into quartz fibers which fan out to the transition pieces between the light guides and PMT's. PIN diodes monitor the output of the LED's. The ratio of PMT output to PIN diode output measures the response of the PMT's to 0.8% RMS. Results are reproducible to 0.3% over a single day. LED outputs were sufficiently stable that the output of the PMT's alone, without reference to PIN diodes, were used for calibrations.

3.2.2 Central and Endwall Hadron Calorimeters (CHA & WHA)

Tower Geometry

The towers of the CHA & WHA[30] combine to form a single hadron calorimeter as shown in figure 3.2. The CHA is directly outside the CEM in the same physical modules (see figure 3.3). The WHA is azimuthally arranged in 24 physically separate modules at positive z mated to corresponding CHA wedges, and likewise at negative z. A single WHA module is shown in figure 3.4a. The CHA and WHA are combined to form twelve towers, each 15° in ϕ and approximately 0.11 units in η as shown in figure 3.2. At positive z the CHA and WHA cover the angular range $90° > \theta > 30°$ ($0.0 < \eta < 1.3$). The towers are numbered 0 through 11 consecutively, where tower 0 is closest to $\theta = 90°$. Towers 0 to 9 are directly outside corresponding towers in the CEM and towers 10 and 11 are outside the first two towers of the endplug electromagnetic calorimeter. Towers 6, 7 and 8 are partly in the CHA and partly in the WHA; the signal for these towers is the sum of the

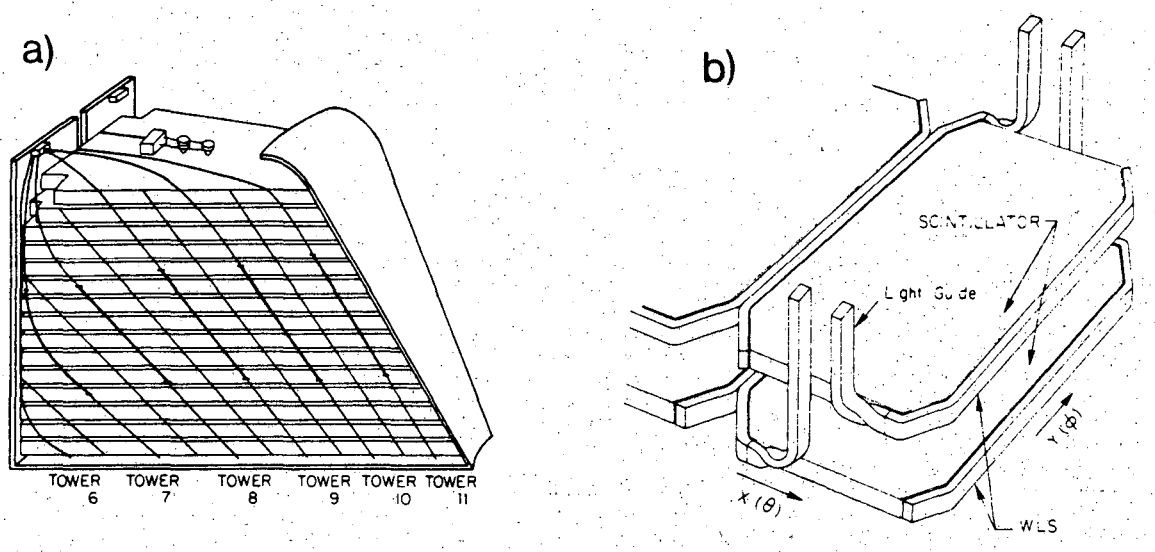

Figure 3.4: **a)** Diagram of one WHA module showing the steel-scintillator sandwich, line sources along the sides of each tower, and movable point source. **b)** Scintillator, wavelength shifter, and light guides of the CHA and WHA.

signals from the CHA and WHA.

Construction

The CHA and WHA are steel-scintillator sandwiches with 1 cm thick plates of acrylic scintillator (PMMA). The CHA consists of 32 layers of 2.5 cm thick steel plates parallel to the beam ($4.7/\sin\theta$ interaction lengths). The WHA consists of fifteen layers of 5.0 cm thick steel plates perpendicular to the beam ($4.5/\cos\theta$ interaction lengths). The CEM, and the endplug electromagnetic calorimeter in front of the CHA and WHA, provides an additional interaction length of hadron sampling.

Signal collection

Signal collection for the CHA and WHA is practically the same as for the CEM. One difference is that the CEM has wavelength shifter on the constant ϕ side of each tower, as shown in figure 3.3, while the CHA and WHA have wave-

length shifter on the constant θ side, as shown in figure 3.4b. Here, light guides on azimuthally opposite sides receive light from alternating θ sides of the scintillator, and transmit the light to "right" and "left" PMT's.

Initial Calibration

The CHA and WHA modules, like the CEM modules, were initially tested with cosmic rays. Each tower of two CHA modules was calibrated with 50 GeV charged pions, and PMT gains were adjusted to yield two picocoulombs per GeV. A "skin source" system, which moved a Cs^{137} point source longitudinally along the tower, produced a calibration current (I_c) in the tower at the adjusted gain. The high voltage of the PMT's in the remaining CHA modules were adjusted to give the calibration current I_c for each tower. Next, all the remaining modules were calibrated with 50 GeV pions in the test beam. Each tower of each CHA module was calibrated to 1% RMS. The calibrations performed with sources correlated with the calibrations performed with pions to 4% RMS.

Since it had been shown that calibrating each module in the test beam was not absolutely necessary, only two WHA modules were calibrated in the test beam. A system of longitudinally positioned Cs^{137} line sources was used to transfer the test beam calibration to the remaining WHA modules. In this way the WHA modules were calibrated to about 4% RMS.

The response of the CHA and WHA to charged pion beams between 10 and 150 GeV was measured and no deviation from linearity was observed for pions which didn't interact in the CEM. This response measurement was used to define the calibration of the CHA and WHA. However, if the pion shower started in the CEM, the total central calorimeter energy response (CEM+CHA) was slightly non-linear, being ~10% low at 10 GeV[31]. The effect of this non-linearity on jet energy measurements is discussed in section 4.4.

The energy resolution of the calorimeter typically depended on the particular tower. For towers 1 to 5 of the CHA the average resolution is $\sigma/E \approx 0.5/\sqrt{E} + 0.04$. For Tower 10 in the WHA the resolution is $\sigma/E \approx 0.7/\sqrt{E} + 0.05$.

The offset in the above resolutions is consistent with a value of e/h between 1.2 and 1.4, as expected for these calorimeters[32]. The slope of the WHA resolution function is larger than the slope of the CHA resolution function by a factor of $\sqrt{2}$, consistent with the expected increase from decreased sampling fraction alone.

Maintenance of Calibration

Many source systems and a single laser system are employed to maintain the calibration of the CHA and WHA.

Source Systems. The CHA and WHA, like the CEM, have computer controlled Cs^{137} source systems to test the response of scintillator, wavelength shifter, light guides and PMT's to sources at a fixed longitudinal depth. The CHA system uses 3 mCi sources in the seventh scintillating layer, while the WHA uses 1.3 mCi sources (schematically shown at the top of figure 3.4a). In addition, longitudinally positioned 3 mCi line sources can be manually inserted into the WHA modules to simultaneously irradiate each layer of each tower (see figure 3.4a). Point β sources can be manually inserted in the transition piece between light guides and PMT's to check the PMT gains. All these source systems were used during the initial calibration stage [30].

The Laser System. The laser system maintains the calibration of the CHA and WHA PMT's. As pictured in figure 3.5, a nitrogen laser beam is split into six beams which travel through quartz fibers to light distribution scintillator disks. The light enters the disk along its axis and uniformly illuminates bundles of optical fibers along the perimeter of the disk. Each optical fiber carries light to a transition piece between light guides and PMT for the calorimeter tower.

3.2.3 Online Calibration

Calibration runs were taken during the course of the 1987 run and the results were stored in a database (the CDFDB [33]). The database was accessed

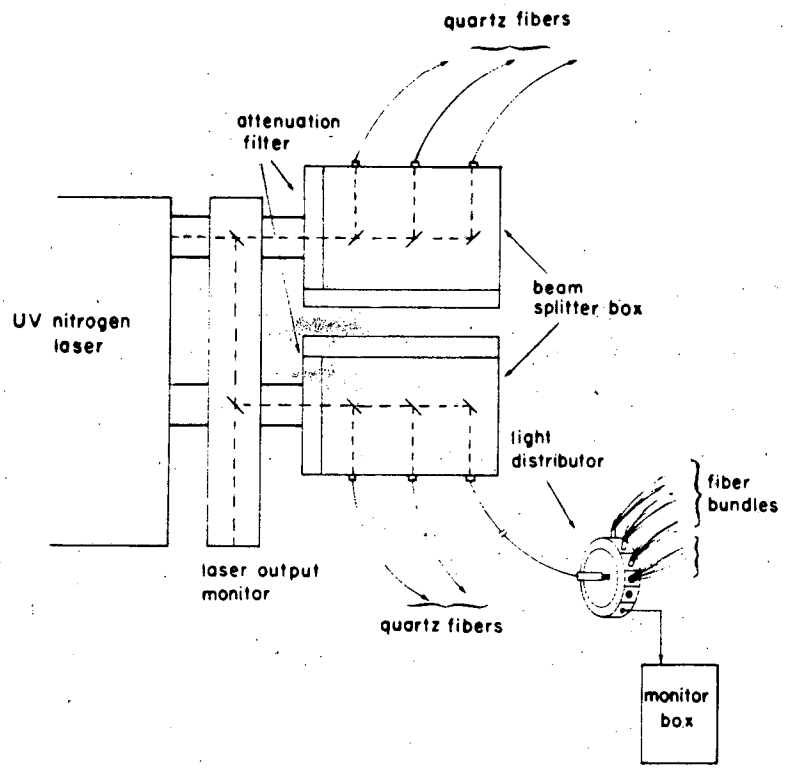

Figure 3.5: The laser calibration system for the CHA and WHA PMT's

by programs that transmitted multiplicative calibration constants to the scanners which read out the front end electronics. The digitized signal, after pedestal subtraction and threshold comparison, was converted to GeV online. To correct the energy scale for long term variations, CEM and CHA Cs^{137} point source calibrations were performed every two to four weeks and WHA line source calibrations every few months. To correct for short term variations in PMT response, CEM LED Flasher and CEM Xenon Flasher calibrations were performed daily and Laser calibrations of the CHA and WHA were performed every few days.

3.2.4 Cracks

Physical design constraints (*e.g.* the mechanical support of the calorimeters) necessarily result in uninstrumented regions. These cracks in the calorimeters are of two types: ϕ cracks and θ cracks. The effect of cracks on the measured E_t of

central jets has been estimated and corrected for.

ϕ Cracks

Each CEM & CHA module is bounded in ϕ by a 0.48 cm thick steel skin. For the CEM, wavelength shifters fit into a 0.64 cm wide gap between the smooth surface of the stack and the steel skin. The gap and skin occupy 0.7° in ϕ of the 15° of the entire tower. For the CHA, light guides fit into a 1.6 cm wide gap between the stack and steel skin. The gap and skin occupy 1.3° in ϕ out of the the 15° of the entire tower.

During test beam calibrations, it was discovered that electromagnetic showers in the CHA light guides were producing Cerenkov radiation, resulting in anomalously large signals (PMT spikes). A uranium radiator of 10 radiation lengths was placed in front of the crack region during the 1987 run, effectively eliminating PMT spikes for incident electrons but not for incident pions. To eliminate these spikes in hadronic showers, an algorithm[34] was developed which used the ratio of the signal in the "right" and "left" phototubes of a tower.

The ϕ cracks were scanned with both electrons and pions in the test beam, and the response of the ϕ cracks was measured in detail. The response of the ϕ cracks to electron and pion beams was ~22% and ~66% of the response in the center of a tower respectively. A detector simulation was tuned to reproduce the response of the ϕ cracks [35]. This simulation was used to determine average jet energy corrections, as described in section 4.4.

θ Cracks

Each CEM module is bounded at $\theta = 90°$ by a one inch steel endplate separated from the lead-scintillator stack by a 5/8 inch support gap, and at $\theta = 38°$ by a two inch thick steel plate separated from the stack by a two inch gap occupied by light guides. At the 90° boundary the gap and steel endplate, and an additional 3/16 inch airgap between east and west wedges on average, form the 90° crack, shown

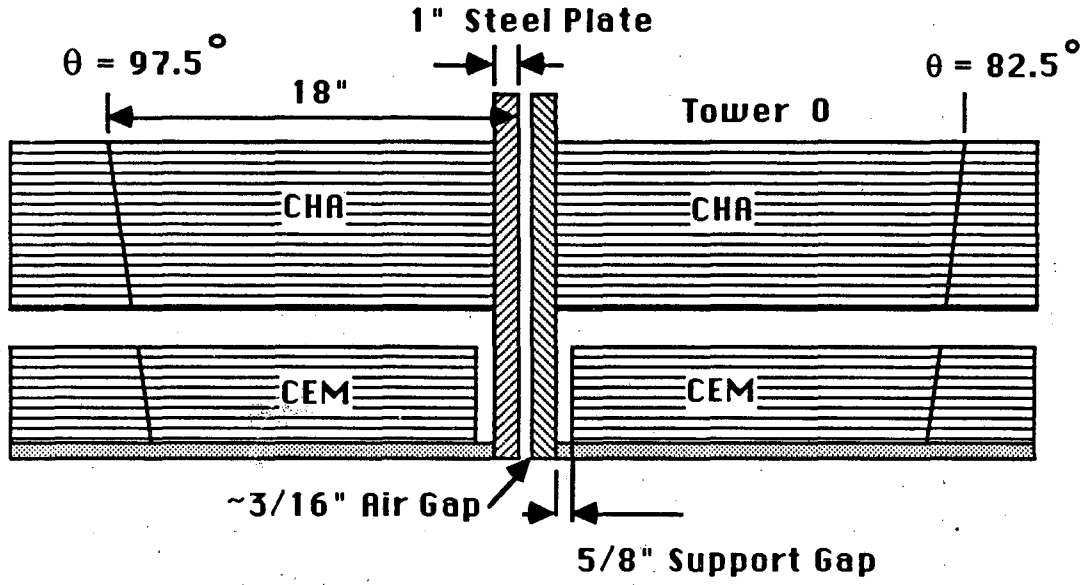

Figure 3.6: The 90° crack, an uninstrumented region near $\theta = 90°$

schematically in figure 3.6. The calorimeters' energy response for jets overlapping the 90° crack was determined from data as discussed in section 4.7.1. At the 38° boundary the gap and steel are the inner edge of a region of complicated response known as the 30° crack. The effects of the 30° crack on this analysis are negligible because we require the trigger jets η centroid to be within $|\eta| < 0.6$ (approximately $58° < \theta < 122°$).

3.3 Gas Calorimeters

All CDF gas calorimeters contain a mixture of 50% argon 50% ethane gas with a small percentage of alcohol added to prevent glow discharge. The gas calorimeters were calibrated in a Fermilab test beam, and that calibration was maintained in the presence of gas gain variations by the CDF gas gain monitoring and calibration system (see Appendix B).

3.3.1 Endplug Electromagnetic Calorimeter (PEM)

Tower Geometry

The PEM[36] is azimuthally arranged in 90° quadrants, four quadrants at positive z and four quadrants at negative z. At positive z the towers cover the angular range $37° > \theta > 10°$ ($1.1 < \eta < 2.4$). The projective towers in the PEM cover 5° in ϕ, and there are sixteen towers segmented in η. The first tower, closest to 37°, is a standard tower of width ~ 0.1 units of η. The next four towers are smaller, each 0.045 units of η, with two towers per standard projective tower. The remaining 11 divisions are each 0.09 units of η. The four small PEM towers are usually combined offline to form two standard towers, giving a total of fourteen standard towers at positive z and likewise at negative z. These towers, numbered 10 to 23, are shown in figure 3.2.

Construction and Signal Collection

The PEM is a sandwich of lead and gas filled proportional tube layers in a cylindrically symmetric gas volume on each side of the interaction region. Four quadrants occupy a single gas volume on one side of the interaction region. Each quadrant's proportional layer is constructed from proportional tubes. Each proportional tube consists of a 52 micron diameter gold plated tungsten wire centered in a resistive plastic tube (60 to 100 KΩ/square). The tubes and wire supports are pictured in figure 3.7a. The tubes have a square cross section, 7.0 mm by 7.0 mm with 0.8 mm thick walls. The tubes span the length of a quadrant. To construct a proportional layer for a quadrant, approximately 156 tubes were laid side by side and sandwiched by a pair of 1.6 mm thick copper clad G-10 panels, as pictured in figure 3.7b. The wires are anodes and the copper clad panels are the cathodes. The copper is subdivided into electrically distinct pads on one side of the panel, and copper traces on the opposite side of the panel carry the cathode signal to the edge of the quadrant. Longitudinally summing the pad signals gives a single tower signal. The pad signals are ganged in three distinct depth segments, five layers, twenty-four

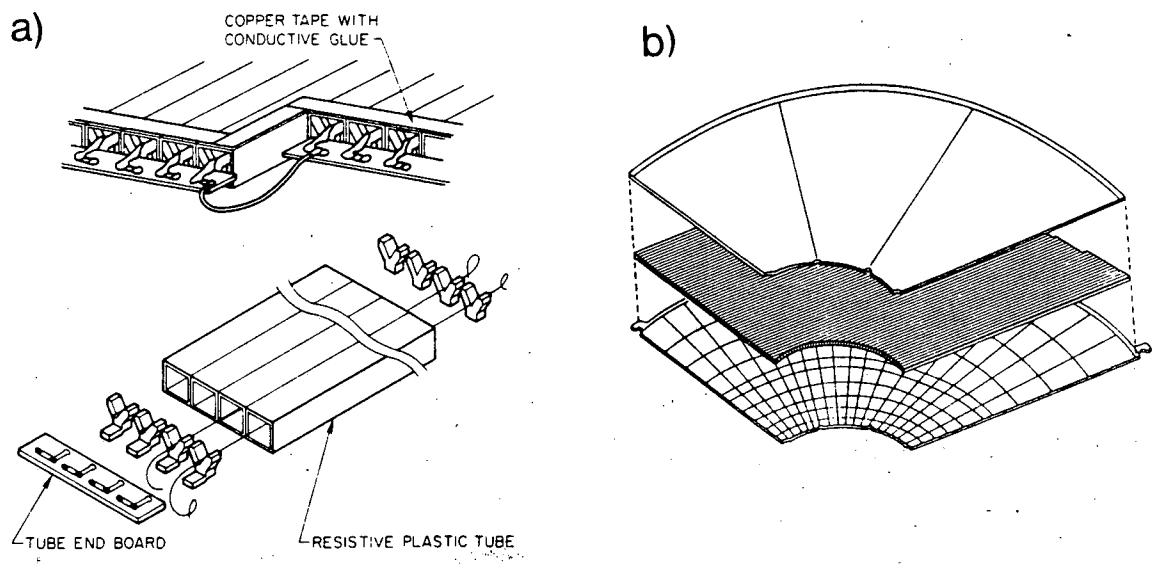

Figure 3.7: **a)** PEM proportional tubes and anode supports. **b)** PEM quadrant proportional layer construction.

layers, and five layers deep. The energies in the three segments are summed offline to give the total electromagnetic energy in a tower. The completed quadrant is a stack of thirty-four proportional layers, each 12 mm thick, interleaved with thirty-three lead layers, each 2.69 mm thick, and covered in front and rear with steel cover plates, 12.7 mm and 44.5 mm thick respectively. Excluding the rear coverplate, which acts as the first absorption layer of the endplug hadronic calorimeter, the total interaction thickness for electromagnetic and hadronic showers in the PEM is $18.2/\cos\theta$ radiation lengths and $1.0/\cos\theta$ interaction lengths respectively. Here $\cos\theta$ takes into account the changing interaction length with angle of incidence.

Initial Calibration

All towers of all quadrants of the PEM were calibrated with 100 GeV electron beams at the Mbottom test beam at Fermilab in 1985. The PEM response was measured with electrons from 20 to 200 GeV. The tower response is relatively flat in η and ϕ, with a tower to tower R.M.S. deviation of 6%. This variation has no significant effect on jet η and ϕ centroids, found by averaging over the many towers

in a jet. The calibrations were done at 1.8 KV and scaled to the operating voltage of 1.7 KV. The response of the PEM was found to be linear to 3%. The resolution for electrons between 20 and 200 GeV is $\sigma/E \approx .3/\sqrt{E}$. Response and resolution measurements were repeated in 1988. Analysis [37] of simultaneous measurements of the response of the PEM and Endplug Hadron Calorimeter to charged pions, reveal that the PEM response to charged pions between 100 and 160 GeV is 80% of its response to electrons of the same energy.

3.3.2 Endplug Hadron Calorimeter (PHA)

Tower Geometry

The PHA[37,38] is azimuthally arranged in 30° sectors, twelve sectors at positive z and twelve at negative z. The towers in the PHA cover 5° in ϕ and 0.09 units of η. Twelve towers of the PHA at positive z cover the angular range $30° < \theta < 10°$ ($1.1 > \eta > 2.4$). These towers, numbered 12 to 23, are shown in figure (3.2).

Construction and Signal Collection

The PHA is a sandwich of steel and gas filled proportional tube layers. Each gas proportional tube consists of a 50 micron diameter gold plated tungsten wire centered in a resistive plastic tube of rectangular cross section. The tube, pictured in figure 3.8a, has walls of the same thickness as PEM tubes. The tubes are laid side by side, sandwiched by a copper ground plane and copper cathode plane, and cut to form pie shaped chambers. The chamber construction is pictured in figure 3.8b. An HV bus runs along the side of the chamber supplying high voltage to each proportional tube. The cathode plane consists of electrically distinct pads on the inner side, electrically connected to the outer side via a plated through hole. Copper traces on the outer side of the plane carry the cathode signal to the edge of the chamber. Each chamber consists of seventy-two pads, twelve rows by six columns. There are six sets of connector pins at the edge of the chamber; each

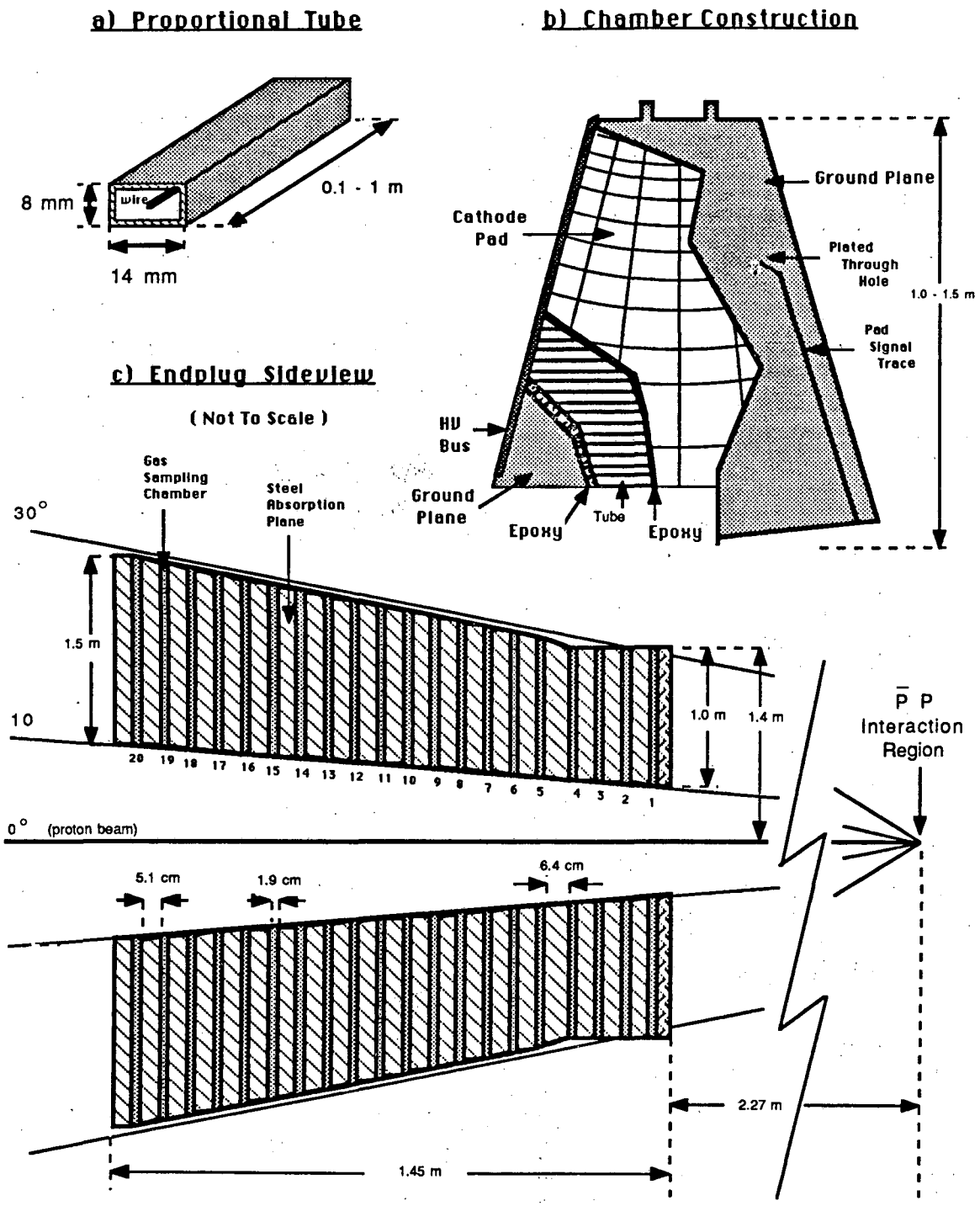

Figure 3.8: The Endplug Hadronic Calorimeter (PHA) **a)** Conductive plastic proportional tube. **b)** Chamber construction. **c)** Endplug sideview.

connector connects the signal and ground for twelve pads (three columns by four rows) to ribbon cables which transmit the cathode signals to front end amplifiers in the collision hall. Twenty proportional chambers are sandwiched by twenty-one steel plates to form a single sector of the hadron calorimeter. A side view of one of the two PHA endplugs is shown in figure 3.8c. The plates are 5.1 cm thick, except for the plate between the fourth and fifth layers which is 6.4 cm thick, and the front plate which is 4.45 cm thick and serves as the rear cover plate of the PEM. Including approximately 0.15 interaction lengths of copper plated G10, the total thickness for hadronic showers in the PHA is $6.3/\cos\theta$ interaction lengths.

The signals from the ribbon cables from each chamber in the sector are ganged together longitudinally to form towers, twelve towers per ribbon cable, seventy-two towers per sector. The cathode tower signals are then amplified and digitized. In addition, the common anode signal of all the tubes in a single chamber is picked off the HV supply line. The anode signal for each chamber is separately amplified and digitized, providing information on longitudinal shower development, which was invaluable in diagnosing calorimeter problems. For example, it was discovered that there were occasionally large pulses of energy in a single tower associated with a single layer. These "Texas Towers" [39] were first observed in the Forward Hadronic Calorimeter. The "Texas Towers" are local energy depositions presumed to be from highly ionizing protons with a few MeV of energy. The protons are produced when a neutron scatters from hydrogenous material in the chamber walls or in the gas. Longitudinal information from the anode signals helped us distinguish real energy from "Texas Towers". In another example, during the 1987 run intermittent noise was induced in the cathode cables by nearby 400 Hz power supplies, but not in the anode signals. The simple grouping of twelve pads per cable allowed easy pattern identification of potential cathode "cable noise". Longitudinal information from the anode signal, and electromagnetic energy in the PEM, helped distinguish real energy from "cable noise". Thus, the cathode signals were used to form towers of calorimeter energy, and the anodes signals served as important diagnostic checks on the calorimeter energy.

Initial Source Calibration

Each of the seventy-two pads of 520 chambers—480 used in the endplugs and forty spares—were calibrated with Cd^{109} sources at Lawrence Berkeley Laboratory between 1984 and 1985. The proportional tubes under each pad were exposed to an 8 KeV copper fluorescence x-ray, induced by the 22 KeV x-ray from the source, and the signals on both the cathode pad and anode wire were recorded. During the calibration of each chamber, anode signals were also recorded from a standard chamber. For each pad the ratio of the pad signal to wire signal, for that pad and for the four adjacent pads, was calculated and saved. The pad to wire ratio was normalized to the wire response of the standard chamber, removing potential variations from chamber to chamber caused by wire response. The normalized pad to wire ratio is a measure of the response of each cathode pad. These pad response measurements improve the energy resolution for pions[40]. We used these measurements to assign chambers to each of the twenty-four sectors in a way which minimized longitudinal variations in response. The tower response was then calculated by averaging the pad to wire ratio over the twenty cathode pads in a tower. Since a simple average and a weighted average showed no significant difference, the simple average was saved as a measurement of the tower response. They were used by the author to calculate the PHA sector response map presented in appendix C.2. The sector response maps agree with jet data and "Texas Tower" signals[41].

Initial Test Beam Calibration

Five sectors of the PHA were calibrated with 200 GeV charged pions in 1985. The response and resolution of two sectors of the PHA were measured with charged pions between 20 and 200 GeV. The response was linear and the resolution for charged pions was $\sigma/E \approx 1.28/\sqrt{E} + .03$. In 1988 a sector was exposed to charged pions between 20 and 230 GeV, and the response was again observed to be linear. During the 1988 test beam, fluctuations in response caused by "texas towers" were removed and the resolution improved to $\sigma/E \approx .86/\sqrt{E} + .04$.

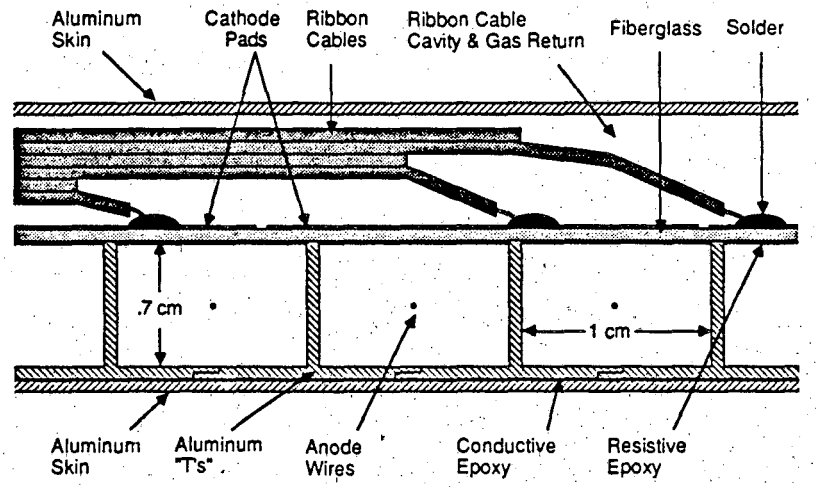

Figure 3.9: Cross section of an FEM chamber.

3.3.3 Forward Electromagnetic Calorimeter (FEM)

Tower Geometry

The FEM[42] is azimuthally arranged in 90° quadrants, four quadrants at positive z and four quadrants at negative z. The projective towers in the FEM span 5° in ϕ and there are twenty divisions in η. The first division is a fraction of a normal tower subtending about 0.03 units of η. The next nineteen divisions are normal sized towers, each 0.1 units of η. The nineteen normal sized towers of the FEM at positive z cover the angular range $11° > \theta > 2°$ ($2.3 < \eta < 4.2$). These towers, numbered 23 to 41, are shown in figure 3.2.

Construction and Signal Collection

The FEM is a sandwich of lead and gas filled proportional tube layers, with a total of $25.5/\cos\theta$ radiation lengths. The proportional chamber construction is shown in figure 3.9. Channels were formed by aluminum "T's" glued to an aluminum skin. Then fiberglass was glued to the aluminum channels to form a series of rectangular proportional tubes. A resistive epoxy coat on the inner side of

the fiberglass provides a path to ground for positive ions liberated in the electron avalanche. A 50 micron gold plated tungsten wire in the center of each tube is the anode, and copper pads on the outer side of the fiber glass are the divided cathode. Ribbon cables are soldered to the cathode pads and a final aluminum skin seals the chamber. There are thirty proportional layers in a quadrant, and the pad signals are ganged in two longitudinal depth segments, each fifteen layers deep. The energy for each depth segment is saved, and combined offline to form a single tower of electromagnetic energy. The anode wires are strung vertically and are ganged together in five sectors per chamber. These sectors, read out independently for each layer, provided information on longitudinal shower development.

Initial Calibration

Four quadrants of the FEM were calibrated with 20 to 200 GeV electron beams in 1985. The energy response of the FEM was linear between 20 and 160 GeV and the electron energy resolution was $\sigma/E \approx 0.25/\sqrt{E} + 0.05$. The response as a function of η was uniform within the statistics of the measurement. Response and resolution measurements were repeated in 1988.

3.3.4 Forward Hadron Calorimeter (FHA)

Tower Geometry

The FHA [43] is azimuthally arranged in 90° quadrants, four quadrants at positive z and four quadrants at negative z. The nineteen projective towers in the FHA are 5° in ϕ and 0.1 units of η and cover the angular range $11° > \theta > 2°$ ($2.3 < \eta < 4.2$). These towers, numbered 23 to 41, are shown in figure 3.2.

Construction and Signal Collection

The FHA is a sandwich of steel and gas proportional layers. There are twenty-seven steel plates, each 5 cm thick, and twenty-seven gas proportional layers. During the 1987 run only thirteen of the proportional layers were installed in each

quadrant. The total thickness for hadronic showers is about $8/\cos\theta$ interaction lengths. The chamber construction is similar to the FEM in figure 3.9, but the tube dimensions are 50% larger. The pads are ganged longitudinally in projective towers with no depth segmentation. The 50 micron anode wires are ganged together in six sectors per chamber, and these sectors, read out independently for each layer, provided information on longitudinal shower development.

Initial Calibration

One quadrant of the FHA was calibrated with charged pion beams in 1985. The energy response of the FHA was linear between 40 and 200 GeV and the pion energy resolution was $\sigma/E \approx 1.4/\sqrt{E}$ when all twenty-seven proportional layers were present; $\sigma/E \approx 2.0/\sqrt{E}$ during the 1987 run. Response and resolution measurements were repeated in 1988.

3.4 Tracking Chambers

The Vertex Time Projection Chamber (VTPC[44]) consists of eight separate time projection chamber modules, stacked end to end in z. Four of the modules are shown surrounding the beam pipe in figure 3.1b. Each chamber is divided azimuthally into eight octants. Each octant measures the radial and z coordinate of charged particle tracks. Tracks in the VTPC were projected back to the event vertex to determine its z position, called the *z vertex*. The z-vertex resolution was about 3 mm. During the 1987 run the z-vertex was Gaussian distributed about $z = 5$ cm with a RMS deviation of 35 cm. The z-vertex was used to calculate, on an event by event basis, the direction of the energy deposited in calorimeter towers.

The Central Tracking Chamber (CTC[45]) is a cylindrical drift chamber surrounding the VTPC, as shown in figure 3.1b. Surrounding the CTC is a superconducting coil which provides a 1.5 Tesla axial magnetic field. The momentum of charged particles was measured in the angular region $40° < \theta < 140°$ ($|\eta| < 1$) with transverse momentum resolution $\delta p_t/p_t^2 \leq .002$ GeV^{-1}. Central calorimeter en-

ergy response non-linearities for low energy particles were determined by comparing measurements of charged particle momentum from the CTC to the corresponding energy deposited in the calorimeter[46]. Charged particle track measurements were also used in studying jet fragmentation, necessary for tuning the Monte-Carlo jet simulation used for calculating jet energy corrections[47].

3.5 Beam-Beam Counters

The Beam-Beam Counters (BBC[48,49]) are scintillator hodoscopes close to the beam pipe used to reject unwanted triggers and estimate the luminosity. Unwanted triggers were collisions between the beam and residual gas in the beam pipe (beam-gas), energy deposition from a halo of particles in time with the beam (beam halo), or particles originating outside the CDF detector (cosmic rays). The BBC provided a count of true beam-beam collisions by comparing the time energy was deposited close to the beam with the expected beam crossing time.

The BBC consist of two sets of sixteen scintillator counters, one set on each side of the interaction point at $|z| = 582$ cm. The sixteen scintillator counters, four per quadrant arranged in a criss-cross grid, form four concentric squares in the xy plane. The position of one set of BBC is shown in figure 3.1b. It covers an angular range $4.5° > \theta > 0.32°$ ($3.2 < \eta < 5.9$). A coincidence between the counters on one side (east side) of the interaction point and the counters on the other side (west side), within a fifteen nanosecond gate centered twenty nanoseconds after the beam crossing, was a single BBC E·W *coincidence*. The time resolution of the counters was 0.2 nanoseconds.

The integrated luminosity is the number of BBC E·W coincidences divided by the fraction of the $\bar{p}p$ total cross section accepted by the BBC. The acceptance of the BBC for the diffractive and hard inelastic components of the total cross section was determined using a monte carlo simulation. The diffractive and hard inelastic $\bar{p}p$ cross section was estimated from an extrapolation[50] of $\bar{p}p$ results at lower $\sqrt{s}$ [51,52]. The total cross section accepted by the BBC was estimated[49] to be 44

millibarns; a systematic uncertainty of 15% came primarily from uncertainties in the extrapolation. The run to run systematic variation of the luminosity measurement was estimated[49] to be 11%. The uncertainty in the luminosity resulting from this run to run uncertainty, was $11\%/\sqrt{N}$ where N is the number of runs in the sample. This uncertainty is independent of the BBC cross section uncertainty, and the two uncertainties are added in quadrature to estimate the total uncertainty on any sample.

3.6 Trigger

The CDF level 1 trigger[48] was used to select "minimum bias" $\bar{p}p$ interactions, jets, electrons, and muons. The "minimum bias" trigger required only a BBC E·W coincidence. Of the other triggers, only the jet trigger will be described here. Simply put, the jet trigger is a global transverse energy trigger, which requires the total transverse energy summed over all, or some, of the calorimeters to be greater than a threshold value.

Transverse energy sums were calculated from signals in *trigger towers*. A trigger tower subtends $\Delta\eta \times \Delta\phi = 0.2 \times 15°$; two standard towers in the central calorimeters, or six standard towers in the gas calorimeters. Separate electromagnetic and hadronic trigger towers were each required to have greater than 1 GeV transverse energy to be included in the sum. The transverse energy was defined using the nominal event vertex at the center of the detector. A *global sum* E_t was calculated as the sum of all the electromagnetic towers (CEM, PEM, and FEM) and all the central hadronic towers (CHA and WHA). A *gas sum* E_t was calculated as the sum of all the electromagnetic gas calorimeter towers (PEM and FEM). Signals from the hadronic gas calorimeters (PHA and FHA) were not included in the trigger because of noise problems: texas towers and cable noise described in section 3.3.2 and section 4.2.

The jet trigger required that there be a BBC E·W coincidence and the following calorimeter trigger:

global sum E_t greater than the *global sum E_t threshold*

or

gas sum E_t greater than the *gas sum E_t threshold.*

The thresholds were set depending on the run's luminosity to keep the total event rate approximately 1 Hz. The thresholds were given the names *low*, *medium*, *high* and *burn* corresponding to global sum E_t thresholds of 20, 30, 40 and 45 GeV respectively and gas sum E_t thresholds of 10, 15, 20, and 20 GeV respectively.

The *hardware trigger* described above was used to determine which events were saved and written to tape. Only events triggered by energy in the central calorimeters were used in the final analysis. The primary reason for this, was that the hadronic gas calorimeters were not in the trigger, so events which were triggered by the gas sum E_t trigger had a complicated bias towards EM energy. In addition, the calibration of the central calorimeters (CEM, CHA, and WHA) was better known. Finally, noise problems in the PEM contributed a substantial fraction of the gas sum E_t trigger rate. For these reasons, we used offline software to remove all the gas calorimeters from the global sum E_t trigger decision. This was accomplished with a *software trigger* (TRGSIM) which calculated the global sum E_t using only transverse energy from the CEM, CHA and WHA and required it to be greater than the appropriate global sum E_t threshold. The software trigger passed a sample of events appropriate for our two jet analysis, in which one jet centroid was well contained in the central calorimeters. The software trigger used the same lists of trigger towers, and the same trigger tower E_t thresholds, as were used during the 1987 run. In section 4.6.2 we discuss the central jet E_t thresholds necessary to make the software trigger 98% efficient.

3.7 Data Acquisition Electronics

The signals from the gas calorimeter cathode pad towers and the central calorimeter photomultiplier tubes were amplified with charge integrating amplifiers. This *front end* electronics[53] was of a *sample and hold* design, which sampled the

signal and then held it awaiting digitization. The signal was integrated and stored both *before* and *after* the beam crossing. The difference of the two signals was digitized by the EWE, an ADC, which also subtracted the pedestal from the analog signal and compared the result to a threshold before digitization. The digitized signals were read out by custom microprocessors (MX), which also multiplied the digitized signals by channel dependent calibration constants. The calibration constants corrected for variations in electronic gain from channel to channel, and for gas gain variations in the gas calorimeters (see appendix B). The MX only read out the digitized signals if the CDF level 1 trigger had been satisfied. The level 1 trigger decision was made quickly by summing the analog trigger tower signals transported individually to the counting room. FASTBUS modules[54] controlled the communication of the trigger decision to the MX and, if the MX was instructed to read out the digitized data, other FASTBUS modules read out the MX. The digitized data, transferred from FASTBUS to a VAX computer cluster, was then monitored online and written to tape.

Chapter 4

Data

4.1 Data Sample

The 1987 calorimeter data sample was accumulated with the four hardware global E_t trigger thresholds discussed in section 3.6. A summary of the data sample is provided in table 4.1. The raw integrated luminosity was estimated using the beam-beam counters as discussed in section 3.5. All events were required to have an event vertex well contained within the center of the detector ($|z| < 60$ cm). The effect of this *z-vertex cut* on the integrated luminosity was measured in the minimum bias data sample[55]. All luminosities were uncertain by 15% except for the low threshold data sample. The low threshold sample consisted of only two major runs, and consequentially had a run to run variation uncertainty of 8% ($11\%/\sqrt{2}$). Adding the normalization systematic uncertainty of 15% in quadrature with the run to run variation uncertainty of 8% gives 17% for the total systematic uncertainty on the luminosity for the low threshold sample.

4.2 Energy Reconstruction

The data sample described in the previous section was passed through a series of software filters designed to remove noise. The sources of noise were:

Quantity	*Trigger Threshold*			
	Low (20 GeV)	Medium (30 GeV)	High (40 GeV)	Burn (45 GeV)
Raw Cal. Triggers (Events)	15852	85816	15895	14552
Raw Luminosity (nb^{-1})	0.404	11.9	5.93	6.25
$\|Z\| < 60$ cm. Lum. (nb^{-1})	0.351	10.5	5.42	5.77
Systematic Error on Lum.	17%	15%	15%	15%
Corrected Jet E_t^{thresh} (GeV)	45	55	65	75
Efficiency	>99%	>98%	>98%	>98%

Table 4.1: Number of events, luminosities, corrected central jet E_t thresholds and corresponding efficiencies for each of the hardware trigger thresholds present in the 1987 run.

- **First Event after a Pause:**

  The first event after a 20 second pause generally contained unphysically large amounts of energy from pedestal shifts. These events, less than 0.5% of the data sample, were removed by the filter "SHOOTFIRST".

- **Pedestal Shifts:**

  Pedestal shifts not removed by the EWE automatic pedestal subtraction were discovered during channel occupancy studies of minimum bias data. They were observed in $\sim$ 10% of the channels and were corrected by the filter "CALORIMETRY"[34], which subtracted the mean pedestal shift measured in minimum bias data[56].

- **"Hot" Electronic Channels:**

  In the same minimum bias analysis mentioned above, some electronic channels were discovered to have very large pedestal shifts or widths and other channels were dead. These channels, amounting to less than 0.5% of all calorimeter channels and less than 0.1% of central calorimeter channels, were excluded from our analysis by "CALORIMETRY".

- **"Hot" PMT's:**

  In the central calorimeters a few photomultiplier tubes occasionally gave unphysically large signals due to high voltage discharge. Also, as described in section 3.2.4, electromagnetic showers in the light guides produced large signals. These PMT *spikes* usually were present in one of the two PMT's per calorimeter tower. The ratio of the signal in the two PMT's was used to identify PMT spikes[34], which were then removed from the data by "CALORIMETRY".

- **Cosmic Rays and Main Ring "Splash":**

  Cosmic Rays and accelerator losses (splash) from the tevatron booster ring (main ring) which passed above CDF, occasionally deposited large amounts of energy in the calorimeter. This energy usually arrived *out of time* with the proton-antiproton beam crossing. Timing signals from TDC's on the central and endwall hadron calorimeters were used to identify and eliminate out of time energy. The filter "HATFLT"[57,58] was 95% efficient at removing events triggered by cosmic ray events and more than 98% efficient at removing main ring "splash" events but removed less than 0.1% of real events.

- **PHA Cable Noise:**

  As discussed in section 3.3.2, ground loops in the cathode pad signal cables allowed nearby power supplies to induce noise in the PHA cathodes but not in the anodes. This *cable noise* appeared in the data with the same topology as the 12 channel ribbon cable, forming a 3 tower by 4 tower rectangle of energy deposition. Real particle showers usually deposited energy in the PEM as well as the PHA, and always produced signals in the anodes. The filter "NCABLE"[59] identified cable noise by its particular cable topology, lack of electromagnetic energy, and absence of anode energy. "NCABLE" removed cable noise with greater than 98% efficiency if the noise had more than 5 GeV of energy, and is estimated to remove real hadronic energy in less than 0.1% of the events.

- **Texas Towers and PEM spikes:**
  As discussed in section 3.3.2, texas towers are large spikes of *apparent* energy in the gas calorimeters, localized to practically a single anode layer and a few cathode towers. These spikes were presumed to be produced when neutrons elastically scattered protons which deposited most of their true energy in a single gas proportional layer. All of the true proton energy, a few MeV, was collected and then scaled by the calorimeter calibration constants into tens of GeV of apparent energy. The calorimeter calibration constant was a large multiplier because most particles produced showers which deposited less than 0.1% of their energy in the gas and more than 99.9% of their energy in the lead or steel absorber. The calorimeters, calibrated in test beams to scale small energy depositions in the gas into large shower energies, scaled the small proton energy deposition into large energy *gas spikes* called texas towers. Texas towers were observed in all the gas calorimeters, though they were a more serious problem in the hadronic gas calorimeters where the relative sampling fraction was smaller and hence the energies were scaled higher. Another kind of gas spike was observed in the PEM. These PEM *spikes* were caused by high voltage breakdown near the anode supports at $|\eta| \approx 1.1$. Both kinds of gas spike were characterized by apparent energy depositions localized both longitudinally and transversely. The filter "FILT_GAS"[56,60] identified transversely localized *clumps* of energy. It used the tower depth segmentation and anode longitudinal information to determine which of the clumps were gas spikes and removed them from the event. "FILT_GAS" was greater than 95% efficient at removing isolated gas spikes with more than 20 GeV of apparent energy[56].

The first phase of data reconstruction started with the sample defined in the previous section and selected events which triggered the central calorimeters. The data was reformatted from detector oriented arrays into a tower indexed array by "CALORIMETRY", and all the filtering functions of "CALORIMETRY" mentioned above were used. During this first pass we only reconstructed central

calorimeter tower energies (CEM, CHA, and WHA), and all the gas calorimeter tower energies were set to zero. Next, to eliminate cosmic ray events, the data was passed through "HATFLT". Then the software trigger (TRGSIM), discussed in section 3.6, selected events which were triggered by central calorimeter energy alone. The configuration of the hardware trigger as a function of time had been saved in a data base, and was reproduced by TRGSIM. The original data arrays for this *central triggered* data sample were written to tape.

In the second phase of data reconstruction the central triggered data sample was fully reconstructed and filtered. The data was again reformatted from the original detector oriented arrays into a tower indexed array by "CALORIMETRY"; this included both central and gas calorimeter energies. Pedestal shifts were corrected, "hot" electronic channels were excluded from the analysis, "hot" PMT's were zeroed, and cable noise and gas spikes were removed. "CALORIMETRY" used a map of the PHA sector response to improve PHA sector calibrations (see appendix C.2). The energy measured by the gas calorimeter towers was corrected for the presence of dead anodes by the software module "DEDWIR" (see appendix C.1). The filtered and calibrated tower energies were stored in a tower indexed array prior to jet reconstruction.

4.3 Jet Definition

Partons emerge from the $\bar{p}p$ collision and hadronize into jets of particles before they even reach the detector. We expect the particle transverse momentum with respect to the parton direction, $\vec{p}_t$, to be distributed in an azimuthally symmetric fashion about the parton direction. As mentioned in section 2.1.3, the locus of $\eta\phi$ points of particles having constant transverse momentum with respect to some jet axis and constant transverse energy with respect to the z-axis is approximately a *circle* in $\eta\phi$ space. Thus, the set of trajectories of particles with E_t above a threshold value are expected to be within a *cone* whose axis emerges from the interaction and intersects the detector $\eta\phi$ grid in a circle. For observed jets,

the set of towers with energy above an E_t threshold is approximately circular in $\eta\phi$ space. This suggests a natural way to define a jet.

4.3.1 Jet Clustering Algorithm

A jet *clustering algorithm* is a set of rules for associating towers of calorimeter energy with a single jet. The clustering algorithm we use (JETCLU[56,61]) defines a cluster by the energy contained within a circle in $\eta\phi$ space. The circle has fixed radius

$$R = \sqrt{(\Delta\eta)^2 + (\Delta\phi)^2} \tag{4.1}$$

where ϕ is measured in radians. This radius is also called the *cone size.* A large cone size (R=1.0) was chosen because jet energy resolution improves with increasing cone size. The JETCLU clustering algorithm, schematically pictured in figure 4.1, forms clusters from towers of calorimeter energy. High transverse energy clusters are jets.

The basic unit of the JETCLU clustering algorithm is a tower. The electromagnetic transverse energy in a tower was defined as the electromagnetic calorimeter tower energy times $\sin\theta_{EM}$, where θ_{EM} was the angle defined by the z-axis, the event z-vertex, and a point at the η center of the tower ten radiation lengths from the event vertex. The hadronic transverse energy in a tower was defined similarly, using a point in the η center of the hadronic calorimeter tower three absorption lengths from the event vertex. The transverse energy in a tower was defined as the sum of the electromagnetic transverse energy and the hadronic transverse energy. Towers in the gas calorimeters were combined to be the same size as towers in the central calorimeter ($\Delta\eta \times \Delta\phi = .1 \times 15°$).

The JETCLU clustering started by finding all *seed towers* with greater than 1 GeV of transverse energy. Seed towers were combined with adjacent seed towers, either on a side or at a corner, to form *preclusters.* Adjacent seed towers in a precluster were required to have monotonically decreasing transverse energy; in a precluster there could be no energy "valleys" only energy "peaks". Preclusters

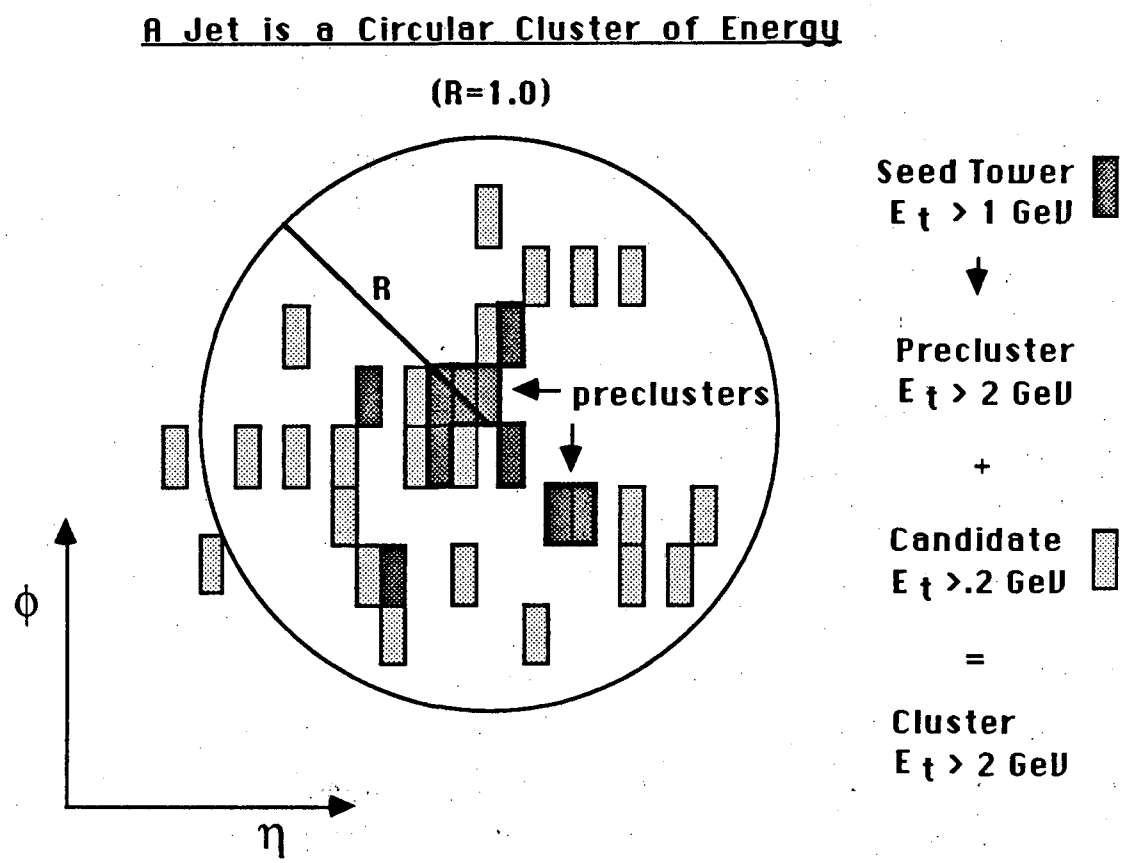

Figure 4.1: The JETCLU clustering algorithm. The cluster is all the energy contained within a circle in $\eta\phi$ space. The algorithm starts with seed towers, forms preclusters from adjacent seeds, and includes all candidate towers within a circle centered on the preclusters in the cluster. The center is then recalculated, and clusters are merged, in an iterative procedure. High transverse energy clusters are jets.

were required to have at least 2 GeV of transverse energy. A circle of radius 1.0 in $\eta\phi$ space was centered on the E_t weighted $\eta\phi$ centroid of the precluster. This was done for each precluster in the event. All towers inside the circle, with E_t above a *candidate* threshold of 0.2 GeV, were included in the *cluster*. The cluster $\eta\phi$ centroid was calculated and a circle was centered on the centroid. Only candidate towers inside the new circle were included in the new cluster, and a new $\eta\phi$ centroid was calculated, and this process was iterated until the list of towers inside the cluster no longer changed. To prevent cluster centroids from wandering too far in exotic cases, the original precluster towers were kept inside the cluster regardless of whether they lay inside the circle.

Each cluster was formed without regard to the possible presence of other clusters. Cluster *overlap* occurred when a tower was included in more than one cluster. These *disputed* towers were not permitted to be shared. If the total amount of E_t in disputed towers was greater than half the E_t of either cluster, then the two clusters were merged into a single cluster. If the E_t in disputed towers was less than half the E_t of either cluster, then the two clusters were separated, and each disputed tower initially went to the closer cluster. The separated cluster centroids were recomputed, and again the disputed towers were assigned to the closer cluster, and this process was iterated until the list of towers assigned to a cluster no longer changed.

4.3.2 Cluster E_t and η

The cluster energy, $E_{cluster}$, was a sum of the energy in all the towers in the cluster. Let i be the index of a tower in the cluster, let $E_{EM,i}$ be the energy in the electromagnetic compartment of that tower, and let $E_{HAD,i}$ be the energy in the hadronic compartment of that tower. Then the cluster energy is defined as the scalar sum

$$E_{cluster} = \sum_i (E_{EM,i} + E_{HAD,i}) \tag{4.2}$$

The pseudorapidity and transverse energy of the cluster was defined using

the direction of the cluster axis determined from the cluster energy-momentum four-vectors. We assume energy was deposited in each tower by extremely relativistic particles, so the momentum of the cluster was calculated as the vector sum of the tower energies. The electromagnetic and hadronic energy vectors were calculated separately by JETCLU, because the event z-vertex was not at the exact center of the detector. Let i be the index of a tower in the cluster, let $\theta_{EM,i}$ and $\theta_{HAD,i}$ be the polar angles of the electromagnetic and hadronic compartments of the tower respectively (see section 4.3), and define ϕ_i as the common azimuthal angle of both the electromagnetic and hadronic compartments. Then the components of the cluster momentum are

$$P_x = \sum_i (E_{EM,i} \sin\theta_{EM,i} + E_{HAD,i} \sin\theta_{HAD,i}) \cos\phi_i \tag{4.3}$$

$$P_y = \sum_i (E_{EM,i} \sin\theta_{EM,i} + E_{HAD,i} \sin\theta_{HAD,i}) \sin\phi_i \tag{4.4}$$

$$P_z = \sum_i (E_{EM,i} \cos\theta_{EM,i} + E_{HAD,i} \cos\theta_{HAD,i}) \tag{4.5}$$

$$P = \sqrt{P_x^2 + P_y^2 + P_z^2} \tag{4.6}$$

The polar angle of the cluster, θ, is defined by the equation

$$P_z = P\cos\theta \tag{4.7}$$

and the pseudorapidity of the cluster, η, is defined by

$$\eta \equiv -\ln\tan\frac{\theta}{2} = \frac{1}{2}\ln\left(\frac{P+P_Z}{P-P_Z}\right) \tag{4.8}$$

The total transverse energy of the cluster, $E_{t,cluster}$, is simply defined as

$$E_{t,cluster} \equiv E_{cluster}\sin\theta = \frac{E_{cluster}}{\cosh\eta}. \tag{4.9}$$

The pseudorapidity, η, measures the direction of jets with respect to the event z-vertex, while the detector pseudorapidity of the cluster, η_d, measures the direction of jets within the detector. Here η_d is defined as the E_t weighted η centroid of the cluster where no correction is made for the event z-vertex when the tower E_t and tower η is calculated. Note that η and η_d are equal when the event vertex is at $z = 0$, but $\eta_d - \eta \approx \pm 0.2$ when the event vertex is at $z = \pm 60$ cm.

4.3.3 Leading Jets

Define the two *leading jets* as the two clusters with the highest transverse energy in the event. The two leading jets approximate the two final state partons. Gluon *bremsstrahlung* from initial and final state partons, discussed in section 2.1.6, has less transverse energy than the primary scattered partons, and produces a falling spectrum of lower E_t clusters (see section 4.8.4). Also, a background of roughly constant transverse energy density was present in the detector. This *underlying event*, presumed to originate from very soft interactions of spectator partons, sometimes fluctuated up and appeared as low transverse energy clusters. To avoid confusing gluon bremsstrahlung and fluctuations in the underlying event for the final state partons we seek to study, we associated the two leading jets with the two final state partons.

4.4 Central Jet Energy Corrections

The cluster energy, $E_{cluster}$, is less than the *true jet energy* E_{jet}. On average, a jet of particles with total energy $E_{jet} = 50$ GeV produced a cluster in the central calorimeters with $E_{cluster} = 40$ GeV. The total *jet energy loss*, measured for jets in the region $0.1 < |\eta_d| < 0.7$, was the result of a combination of effects:

- **Low Energy Non-Linearities**
  As described in section 3.2.1 and 3.2.2, the central calorimeters were calibrated in a test beam with high energy electron and pion beams. Linear energy-response relations were used to define electromagnetic and hadronic compartment energies during the 1987 run. However, the full response of the electromagnetic plus hadronic compartments to charged pions was slightly non-linear for charged pions around 10 GeV. Also, an analysis [46] which compared the momentum of charged particles in the central tracking chamber to the corresponding energy deposited in the calorimeter, determined that the calorimeters respond non-linearly to particles with momentum between

0.5 and 8 GeV. These measurements determined that the response of the central calorimeter to charged particles with energies below ~10 GeV deviated from a linear extrapolation by as much as ~40% [7]. A detector simulation was tuned to reproduce the measured non-linearities. An analysis using the simulation determined that a 50 GeV jet loses an average of 7.5 GeV from calorimeter non-linearities [62,47]. This was the largest contribution to the total jet energy loss.

- **ϕ Cracks and Other Calorimeter Losses**

  The central calorimeter has cracks at the azimuthal boundary between towers as described in section 3.2.4. The calorimeter response to electrons and pions aimed at the crack was measured in the test beam. A detector simulation was tuned to reproduce the measured response of both the ϕ crack and the the tower face[35]. Jet energy losses also occur when low momentum ($\leq$ .4 GeV) charged particles curl up in the central magnetic field, never reaching the calorimeter, and when muons and/or neutrinos are part of the jet. The simulation estimated that the energy loss of a 50 GeV jet from sources other than non-linearities was 5 GeV on average.

- **Clustering Effects**

  A roughly uniform background energy deposition from the underlying event deposited energy in the JETCLU cluster. This energy should not be associated with the final state partons. An analysis [63] of a sample of two jet events measured the energy in a region 90° in ϕ from the jet axis, and estimated that the energy density of the underlying event in $\eta\phi$ space is 0.99 ± 0.35 GeV/rad^2. The total underlying event inside a jet clustering circle of radius 1.0 was a *jet energy gain* of about 3.1 ± 1.1 GeV. This energy gain was partially offset by true jet energy lost outside the clustering circle, and energy cut out by the 0.2 GeV candidate tower threshold, described in section 4.3.1. This jet energy loss was estimated[64] by varying the circle radius, varying the threshold, and taking into account the changes expected from the underlying event. The

small mean jet energy loss ascribed to the cone size and candidate threshold, only 0.3 GeV, is within the total uncertainty on the underlying event. The total jet energy change from all clustering effects is a gain of 2.8 ± 1.4 GeV, and is roughly independent of jet energy[64].

The calorimeter non-linearities and ϕ crack response were incorporated into a full detector simulation as mentioned above. To estimate the central jet energy correction, jets were generated using the ISAJET[65] monte carlo. This used an *independent fragmentation* model for hadronizing final state partons into jets of particles and distributing the energy among them. A parton which fragmented into many low energy pions gave a smaller total energy in the calorimeter than one which fragmented into only a few high energy pions. This was simply caused by the low energy non-linearities. To insure that the independent fragmentation model was producing physically reasonable jets, the parameters of the model were tuned until jet fragmentation distributions from ISAJET matched CDF measurements in the central tracking chamber. The result of the tuning[47] was that the best parameters for the independent fragmentation model were those suggested by Field and Feynman[66], the originators of the independent fragmentation model. Two other reasonable parameter sets were studied[47]; they didn't fit the CDF data as well, and were used for upper and lower systematic bounds on the fragmentation parameters.

We used the tuned ISAJET monte carlo and the CDF detector simulation to generate two jet events. The energy deposited in the calorimeter, by particles associated with a jet, was compared to the total particle energy. This predicted the jet energy loss caused by non-linearities and cracks, which was combined with the jet energy gain from clustering effects, to determine the total jet energy correction. The correction was linear at high jet energies, and had a small quadratic piece at low jet energies. The central jet energy correction[47], the combined work of many

people in the CDF collaboration, is (for cone size $R = 1.0$):

$$\begin{aligned} &if \quad E_{cluster} < 70\ GeV \\ &\quad E_{jet} = (-0.174 \times 10^{-2})(E_{cluster})^2 + 1.37E_{cluster} - 2.36\ GeV \\ &if \quad E_{cluster} \geq 70\ GeV \\ &\quad E_{jet} = 1.115E_{cluster} + 6.68\ GeV \end{aligned} \tag{4.10}$$

The central jet energy correction is displayed along with its total systematic bounds in figure 4.2a. The ratio of the jet energy to the cluster energy is shown as a function of the jet energy. The correction varies from 1.25 for 50 GeV jets to 1.15 for 200 GeV jets. The total systematic uncertainty on the ratio, which is the total systematic uncertainty on the jet energy, is broken down into its components in figure 4.2b. Note that the calorimeter non-linearities, the largest contributor to the jet energy loss, is also the largest contributor to the uncertainty in the jet energy correction over most of the energy range. At high jet energies ($E_{jet} > 150$ GeV) the uncertainty in the calorimeter simulation, which contains within it the uncertainty in the test beam energy calibration, dominates the uncertainty in the jet energy correction. In figure 4.2b, the fragmentation uncertainty was estimated by varying the parameters of the independent fragmentation model, and the charged/neutral uncertainty was estimated by varying the ISAJET distribution of charged/total energy. The calorimeter calibration uncertainty is the estimated uncertainty on the maintenance of the central calorimeter calibration. These independent systematic uncertainties were added in quadrature to obtain the total systematic uncertainty.

The central jet energy corrections were the first and primary jet energy corrections applied in this analysis. From the corrected jet energy E_{jet} we obtain a first value for the corrected jet transverse energy E_t using

$$E_t \equiv E_{jet} \sin\theta = \frac{E_{jet}}{\cosh\eta} \tag{4.11}$$

where η was defined by equation (4.8). In section 4.7 we will present additional jet E_t corrections which are very small compared to the corrections in equation (4.10). First, it is necessary to discuss the initial event selection which proceeded using the corrections of equation (4.10) alone.

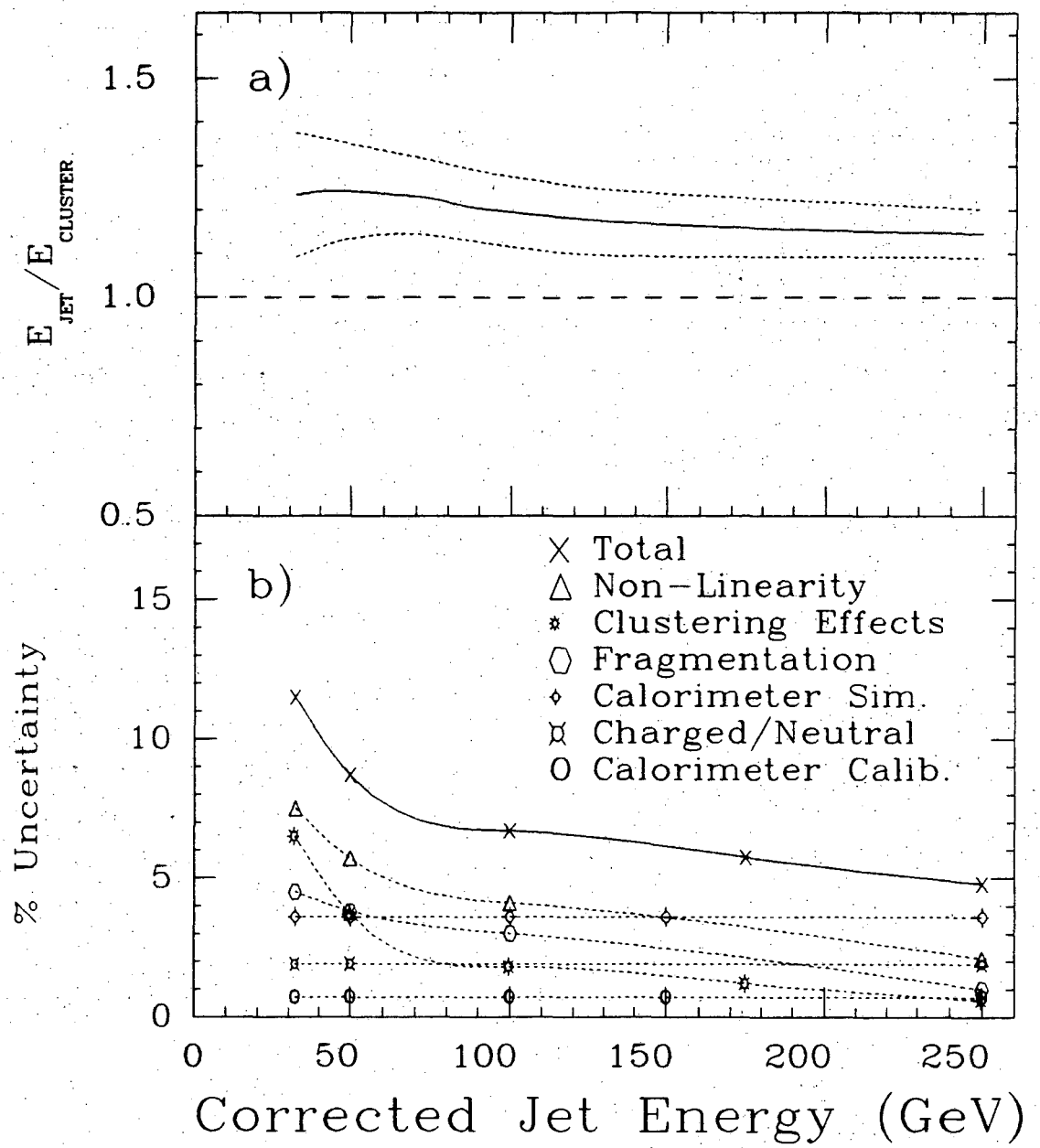

Figure 4.2: **a)** The central jet energy correction (solid) is bracketed by its total systematic bounds (dotted). **b)** Independent sources of systematic uncertainty on the jet energy, described in the text, are summed in quadrature to obtain the total systematic uncertainty (solid).

4.5 Event Selection

The initial event selection, designed to select events of the type $\bar{p}p \rightarrow$ jet1 + jet2 + X, is outlined in table 4.2. The calorimeter triggers from the 1987 run, described in section 4.1, were used. Cosmic ray and main ring events eliminated by HATFLT. were less than 1% of the sample. The software trigger, discussed in section 3.6, eliminated about a third of the sample. A z-vertex cut, discussed in section 4.1, rejected about 10% of the sample. The number of clusters in the event was required to be at least two. This cut rejected only a very small fraction of the sample, 0.4%, as expected for a good two jet sample. At least one of the two leading jets was required to be inside the region $|\eta| < 0.6$. This cut rejected 23% of the data sample. In order to insure that a single jet in the region $|\eta| < 0.6$ was solely responsible for triggering the event, a cut was placed on the corrected jet E_t. The jet E_t cut, E_t^{thresh}, depended on the hardware trigger threshold of the event, and was set by requiring a jet with $E_t = E_t^{thresh}$ to have sufficient E_t to satisfy the hardware and software trigger more than 98% of the time. The individual corrected jet E_t thresholds and corresponding efficiency are listed in table 4.1 and are discussed in the next section. The jet E_t cut rejected 91% of the remaining sample. The remaining 5096 events, chosen for the cross section measurement, were studied for systematic variations in central calorimeter response. The results of that study are discussed in section 4.7.

4.6 Jet Trigger

4.6.1 Trigger Jets and Probe Jets

At least one jet of the two leading jets, for which $E_t > E_t^{thresh}$ and $|\eta| < 0.6$, is called a *trigger jet*. The other, is called a *probe jet*, and is allowed to have any transverse energy and any pseudorapidity . If both leading jets are trigger jets, then they are also both probe jets. The pseudorapidity of the trigger jet is called η_1

Select	Events Remaining
Raw Calorimetry Triggers	132,115
HATFLT	131,167
Central & Endwall Triggers	86,205
$\|Z\| < 60$ cm	77,243
Number of Clusters ≥ 2	76,954
Central Jet ($\|\eta_1\| < 0.6$)	59,361
Central Jet $E_t \geq E_t^{thresh}$	5,096

Table 4.2: Cuts applied to full data sample and corresponding total number of events remaining. Separate central jet E_t thresholds were used for each hardware trigger threshold.

and the pseudorapidity of the probe jet is called η_2. The transverse energy of the trigger jet is just called E_t.

4.6.2 Trigger Efficiency

The jet E_t cut, E_t^{thresh}, depended on the hardware trigger threshold of the event, and was set by requiring a trigger jet with $E_t = E_t^{thresh}$ to have sufficient E_t to satisfy the hardware and software trigger more than 98% of the time.

E_t^{thresh} was first estimated by examining jet E_t distributions. Events were selected which had only one cluster in the region $|\eta| < 0.6$, and no other clusters with $|\eta_d| < 2.0$. In other words, one cluster was isolated in the central region and the other clusters were in the plug and forward calorimeters far enough away from the central calorimeters so they wouldn't significantly contribute to the software trigger. With these *isolated* jets, the E_t distribution of the cluster in the central region was measured for each of the four hardware trigger thresholds. For the medium sample, which had the best statistics, the isolated jet E_t distribution is shown in figure 4.3a. Notice how the hardware and software trigger thresholds cause the distribution to *roll-off* forming a peak at low E_t. We chose an E_t threshold far enough away from the roll-off so that our event sample would have practically *full acceptance*. The

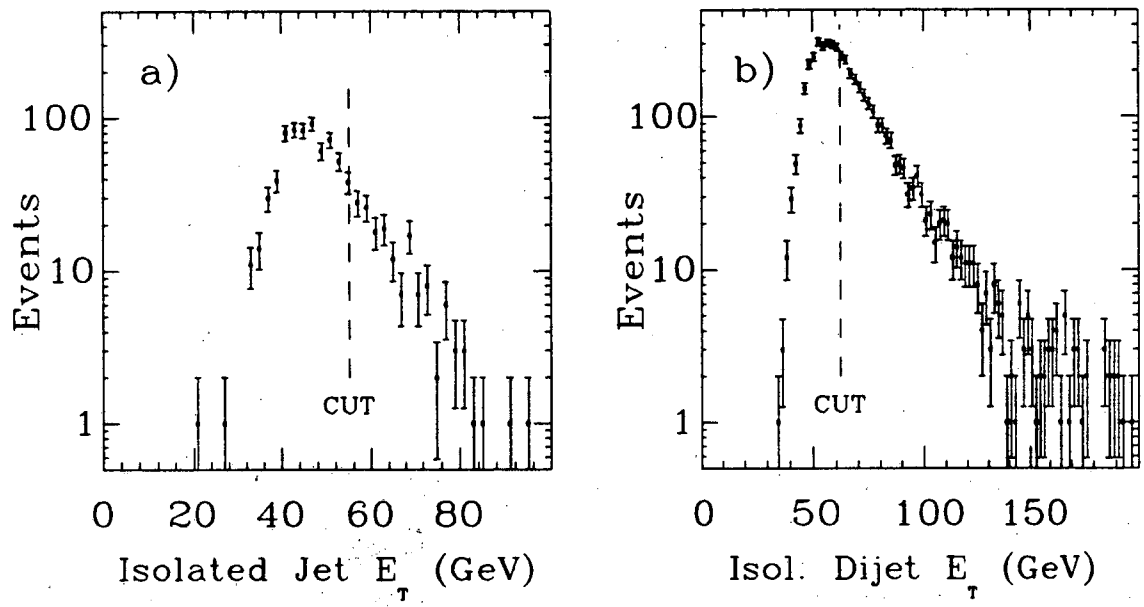

Figure 4.3: Trigger Jet E_t distributions for events from the medium threshold sample. **a)** The corrected jet E_t distribution for single jets in the region $|\eta| < 0.6$. This sample of events contains no other clusters with $|\eta_d| < 2.0$. The dashed line is $E_t{}^{thresh}$ for the medium sample. **b)** The distribution of "dijet" E_t $(E_{t1} + E_{t2})$, where both jets are in the region $|\eta| < 0.6$. This sample of events contains no other clusters anywhere in the calorimeters. The dashed line is the dijet E_t threshold for the resolution measurement sample.

E_t threshold chosen for the medium sample was 55 GeV; its position with respect to the trigger roll-off of the E_t distribution is shown in figure 4.3a as a dashed line labelled "CUT".

The measurement of E_t and η_2 resolution used a sample of events in which both leading jets were inside the region $|\eta| < 0.6$. For this sample, both leading jets were allowed to contribute to the trigger decision, and lower E_t jets were accepted. In figure 4.3b the distribution of "dijet" E_t, the scalar sum of the corrected jet E_t of the two jets, is shown for the medium sample. These events contain only two clusters, so no other clusters influenced the trigger. There are many more events in this plot than in figure 4.3a because this plot includes central-central two jet events, which are far more numerous than central-forward two jet events. Once again, we

cut far enough away from the peak to avoid losing too many events to the trigger roll-off. Events with dijet E_t greater than the threshold 62 GeV, from the medium trigger sample, are the sample of events used for resolution measurements, discussed in section 5.1. Dijet E_t thresholds of 80 GeV for the high trigger sample, and 90 GeV for the burn trigger sample, were chosen in a similar fashion; these samples were combined with the medium sample and used to measure the response of the 90° crack, as discussed in section 4.7.1.

The efficiencies of the trigger jet E_t thresholds were calculated by running the monte carlo ISAJET with a full detector simulation (QFL[67]) and the software trigger. The efficiency was calculated as the ratio of the number of jets accepted by the software trigger to the number of jets produced by ISAJET and QFL. When calculating the accepted number of jets, the software trigger used the same trigger towers and the same thresholds present in the 1987 run. When calculating the produced number of jets, only ISAJET and QFL were used. A separate study comparing the efficiency of the software trigger for calorimeter triggers in the data, to that simulated using ISAJET-QFL-TRGSIM, indicated that the trigger simulation was working properly in the region of interest.

The results of the efficiency analysis are shown in figure 4.4. Each chosen threshold was greater than 98% efficient at accepting single jet triggers. The dijet E_t cut on the medium sample, defining the sample of events used for our resolution analysis, was greater than 95% efficient at accepting dijet triggers.

The central jet threshold, E_t^{thresh}, is much greater than the corresponding global E_t threshold for a few reasons. First, the clustering accepts towers with as little as 0.2 GeV of total E_t while the hardware and software trigger only summed energy in trigger towers with greater than 1 GeV of Electromagnetic E_t or 1 GeV of Hadronic E_t. Second, a small fraction of the energy of a jet, with radius $R = 1.0$ and centroid in the pseudorapidity region $|\eta| < 0.6$, will sometimes fall outside of the central calorimeter: $|\eta_d| < 1.3$ in the hadronic section and $|\eta_d| < 1.0$ in the electromagnetic section. When this happens the energy will not be counted by the software trigger. Third, the jet E_t threshold is in corrected E_t which is approx-

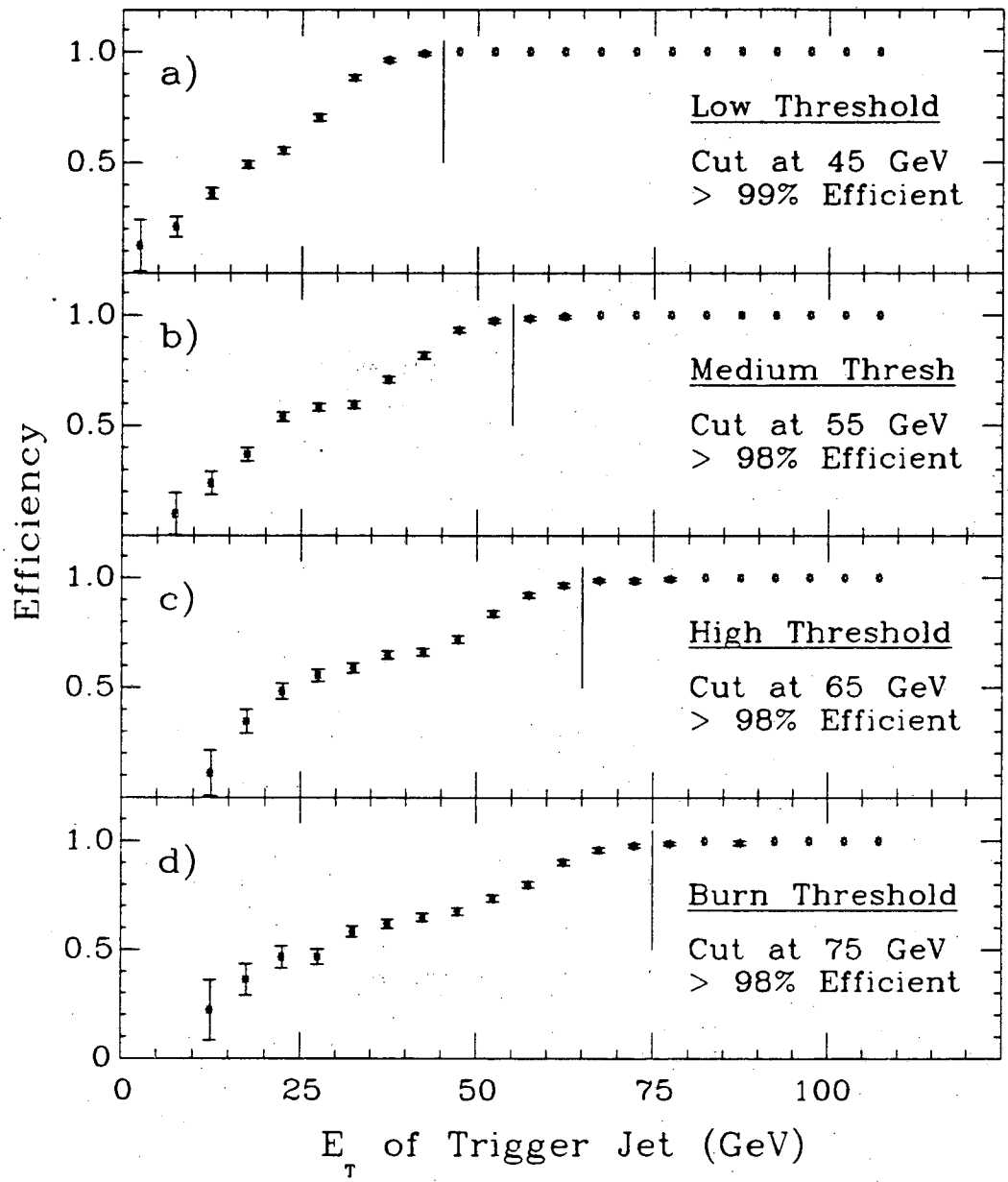

Figure 4.4: The efficiency of the combined hardware and software trigger for accepting a single trigger jet plotted versus corrected jet E_t. The efficiency is defined as the number of jets accepted by the trigger divided by the number produced. The efficiency and chosen minimum E_t cut, E_t^{thresh}, are shown for the four different hardware triggers present during the 1987 run: **a)** low threshold, **b)** medium threshold, **c)** high threshold, and **d)** burn threshold.

imately 25% higher than the uncorrected E_t seen by the hardware and software trigger. Thus, our trigger is efficient for jets with high E_t only.

4.7 Extension of Jet Energy Corrections

The central jet energy corrections, described in section 4.4, were calculated for jets in the detector pseudorapidity region $0.1 < |\eta_d| < 0.7$. Only 1% of trigger jets in the real pseudorapidity range $|\eta| < 0.6$, fall outside the region $|\eta_d| < 0.7$. However, 16% of trigger jets fall inside the region $|\eta_d| < 0.1$, which includes the 90° *crack* (see section 3.2.4). Rather than redo the work of the energy correction for our η range, it was decided to simply extend the existing energy corrections. This was done using the technique of two jet E_t *balance.*

The E_t balance technique uses the two leading jets from a sample of events in which one jet is in a *control* region and the other jet is in a *probe* region. By comparing the E_t of the jet in the probe region with the E_t of the jet in the control region, variations in detector response are measured. The difference in the E_t of the two leading jets along a "parallel" axis, shown in figure 5.1 and discussed at length in section 5.1, is a measurement of E_t response variations. This technique has been used to measure the response of the 90° crack, and also to measure variations in response as a function of trigger jet η.

4.7.1 90° Crack Jet E_t Correction

The ninety degree crack is shown in figure 3.6. As discussed in section 4.6.2, we used a sample of jets from the medium, high, and burn trigger samples, and required the dijet E_t be greater than 62, 80, and 90 GeV respectively. One jet was required to be in the control region where the jet energy correction is known ($0.1 < |\eta_d| < 0.7$) and the other jet was required to be in the crack region ($|\eta_d| < 0.1$). The average E_t loss in the crack region is shown in figure 4.5a.

The E_t loss was always greater than zero, however, the data indicates that only jets with $E_t > 31$ GeV require an E_t correction. Beyond 62 GeV the statistics

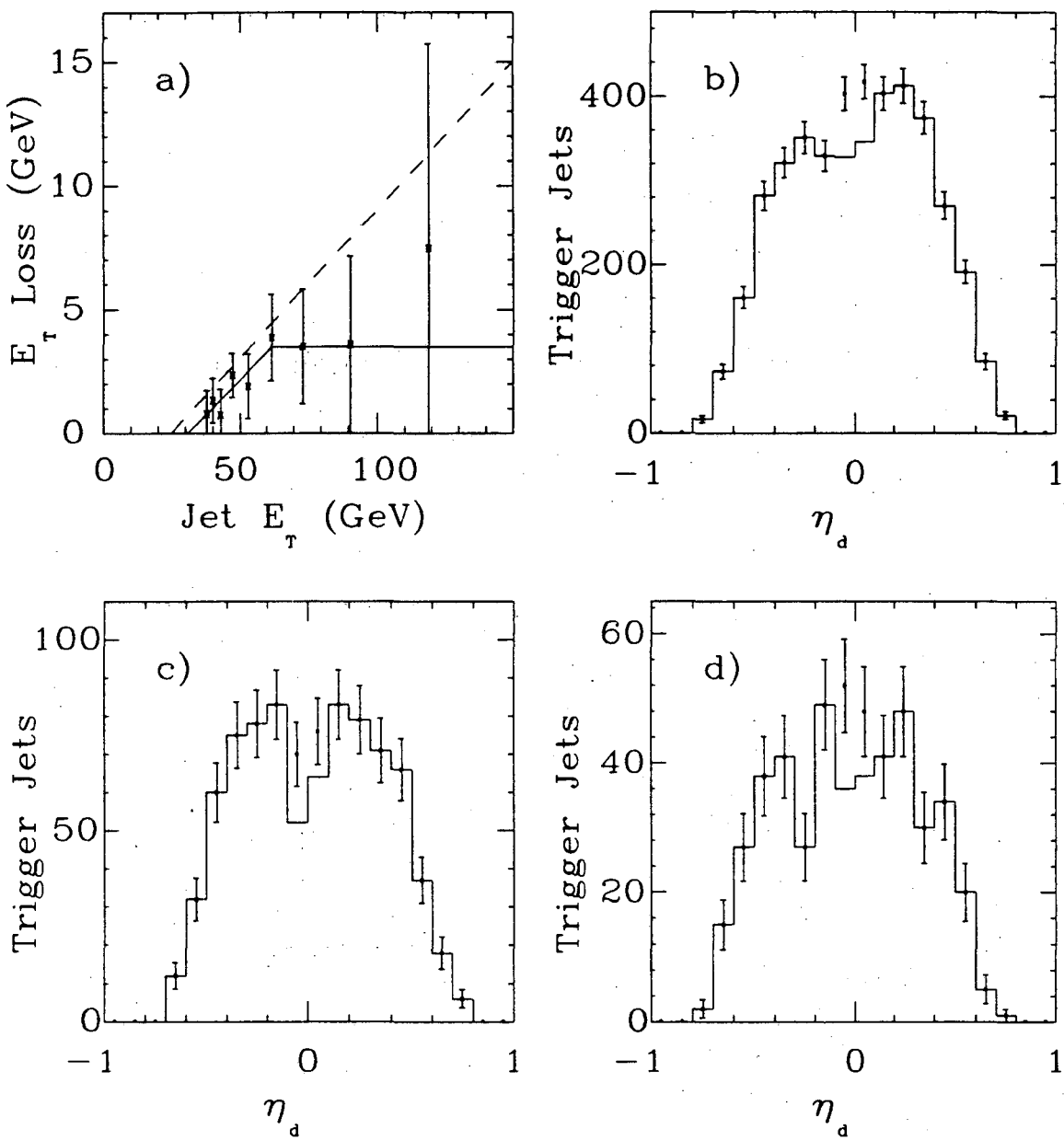

Figure 4.5: **a)** The transverse energy lost by a jet in the 90° crack (points) as a function of jet E_t. Also shown is the crack correction (solid) and an upper systematic bound (dashed). Plots **b)**, **c)**, and **d)** show the detector pseudorapidity distributions of trigger jets before (histogram) and after (points) crack correction for the medium, high, and burn trigger threshold respectively.

are poor, and the data is consistent with a constant E_t loss of 3.5 GeV. We defined the 90° crack correction, C_{crack}, to be

$$C_{crack} = \begin{cases} 0.0\ GeV & if \quad E_t < 31GeV \\ 0.113E_t - 3.5\ GeV & if \quad 31 < E_t < 62GeV \\ 3.5\ GeV & if \quad E_t > 62GeV \end{cases} \tag{4.12}$$

which is the solid line shown in figure 4.5. The correction is small compared to the original jet energy corrections in equation (4.10), particularly considering the crack correction is only applied to jets in the range $|\eta_d| < 0.1$. The η_d distribution of trigger jets before and after adding the crack correction is shown in figures 4.5b-d for the medium, burn, and high threshold samples. Before the crack correction is applied a distinct dip is observable in the η_d spectrum, because energy lost in the crack prevented some jets from passing the trigger jet E_t threshold. After correction, the dips in the region $|\eta_d| < 0.1$ are gone. This correction changed the total number of events in the two jet sample from 5096 to 5291. The dashed line in figure 4.5a is an estimate of the upper systematic bound on the crack correction, and zero is an estimate of the systematic lower bound.

4.7.2 η Dependent Jet E_t Correction

The η distribution of the trigger jet, after correction for energy lost in the 90° crack, was uniform for all the trigger samples except the medium sample shown in figure 4.6a. The data shows a region of slightly higher rate ($0 < \eta < 0.4$ has an excess of 15% in rate) and one bin with significantly lower rate ($0.5 < \eta < 0.6$ has 25% less rate) than standard QCD expectations normalized to the total jet rate. This variation in rate was translated directly into a variation in response, using the measured slope of the E_t spectrum ($N \sim 1/{E_t}^5$). The variation in response is shown in figure 4.6b. Studies of response using the E_t balance technique were also done. One trigger jet was in the control region defined as $|\eta| < 0.6$ and the variation in response was determined for varying η_1 of the other trigger jet. The variation in response from the E_t balance technique is also plotted in figure 4.6b.

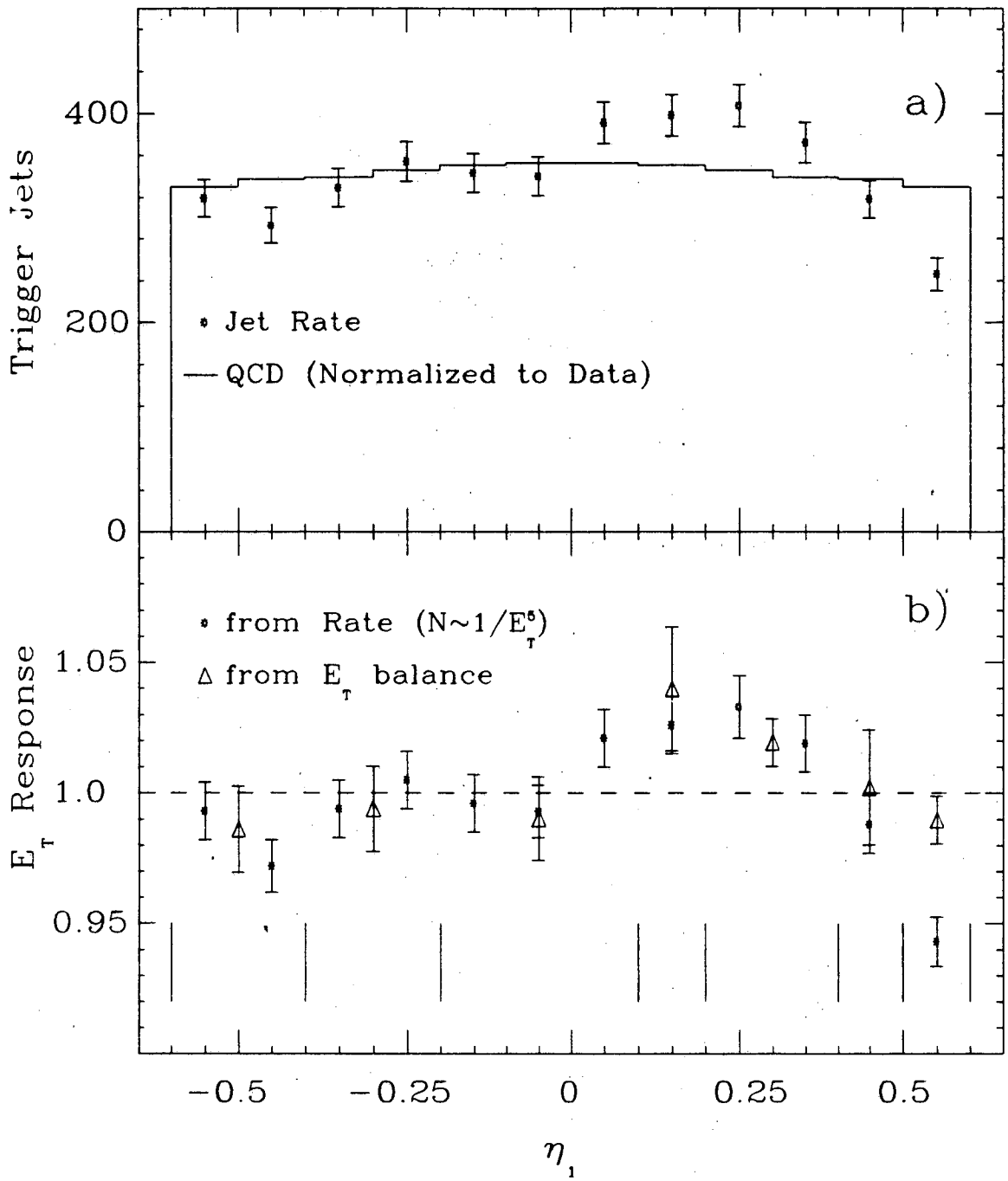

Figure 4.6: **a)** The trigger jet rate vs. η for the medium threshold sample compared to a QCD prediction normalized to the data. **b)** Relative response as a function of η derived from the rate, compared with relative response derived from E_t balance measurements.

These two techniques of measuring response, using the rate or using E_t balance, gave practically the same results, but the statistical significance of the former technique is better.

To understand this variation, we note that the medium sample has the largest mean z-vertex (5.5 cm), and when the z-vertex acceptance region was cut from $|z| < 60$ cm to $|z| < 10$ cm the distribution became uniform and constant. The effect of the shifted mean z-vertex was most likely causing the problem. The observed excess in rate is roughly expected from changes in effective sampling fraction with mean z-vertex.

We have used the response measurements derived from the rate to correct the E_t response of the trigger jet. As can be seen in figure 4.6b, the corrections vary from -3%, for the region $0.0 < \eta < 0.4$, to $+5\%$, for the region $0.5 < \eta < 0.6$, and represent an RMS deviation of 2.5% in the E_t response over the entire region $-0.6 < \eta < 0.6$. This variation is small, almost at the level of the systematic variation of the calibration. The variations in response were only apparent in the medium sample, and hence the corrections were only applied to that sample. The correction is small compared to the original jet energy corrections in equation (4.10). After the correction the η distribution of the trigger jet in the medium sample agrees with the η distributions in the low, high and burn samples. All distributions were relatively constant as a function of η. The correction was designed to leave the total number of events in the sample unchanged, though some events moved in and some events moved out.

4.8 Properties of the Data Sample

The final data sample after all corrections contained 5291 events. In this section the basic features of the leading jets are discussed.

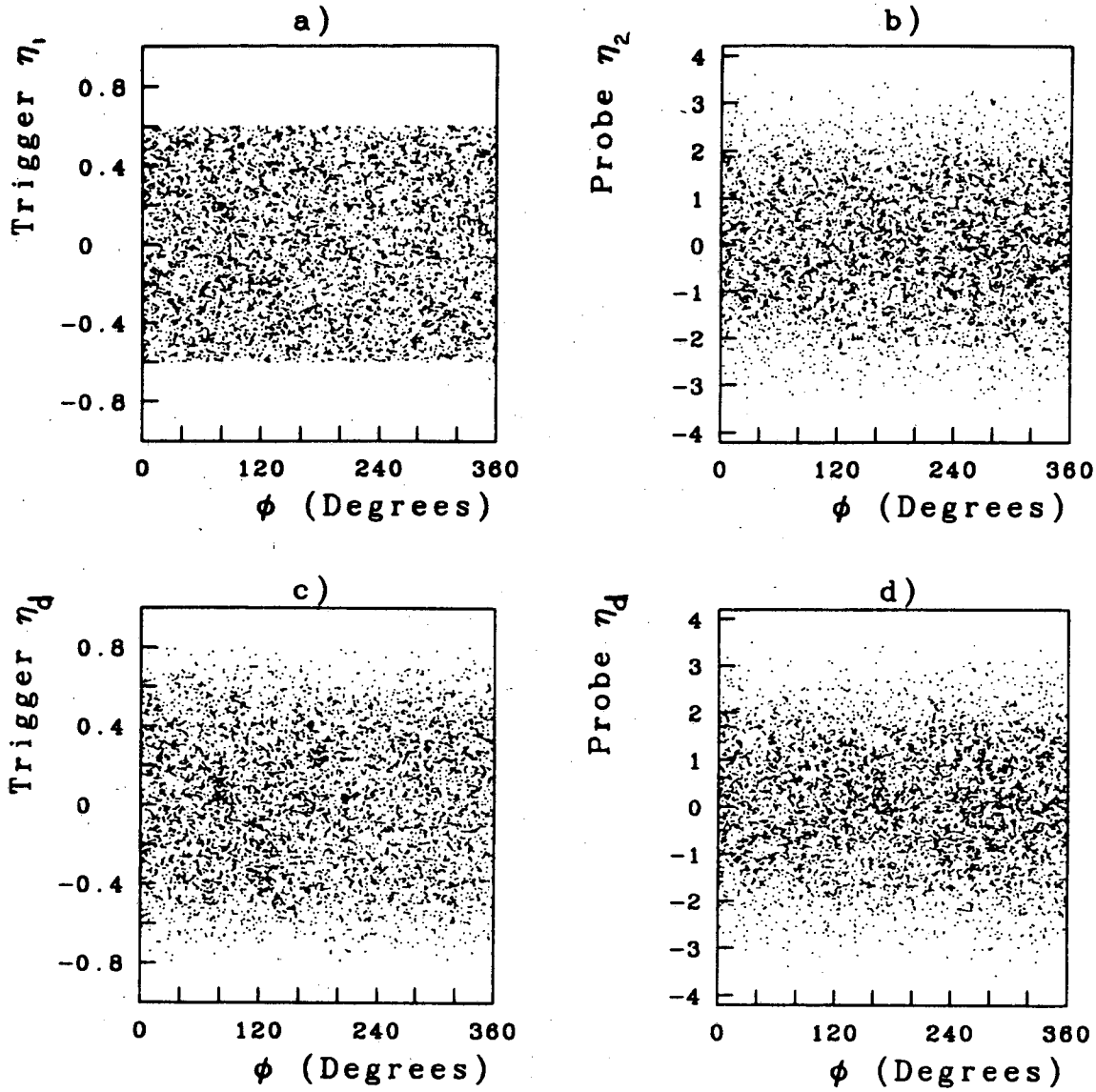

Figure 4.7: Scatter plots of pseudorapidity and azimuthal angle of the leading jets. **a)** and **b)** show the density of jets in $\eta\phi$ space for trigger and probe jets respectively. η was corrected for the location of the event z-vertex. **c)** and **d)** show the the density of jets in $\eta_d\phi$ space for trigger and probe jets respectively. η_d was not corrected for the location of the event z-vertex. Each plot contains 5795 leading jets.

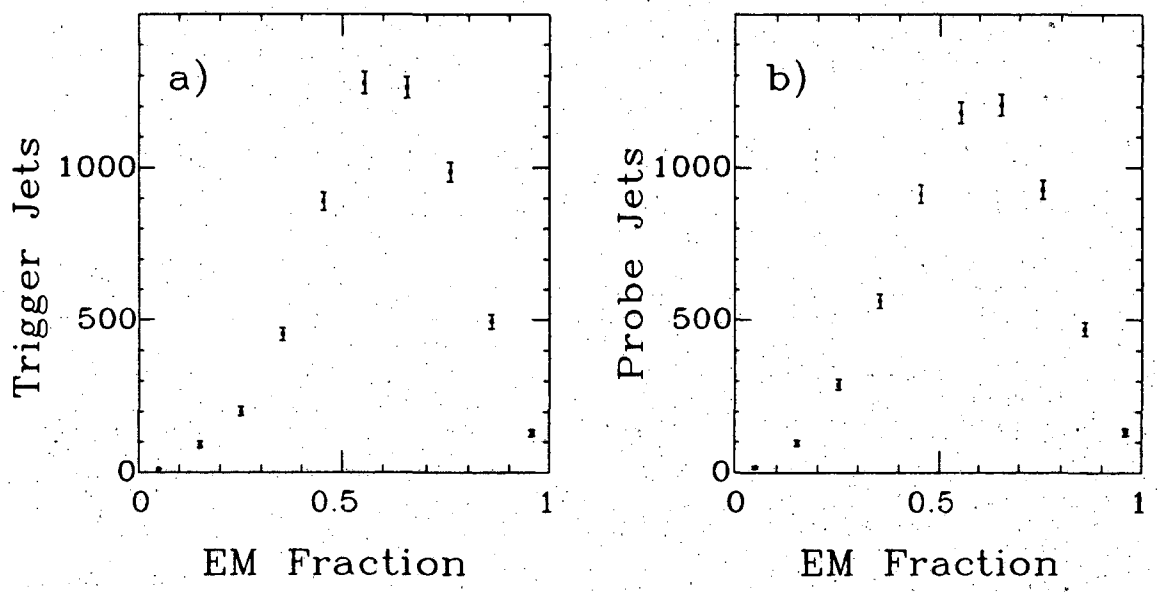

Figure 4.8: The fraction of a leading jets energy deposited in the electromagnetic calorimeter is shown for **a)** trigger jets and **b)** probe jets.

4.8.1 Data Sample Integrity

To demonstrate the integrity of the two jet data sample we present a few simple distributions. In figure 4.7a-b $\eta\phi$ *scatter* plots are presented for the trigger and probe jets respectively. In these scatter plots a single dot represents the $\eta\phi$ coordinates of a single jet. In figure 4.7a our cut at $|\eta_1| = 0.6$ is clearly visible. Figure 4.7b covers the unrestricted range of pseudorapidity available to the probe jet, and demonstrates the full coverage of the CDF detector for two jet physics. Figure 4.7c-d are $\eta_d\phi$ scatter plots, useful to spot detector problems such as hot spots with hardware-like topologies (rectangular excesses of dots in the plot) or dead regions (blank patches). It is clear on inspection of figure 4.7c, that no such problems exist in the central calorimeters. The sharp edge at $|\eta_1| = 0.6$ in figure 4.7a gets smeared out by the width of the z-vertex distribution, resulting in a blurred edge in figure 4.7c. The trigger jets at $\eta_d = \pm 0.8$ in figure 4.7c, correspond to jets with $\eta = \pm 0.6$ for which the event z-vertex was ± 60 cm. Finally, figure 4.7d shows the detector pseudorapidity of probe jets in the entire calorimeter. Note that there is no obvious hardware related noise: PEM spikes, cable noise, *etc.*.

Each of the scatter plots in figure 4.7 contains 5795 leading jets although there are only 5291 events in the final sample. As stated in section 4.3.3, when both leading jets are inside the pseudorapidity region $|\eta| < 0.6$ and they both have $E_t > E_t^{thresh}$, then they are both counted as trigger jets and probe jets as well. There are 504 such events where both jets satisfy the trigger, out of the total of 5291 events, giving a total of 5795 trigger jets and 5795 probe jets.

Another check of the quality of the two jet sample is the distribution of the fraction of a jet's total cluster energy that was deposited in electromagnetic calorimeters (EM Fraction). In figure 4.8 we show the distribution for trigger jets and probe jets separately. Excesses of electromagnetic energy would indicate a problem with the EM calorimeters, and would produce a spike at EM Fraction= 1. Similarly, spikes at EM Fraction= 0 would indicate a problem with the hadronic calorimeters. The absence of spikes in these distributions indicates that this leading jet sample is free of any significant calorimeter related problems.

4.8.2 η and E_t Distributions

The inclusive η and E_t distributions of each of the two leading jets are the most basic distributions of the two jet analysis. In figure 4.9a-b the η distributions of the trigger and probe jets are shown for the full sample. After correction for the 90° crack and the slight η_1 dependence of central response, as described in section 4.7, the η_1 distribution of trigger jets is flat near $\eta_1 = 0$ and falls gradually at larger values. The probe jets in figure 4.9b are not required to pass a specific E_t threshold, they are only required to be one of the two leading jets. Consequentially, the η_2 distribution is insensitive to most calorimeter response variations. However, E_t and η_2 resolution distort its shape, primarily at high $|\eta_2|$. The fall-off of the η_2 distribution is an expected result of the rapid decrease of the structure functions with increasing parton fractional momentum, as described in section 2.3.3.

The E_t distribution of the trigger jet falls rapidly ($dN/dE_t \sim 1/E_t^6$), as shown for the medium threshold sample in figure 4.10a. Within the parton model

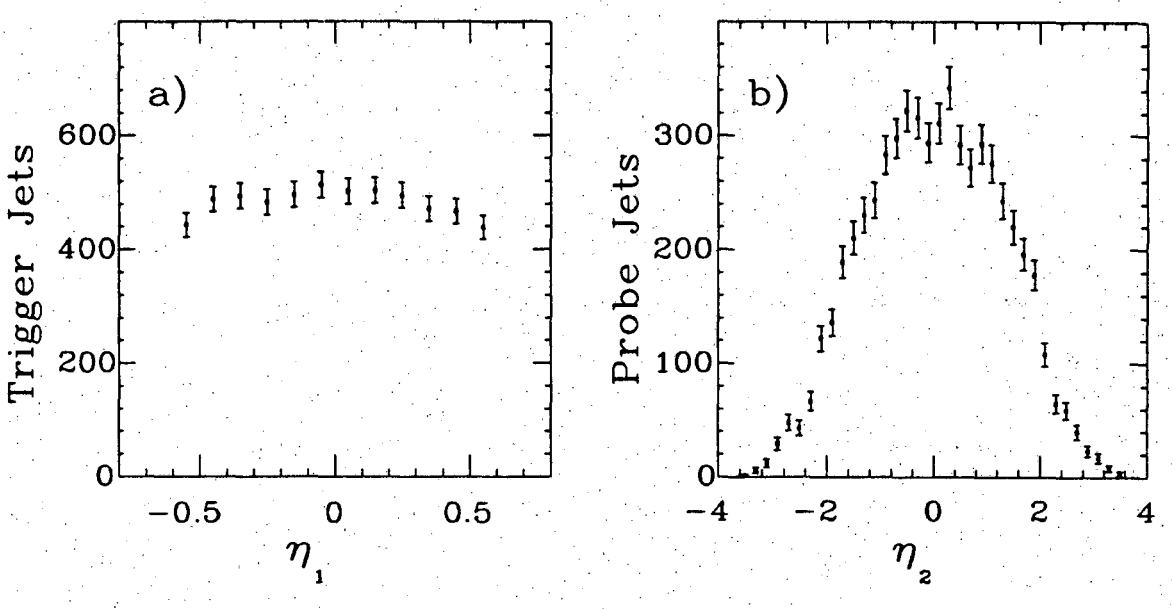

Figure 4.9: The η distributions of the two leading jets from the full sample are shown for **a)** trigger jets and **b)** probe jets. The distributions contain no corrections for E_t or η resolution smearing, and each plot contains 5795 jets.

the rapid fall-off with E_t is the result of many factors: the rapid decrease of the structure functions with increasing x, the fall-off of the subprocess cross section proportional to $1/\hat{s}^2$, and the slight decrease of α_s with increasing Q^2. In figure 4.10b the $E_{t,cluster}$ distribution of the probe jet is shown for leading jets from the medium threshold sample. The probe jet, unrestricted in pseudorapidity, was not corrected for jet E_t loss. The probe jet $E_{t,cluster}$ distribution peaks at around 40 GeV, which corresponds to the 55 GeV cut on trigger jet E_t, minus $\sim 20\%$ for E_t loss, and minus a few GeV to compensate for E_t resolution effects discussed in section 5.1. The E_t resolution causes the number of probe jets to smoothly decrease with decreasing $E_{t,cluster}$, in contrast to the sharp low E_t edge of the trigger jet distribution.

The trigger jet E_t distribution is dependent on the pseudorapidity of the probe jet. In figure 4.11 the E_t distribution of trigger jets from the medium threshold sample is shown for three different probe jet pseudorapidity intervals. The slope of the E_t distribution gets steeper as the pseudorapidity of the probe jet increases from $|\eta_2| = 0$ to large $|\eta_2|$. The parton model predicts this change in slope of the

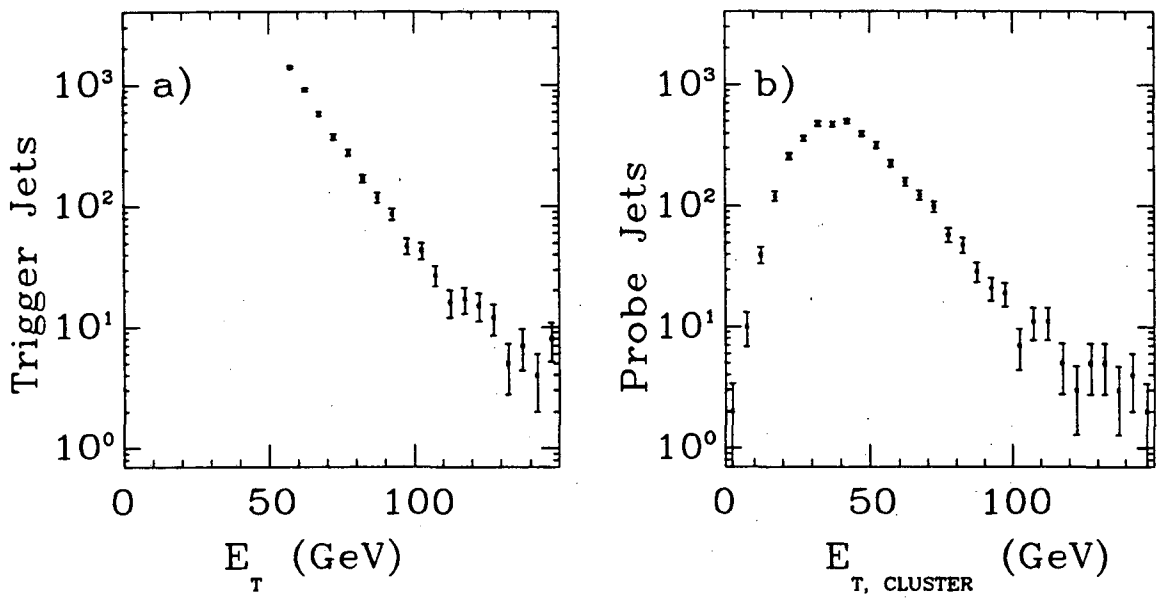

Figure 4.10: The E_t distributions of the two leading jets from the Medium Threshold sample. **a)** The "true" jet E_t of the trigger jet. **b)** The uncorrected cluster transverse energy of the probe jet. The distributions contain no corrections for E_t resolution smearing.

E_t distribution. At higher $|\eta_2|$ one of the partons is at relatively higher fractional momentum x. For this higher x, a given fractional change in E_t represents a larger absolute change in x. Since the structure functions behave roughly as e^{-x}, the larger absolute change in x produces a larger relative change in the rate, and the E_t distributions must fall more rapidly when $|\eta_2|$ is large.

The change in slope of the E_t distributions with $|\eta_2|$ has dramatic consequences for the measurement of the two jet differential cross section. In section 5.1 we discuss how the jet energy resolution combines with a steeply falling E_t spectrum to produce *resolution smearing* of jets with low E_t into higher E_t bins. This distortion of the produced spectrum increases when the jet E_t spectrum falls more rapidly. The E_t spectrum is steeper at high $|\eta_2|$ so we expect more E_t smearing at high $|\eta_2|$. The measurement of the effects of resolution smearing on the two jet differential cross section, as a function of E_t and η_2, was the greatest challenge in this analysis. The method used to estimate and remove the distortions produced

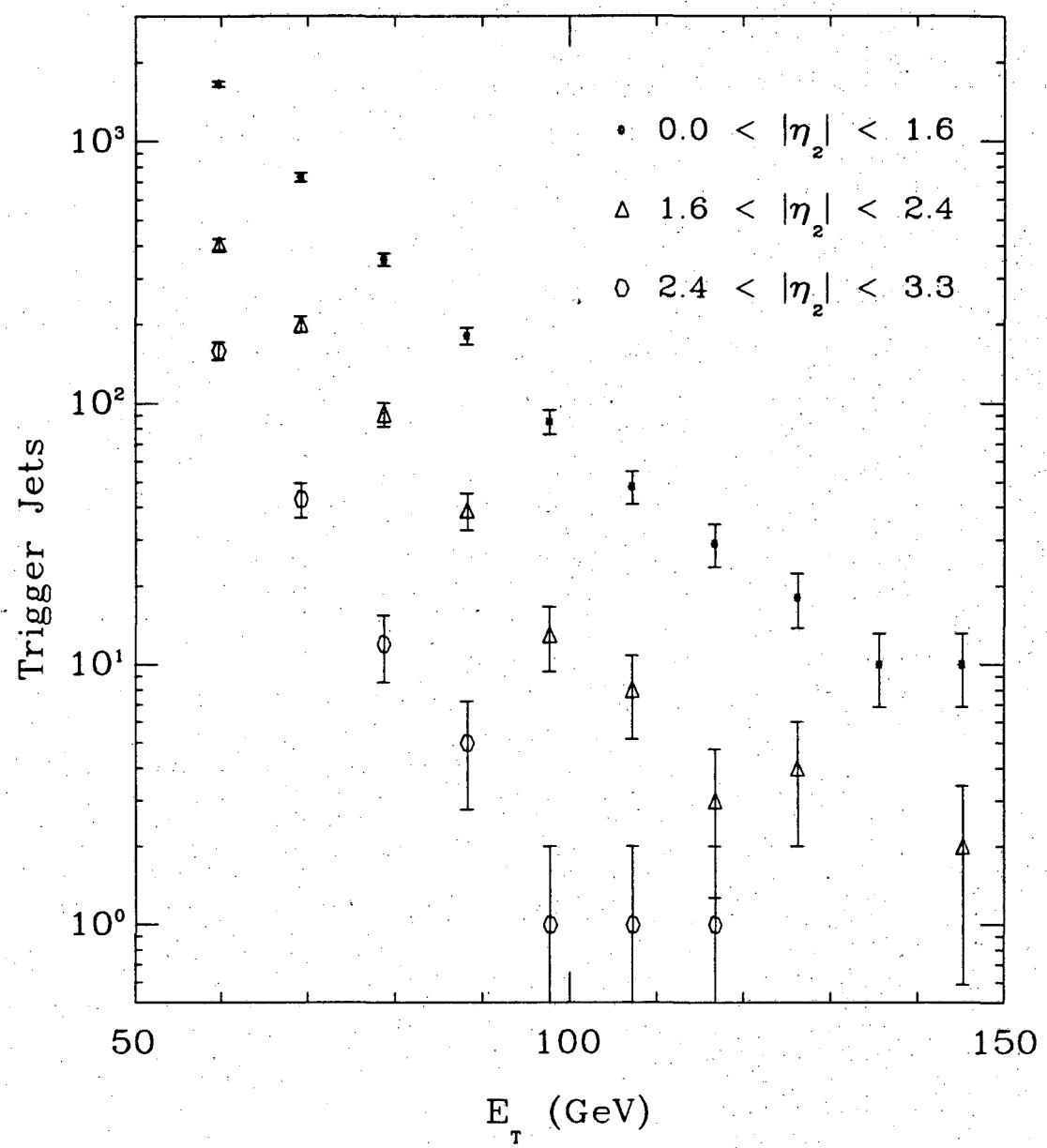

Figure 4.11: The number of trigger jets as a function of jet E_t is shown for leading jets from the medium sample. The E_t distribution is plotted separately for three different intervals of pseudorapidity of the probe jet. Note how the slope of the E_t distribution gets steeper as $|\eta_2|$ increases.

by resolution smearing is discussed in section 5.1.

4.8.3 Uncorrected Two Jet Differential Cross Section

The two jet differential cross section, without any corrections for resolution smearing, is shown in figure 4.12. The bulk of the data is contained in the three E_t intervals which span from 55 GeV to 100 GeV. For each E_t interval and $|\eta_2|$ bin, the total number of trigger jets in the single pseudorapidity bin $|\eta_1| < 0.6$ is included. The raw two jet differential cross section, indicated by the height of each point, is the number of trigger jets in an interval of trigger jet E_t and a bin of probe jet $|\eta_2|$, divided by the total luminosity for that bin and the total bin width. The bin width is just the width of the E_t interval, times the width of the η_2 bin, times the fixed width of the η_1 bin. The errors are statistical only. The raw cross section for the lowest E_t interval comes from the low threshold sample only; the statistics in this E_t interval are poor. Bins with 10 trigger jets or fewer, all at the high $|\eta_2|$ edge of the sample, are omitted from the plot and this analysis.

At low $|\eta_2|$ the raw cross section is about 40% larger than a typical leading order QCD expectation, and at $|\eta_2| = 2.6$ the raw cross section is as much as 400% larger than a typical leading order QCD expectation. As will be shown in section 5.1, this excess rate is the result of resolution smearing, primarily the feeddown of many low E_t jets into higher E_t bins. Although distorted by resolution effects, figure 4.12 shows the basic features of the two jet differential cross section. The cross section decreases with the E_t of the trigger jet and with the $|\eta_2|$ of the probe jet, and a slight rapidity plateau is visible at $|\eta_2| = 0$ for the three E_t intervals with the highest statistics.

4.8.4 Two Jet Dominance

The primary indication of two jet dominance in $\bar{p}p$ collisions is the presence of two high energy clusters with roughly equal E_t located in azimuthally opposite hemispheres. We have already used E_t balance to obtain E_t corrections for the

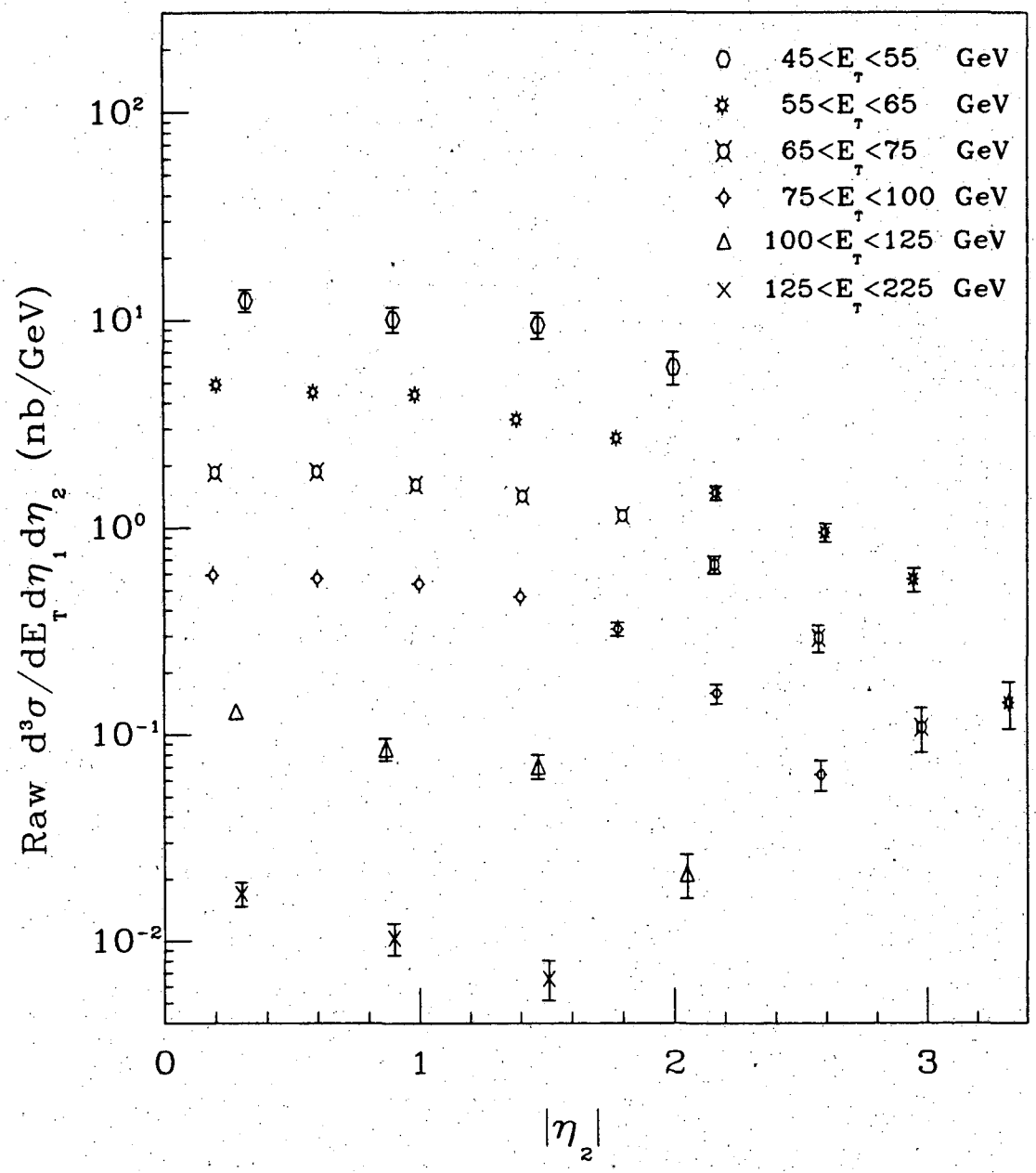

Figure 4.12: The raw two jet differential cross section. The raw cross section, for finding a trigger jet with pseudorapidity within $|\eta_1| < 0.6$ and E_t within an E_t interval when a probe jet is within a given $|\eta_2|$ bin, is shown for 6 different trigger jet E_t intervals. The raw cross section has not been corrected for resolution smearing.

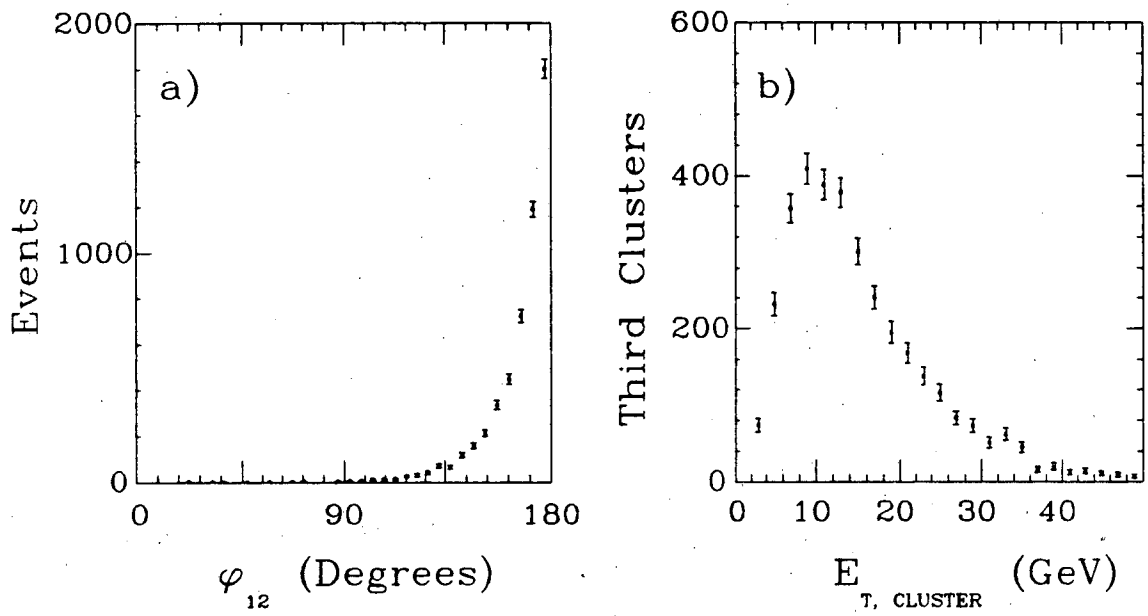

Figure 4.13: **a)** The distribution of the azimuthal separation of the two jets, showing a clear *back-to-back* peak at $\phi_{12} = 180°$. **b)** The distribution of uncorrected cluster transverse energy for the cluster with the third highest E_t.

two jet sample in section 4.7, and it will be used to determine the E_t resolution in section 5.1; the E_t resolution is about 12 GeV for a 50 GeV jet. In figure 4.13a the azimuthal angle between the trigger and probe jets, ϕ_{12}, is shown for the full sample of 5291 events. Note that the distribution peaks sharply at $\phi_{12} = 180°$, and falls off in an approximately Lorentzian distribution about this *back-to-back* position. The overwhelming peak at $\phi_{12} = 180°$ indicates two jet dominance, while the long low "tail" is produced by the presence of other clusters in the event. Other clusters in the event are associated with QCD final state radiation, and other deviations from $2 \rightarrow 2$ QCD described in section 2.1.6. The ϕ_{12} distribution of events with only two clusters had no "tail". It was peaked at $\phi_{12} = 180°$ and ended abruptly at about $\phi_{12} = 145°$, which demonstrates that the tail on the ϕ_{12} distribution is associated with the presence of other clusters.

Another indication of two jet dominance is that a substantial fraction (35%) of the events had only two clusters, while in the remainder of the events the E_t of the third cluster was relatively small. From events with three or more clusters,

the distribution of $E_{t,cluster}$ for the third cluster is shown in figure 4.13b. The average $E_{t,cluster}$ for the third cluster (15 GeV) is much less than the average $E_{t,cluster}$ of the trigger jet (60 GeV). The distribution rises continuously with decreasing $E_{t,cluster}$ before rolling off at around 10 GeV; the roll-off is caused by inefficiencies within the clustering algorithm for very low E_t clusters. The angular distribution of jets in events with energetic third clusters is the same as for two jet events[68], indicating that extra clusters come primarily from QCD radiation superimposed on a $2 \rightarrow 2$ event. The above discussion has presented some of the reasons why we believe that deviations from $2 \rightarrow 2$ production are merely perturbations, and that two jet production is dominant. We analysed all events with two or more clusters, and corrected the two jet differential cross section for distortions induced by calorimeter resolution and QCD deviations from $2 \rightarrow 2$ production, as discussed in the following chapter.

Chapter 5

Resolution

5.1 E_t and η_2 Resolution

The E_t resolution and η_2 resolution, as a function of jet E_t, have been measured using jet data. The resolution is defined as the average deviation of our measured E_t and η_2 from what would have been the E_t and η_2 of a $2 \rightarrow 2$ event measured by a calorimeter with perfect resolution. The presence of initial state and final state radiation, as well as hard higher order processes, insures that there will be some events that deviate from $2 \rightarrow 2$ kinematics. Finite detector resolution and QCD radiation will alter the E_t of the central jet and the η_2 of the other jet. When we correct the two jet differential cross section for distortions caused by the E_t and η_2 resolution, we correct for the average combined effect of detector resolution and QCD radiation.

To measure both the E_t and η_2 resolution we use the technique of E_t *balance*, first introduced by UA2[23,69] and later adopted by CDF[70]. For a $2 \rightarrow 2$ event in a perfect calorimeter, momentum conservation requires the P_t of the first jet to be equal to the P_t of the second jet. E_t equals P_t for massless partons, so we naively expect the E_t of the first jet to "balance" the E_t of the second jet. Calorimeter resolution and QCD radiation produce fluctuations in E_t, which result in E_t imbalance for an event, though we expect the E_t of the leading jets to balance

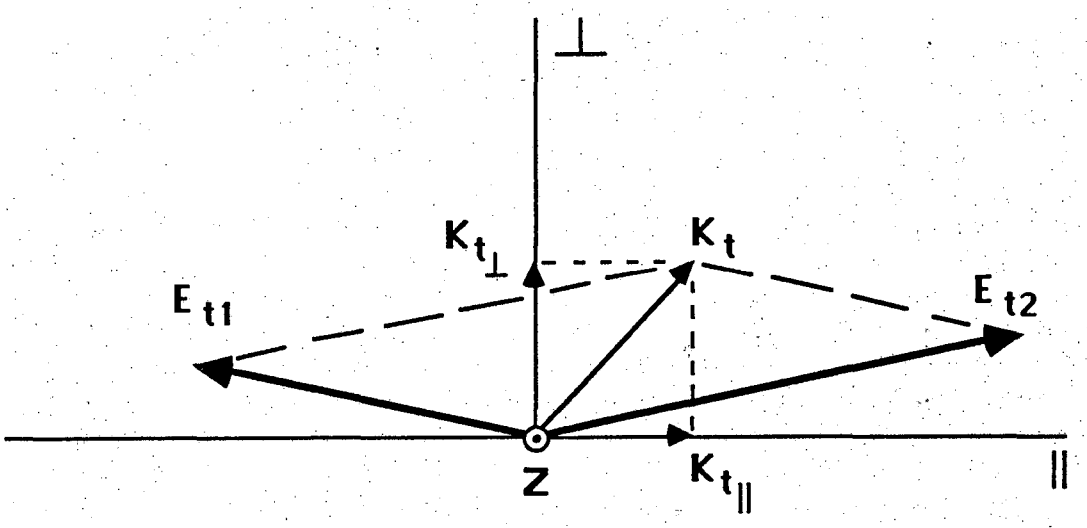

Figure 5.1: The E_t balance technique. The E_t vectors of two leading central jets in the transverse plane are shown. The $\perp$ axis is the perpendicular bisector of ϕ_{12} (the azimuthal angle between the two jets). The $\parallel$ axis is orthogonal to the $\perp$ axis in the transverse plane. K_t, the vector sum of E_{t_1} and E_{t_2}, is shown with its component along the parallel axis, $K_{t_\parallel}$, and its component along the perpendicular axis, $K_{t_\perp}$.

on average for any large ensemble of events. Fluctuations in E_t, including any caused by equating jet E_t with parton P_t, are reflected in the E_t balance measurement and therefore in the E_t resolution function.

Define the vector $\vec{K}_t$ as the vector sum of the E_t of the two leading jets in the plane transverse to the incident beams:

$$\vec{K}_t = \vec{E}_{t_1} + \vec{E}_{t_2}. \tag{5.1}$$

$\vec{K}_t$ is pictured in figure 5.1. Define the $\perp$ axis of the two jets in the transverse plane to be the perpendicular bisector of, ϕ_{12}, the angle between jet 1 and jet 2 in the transverse plane, as pictured in figure 5.1. Define the $\parallel$ axis of the two jets in the transverse plane to be orthogonal to the perpendicular bisector of the the two jets E_t vectors, as pictured in figure 5.1. Divide $\vec{K}_t$ into two components, one along the

parallel axis

$$K_{t_\parallel} = (E_{t_1} - E_{t_2}) \sin(\frac{\phi_{12}}{2}) \tag{5.2}$$

and one along the perpendicular axis

$$K_{t_\perp} = (E_{t_1} + E_{t_2}) \cos(\frac{\phi_{12}}{2}). \tag{5.3}$$

Fluctuations in $K_{t_\parallel}$, caused by the energy resolution of the calorimeter for jets and by QCD radiation, are related to a single jet's E_t resolution by the approximate relation

$$E_t \; Resolution \approx \frac{K_{t_\parallel} Resolution}{\sqrt{2}}. \tag{5.4}$$

Equation 5.4 is the consequence of enforcing $2 \rightarrow 2$ kinematics. The $\sqrt{2}$ follows from the assumption that the fluctuation in each leading jets E_t is an independent fluctuation, and the fluctuations of the two leading jets add in quadrature to give the measured $K_{t_\parallel}$ resolution. Fluctuations in $K_{t_\perp}$, caused by the angular resolution of the calorimeter for jets and by QCD radiation, are related to the η_2 resolution by the approximate relation

$$\eta_2 \; Resolution \approx \frac{K_{t_\perp} Resolution}{\sqrt{2}\; E_t}. \tag{5.5}$$

Equation (5.5) follows from the assumption that a two jet system receives a $K_{t_\perp}$ "kick" which is azimuthally symmetric with respect to the jet axis as outlined in Appendix A.3. In simple terms, we are using the ϕ resolution as an estimate of the η resolution, which is a good approximation since angular deviations are primarily caused by QCD radiation.

The typical shapes of $K_{t_\parallel}$ and $K_{t_\perp}$ distributions are seen in figure 5.2 for average jet E_t between 50 and 100 GeV. The $K_{t_\parallel}$ distribution, dominated by calorimeter resolution, is approximately Gaussian. The slight excess of events on the tail is caused by the width of the E_t bin; the distributions used for the E_t resolution analysis, in narrower bins of E_t, were more Gaussian (see section 5.1.1). The $K_{t_\perp}$ distribution, dominated by QCD radiation, was approximately Lorentzian.

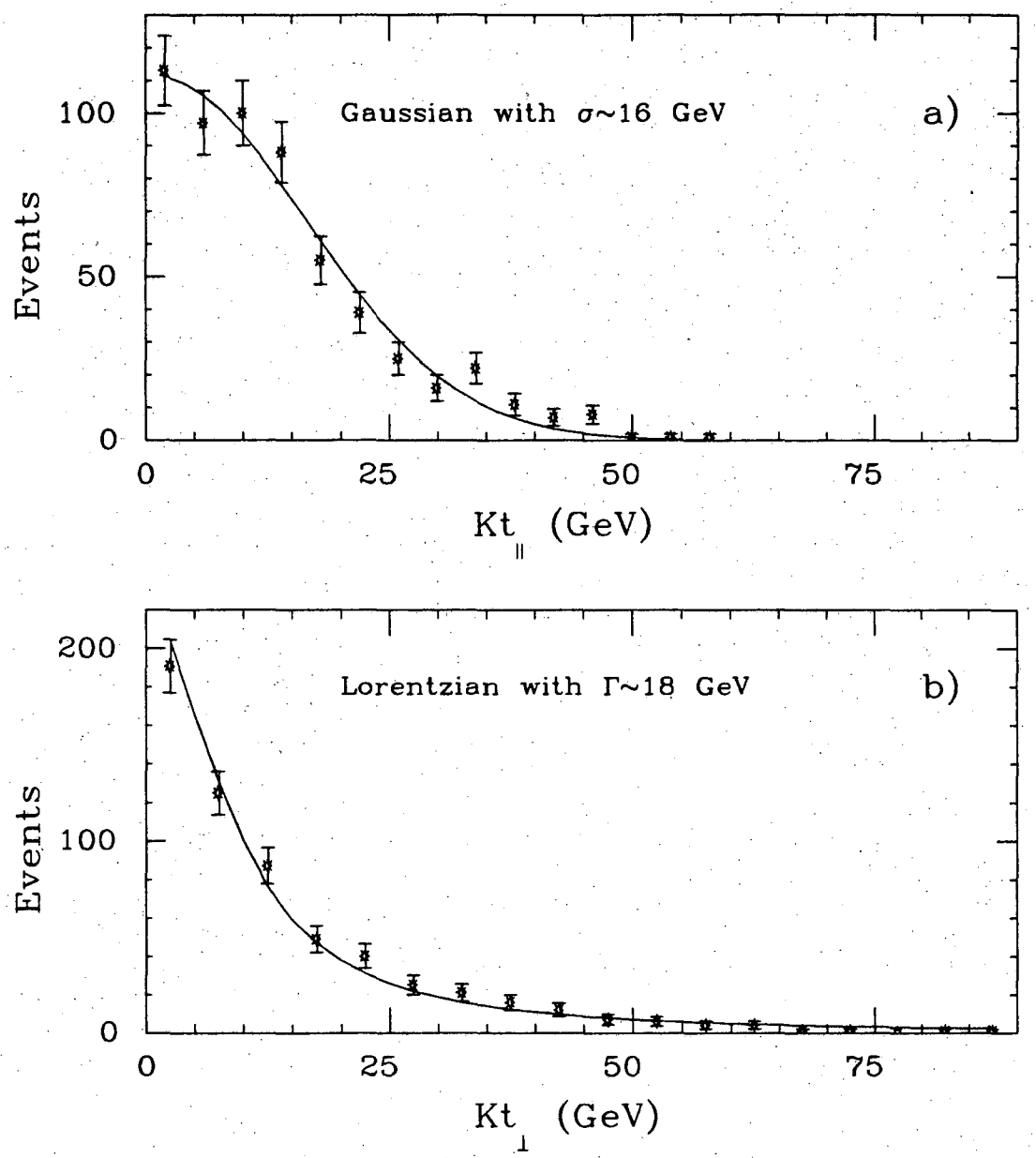

Figure 5.2: K_t distributions for average jet E_t of $50 < \overline{E_t} < 100$ GeV. **a)** The $K_{t_\parallel}$ distribution and Gaussian fit. **b)** The $K_{t_\perp}$ distribution and Lorentzian fit.

5.1.1 E_t Resolution and Systematic Uncertainty

The $K_{t_\parallel}$ resolution in the central calorimeter was measured from the sample of jets in which both jets were in the region $|\eta| < 0.6$. This sample had the same cuts as the complete sample, except a dijet E_t cut was substituted for the single jet E_t cut, as described in section 4.6.2. The $K_{t_\parallel}$ resolution was measured for 9 bins of $\overline{E_t}$ of the two jet system ($\overline{E_t} = (E_{t_1} + E_{t_2})/2$). The bin widths were chosen to keep the number of events in a bin from decreasing too quickly with E_t. The lower edge of the first bin was at $\overline{E_t} = 37.5$ GeV, and the upper edge of the last bin was at $\overline{E_t} = 150$ GeV. The lower edge was chosen higher than the minimum allowed lower edge of 31 GeV to avoid any possibility of trigger bias. The lowest resolution value measured is approximately 1.7σ below the E_t threshold for trigger jets in the medium sample.

The resolution was measured as a function of $\overline{E_t}$ of the two jets, as opposed to E_t of a single jet, to avoid the bias caused when a single jet fluctuates up into an E_t bin, thus causing a net $K_{t_\parallel}$ imbalance. This is what would occur most of the time since the measurements are made on a steeply falling E_t spectrum. By binning in the $\overline{E_t}$ of the two jets and measuring the $K_{t_\parallel}$ distribution, the measurement is only biased towards high fluctuations in $\overline{E_t}$. These fluctuations do not occur as often as high fluctuations in a single E_t, and do not affect the E_t difference which is the measurement of the resolution. This has been checked with a simple monte carlo.

A scatter plot of $K_{t_\parallel}$ versus the dijet E_t is given in figure 5.3a. Projections on the $K_{t_\parallel}$ axis, in 3 of the 9 bins of $\overline{E_t}$ used in the resolution measurement, are shown in figures 5.3b-d with Gaussian fits. We have simply used the RMS deviation of the measured distribution, one σ for each of the nine $\overline{E_t}$ bins, as a measure of the Gaussian $K_{t_\parallel}$ resolution function.

From the measurement of $K_{t_\parallel}$ resolution as a function of $\overline{E_t}$, the E_t resolution as a function of $\overline{E_t}$ is determined using equation (5.4). The effect of the E_t resolution itself on the measurement of $\overline{E_t}$ has been accounted for in a simple

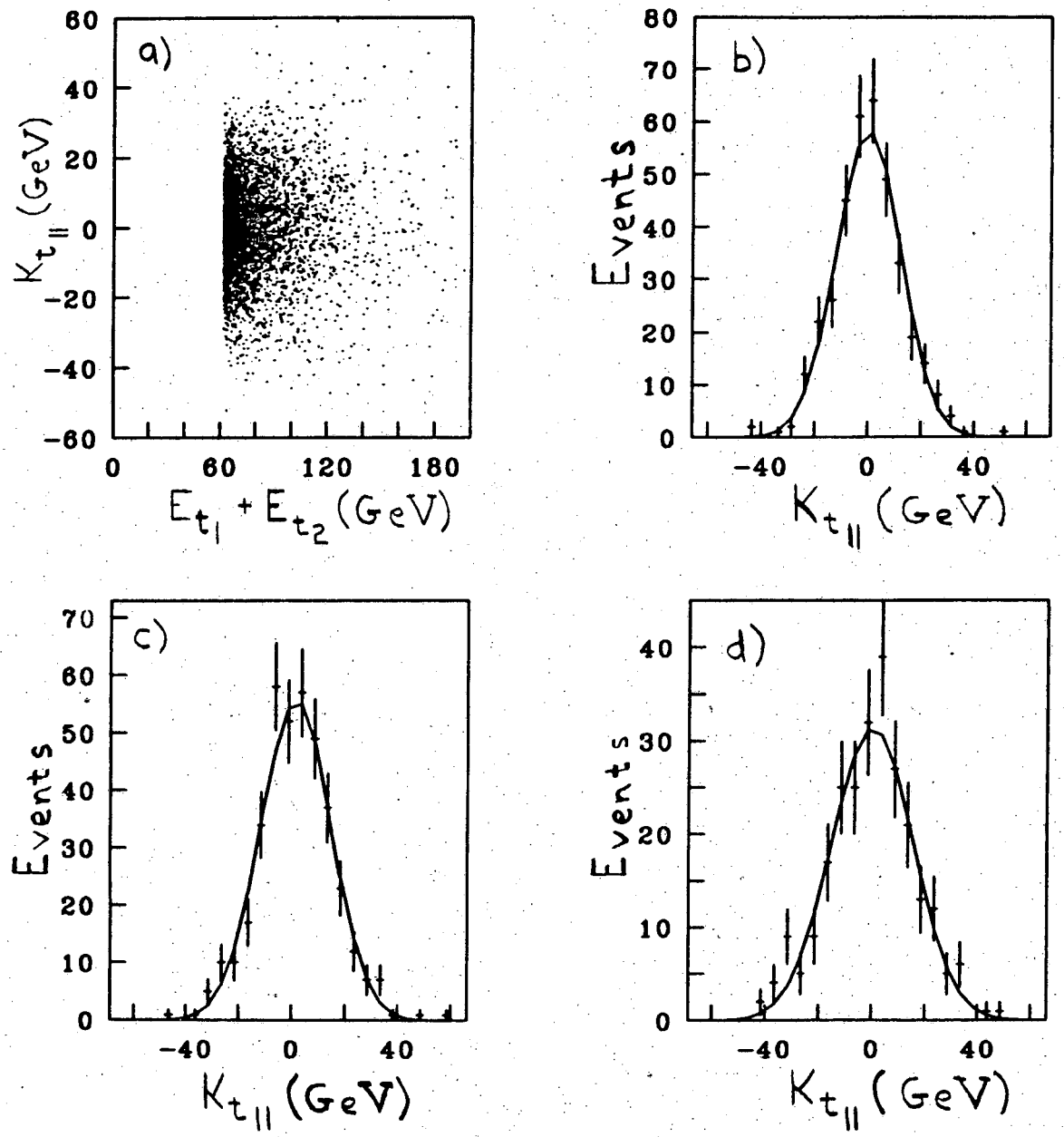

Figure 5.3: $K_{t_\parallel}$ distributions. **a)** A scatter plot of $K_{t_\parallel}$ versus the sum of the two leading jets E_t. **b)** $K_{t_\parallel}$ distribution for $75 < E_{t1} + E_{t2} < 79$ GeV fit to a Gaussian of width $\sigma = 12$ GeV. **c)** $K_{t_\parallel}$ distribution for $84 < E_{t1} + E_{t2} < 91$ GeV fit to a Gaussian of width $\sigma = 13$ GeV. **d)** $K_{t_\parallel}$ distribution for $102 < E_{t1} + E_{t2} < 117$ GeV fit to a Gaussian of width $\sigma = 15$ GeV.

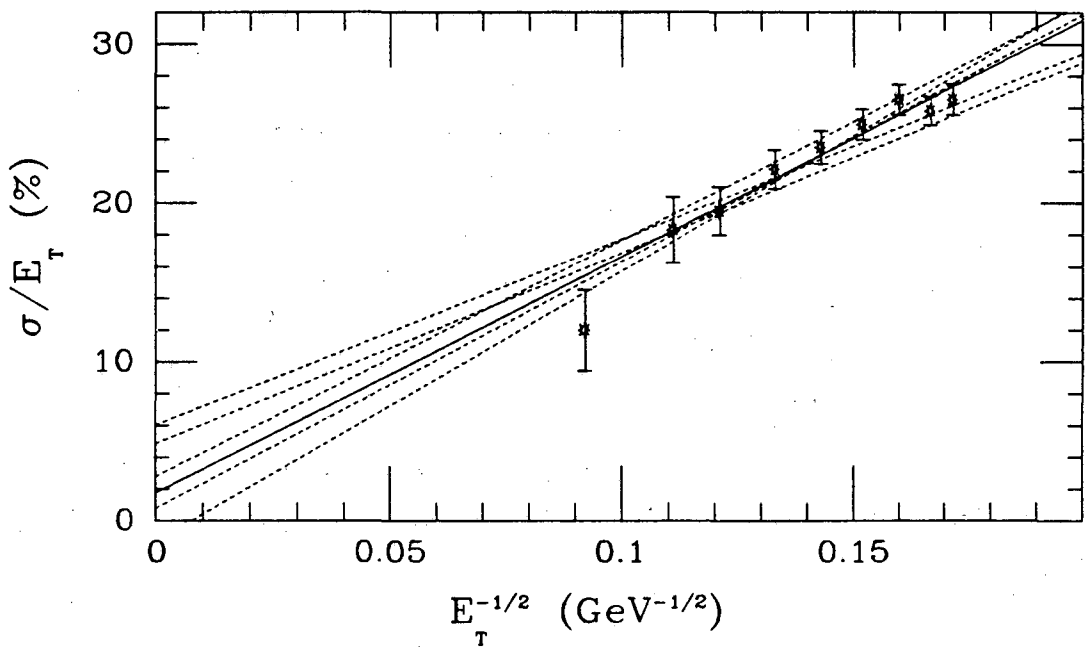

Figure 5.4: The Gaussian E_t resolution of the two jet system, including the effects of QCD radiation, fit with a straight line (solid) as a function of $1/\sqrt{E_t}$. The dotted lines are estimates of systematic bounds on the resolution function.

unsmearing exercise using the measured slope of the E_t spectrum, feeding the first E_t resolution in and calculating the shift in measured $\overline{E_t}$, calculating a new E_t resolution function, feeding that in to get a new $\overline{E_t}$ and so forth until convergence was attained. The net shift in the first resolution function was small, amounting to between a -6% change in the E_t of the lowest E_t bin and a -4% change in the highest E_t bin. Finally, in figure 5.4, we plot the corrected E_t resolution versus $1/\sqrt{E_t}$. The best linear fit, shown as a solid line in figure 5.4, is our "standard" E_t resolution function,

$$\sigma(E_t) = \frac{148.7\%}{\sqrt{E_t}} + 1.77\%. \tag{5.6}$$

The fit had 7 degrees of freedom and a chi-square per degree of freedom of 0.7.

The systematic uncertainty in the slope of the E_t resolution function was estimated from the systematic uncertainty in the jet E_t. A 10% uncertainty in the jet E_t scale (see section 4.4) produces a 5% uncertainty in the slope of the E_t resolution function. The correction to the resolution function for resolution smearing gives a

net shift of about 5% in jet E_t, and produces a 2.5% change in the slope of the E_t resolution function, which we take as an additional uncertainty. Combining the two uncertainties in quadrature gives a systematic uncertainty of 5.6% on the slope of the resolution function.

To estimate maximum and minimum resolution functions we held the slope of the "standard" E_t resolution function constant and varied the offset until the chisquared of the linear fit changed by 1. This indicated that for a fixed slope the offset in equation (5.6) is $1.77\% \pm 1\%$. Then we multiplied the slope of the resolution functions by $1 \pm .056$ to account for the systematic uncertainty in the slope of the resolution function, as discussed above. This gave a resolution function with maximum slope in which the function is always above the "standard" result

$$\sigma(E_t) = \frac{157\%}{\sqrt{E_t}} + 2.77\% \tag{5.7}$$

and one with minimum slope always below the "standard" result

$$\sigma(E_t) = \frac{140\%}{\sqrt{E_t}} + 0.77\%. \tag{5.8}$$

We estimated two resolution functions skew to our "standard result" by the 1 σ statistical bound on the slope where the offset was free to vary. Here "skew" means that the resolution function intersects our standard result: higher slope and lower offset, or lower slope and higher offset. We found that the mean slope was $148.7\% \pm 20.2\%$ corresponding to a mean offset of $1.77\% \mp 3.08\%$. The resolution function skew to our "standard" result with maximum slope is

$$\sigma(E_t) = \frac{170\%}{\sqrt{E_t}} - 1.3\%. \tag{5.9}$$

The corresponding minimum slope result was almost as skew as a resolution function we obtained from a P_t balance measurement; this used the variable $P_t \equiv (P_x^2 + P_y^2)^{0.5}$ as opposed to E_t. The P_t result intersected the "standard" result with a smaller slope, and it was used as the resolution function skew to our "standard" result with minimum slope:

$$\sigma(E_t) = \frac{117\%}{\sqrt{E_t}} + 6.0\%. \tag{5.10}$$

These four resolution functions, shown as dotted lines in figure 5.4, are estimates of bounds on the E_t resolution at the 1 σ level.

5.1.2 η_2 Resolution and Systematic Uncertainty

The $K_{t_\perp}$ resolution in the central calorimeter was measured using the same sample of jets as in section 5.1.1, except the lower edge of the dijet E_t cut was left at 62 GeV. Fits of $K_{t_\perp}$ distributions to Gaussians were poor. Instead, $K_{t_\perp}$ distributions were fit with Lorentzian distributions, whose single parameter Γ, the full width at half maximum (FWHM), defines the $K_{t_\perp}$ resolution. Γ was then measured as a function of E_t, and related directly to the η_2 resolution via equation (5.5).

A scatter plot of $K_{t_\perp}$ versus dijet E_t is given in figure 5.5a. Projections on the $K_{t_\perp}$ axis, in 3 of the 8 bins used in the resolution measurement, are shown in figures 5.5b-d. The distributions have been folded about $K_{t_\perp} = 0$ to maximize statistical accuracy, and fit with Lorentzians centered on $K_{t_\perp} = 0$. The Lorentzian fits are truncated at $K_{t_\perp} = 2E_t$ since $K_{t_\perp}$ cannot exceed this value. The fits gave Γ for 8 values of $\overline{E_t}$, which when fit to a straight line gives

$$\Gamma_{K_{t_\perp}}(E_t) = 12 + .11E_t \ \ (GeV). \tag{5.11}$$

The fit had 6 degrees of freedom and a chi-square per degree of freedom of 1.2. Substitution of equation (5.11) into equation (5.5) gives the "standard" η_2 resolution function:

$$\Gamma_{\eta_2}(E_t) = \frac{8.77}{E_t} + 0.074 \tag{5.12}$$

The η_2 resolution values are shown in figure 5.6 together with the "standard" η_2 resolution function.

The Lorentzian η_2 resolution can be crudely related to a Gaussian, for the purpose of comparison with other measurements, by dividing it by 2.36. Doing this for the "standard" η_2 resolution function gives a Gaussian η_2 RMS deviation of about .1 for 50 GeV jets, falling to about .06 for 150 GeV jets. This is generally much larger than the detector resolution, which is known from tracking measurements

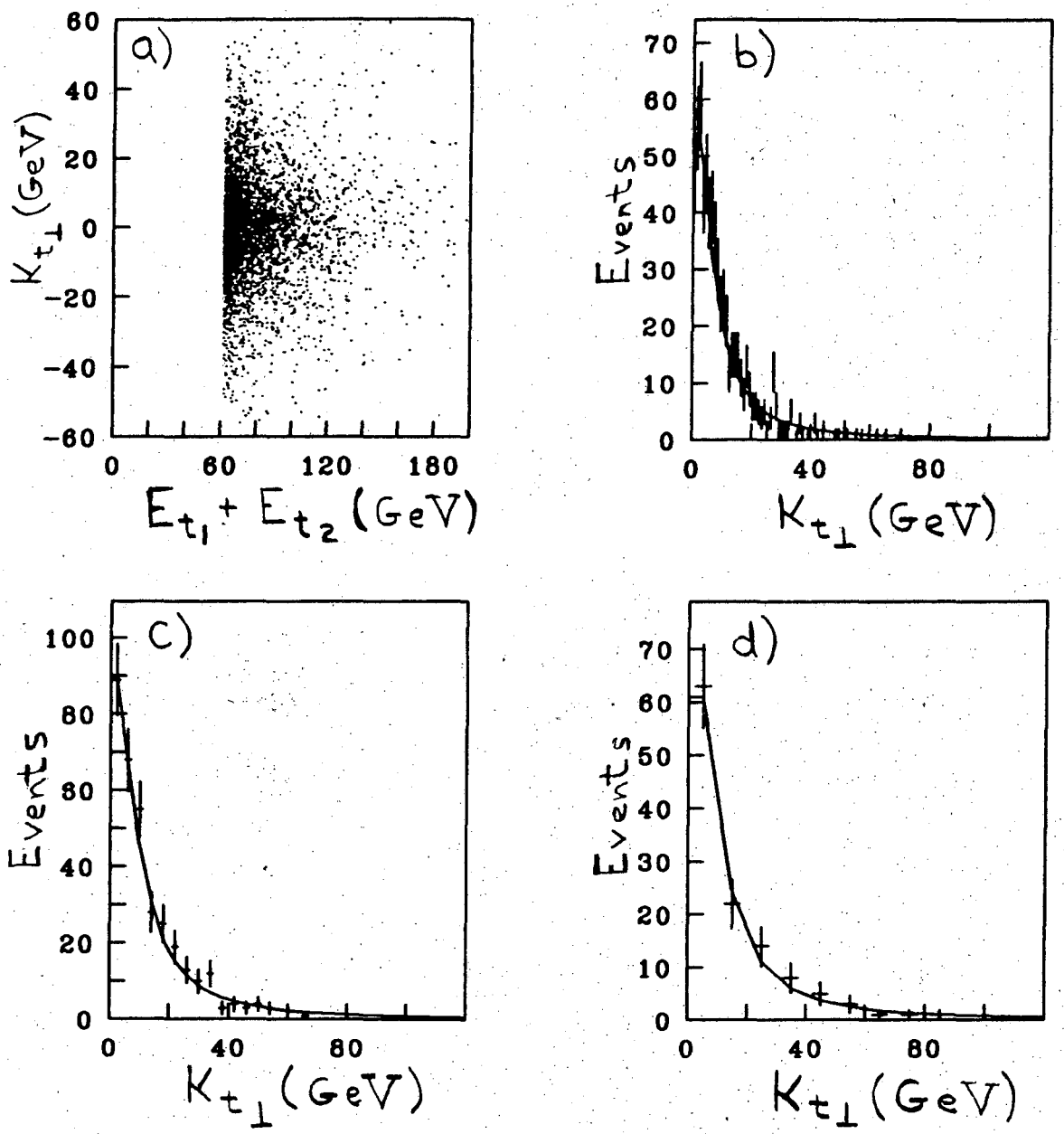

Figure 5.5: $K_{t_\perp}$ distributions. **a)** A scatter plot of $K_{t_\perp}$ versus the sum of the two leading jets E_t. **b)** $K_{t_\perp}$ distribution for $80 < E_{t1} + E_{t2} < 90$ GeV fit to a Lorentzian with Full Width at Half Maximum $\Gamma = 15$ GeV. **c)** $K_{t_\perp}$ distribution for $100 < E_{t1} + E_{t2} < 120$ GeV fit to a Lorentzian with FWHM $\Gamma = 19$ GeV. **d)** $K_{t_\perp}$ distribution for $140 < E_{t1} + E_{t2} < 200$ GeV fit to a Lorentzian with FWHM $\Gamma = 21$ GeV.

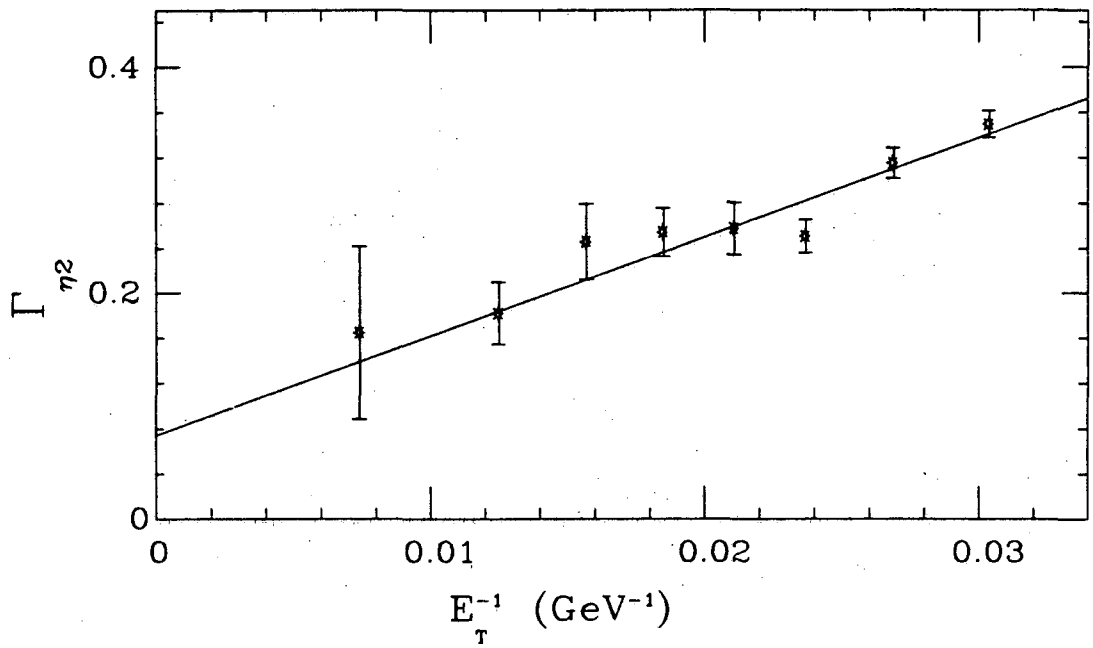

Figure 5.6: An estimate of the Lorentzian η_2 resolution of the two jet system, dominated by the effects of QCD radiation, is plotted as a function of $1/E_t$. The straight line is the estimate of the η_2 resolution function used in this analysis.

to be better than 2° ($\Delta\eta \approx .03$). The η_2 resolution appears to be dominated by effects other than calorimeter resolution. Since the angular resolution improves dramatically when we remove events with energetic third clusters[70], it is natural to conclude that the η_2 resolution is strongly affected by QCD radiation. The η_2 resolution is approximately the same as the width of the ϕ_{12} distribution (see figure 4.13a). The two distributions are directly related via the $K_{t_\perp}$ resolution and equation 5.3 using the small angle approximation. Our result, although obtained exclusively in the central calorimeters, was used for the η_2 resolution of all jets.

The largest uncertainty in the η_2 resolution function is caused by the assumption that the $K_{t_\perp}$ kick can be attributed statistically to both jets (see Appendix A.3, equation A.8), resulting in the factor of $\sqrt{2}$ in the denominator of equation (5.5). The upper systematic bound on the η_2 resolution has been estimated by simply attributing the entire $K_{t_\perp}$ kick to the second jet, thus multiplying both equation (5.5) and equation (5.12) by a factor of $\sqrt{2}$. If instead of adding the $K_{t_\perp}$ kick in

quadrature, we had added it linearly, the $\sqrt{2}$ in the dominator would have been a 2. To bracket any systematic uncertainty, the lower systematic bound was estimated by dividing both equation (5.5) and equation (5.12) by a factor of $\sqrt{2}$. In section 6.1.3 we will show that these generous systematic bounds lead to only small systematic uncertainties in the final cross section.

Our chosen systematic bounds gave η_2 resolution functions with maximum slope above the "standard", and minimum slope below the "standard". As in the case of the E_t resolution, we give an estimate of an η_2 resolution skew to the "standard" with maximum slope, and an η_2 resolution skew to the "standard" with minimum slope. The maximum η_2 resolution function is

$$\Gamma_{\eta_2}(E_t) = \frac{12}{E_t} + 0.11 \tag{5.13}$$

The minimum η_2 resolution function is

$$\Gamma_{\eta_2}(E_t) = \frac{6}{E_t} + 0.055 \tag{5.14}$$

The skew η_2 resolution function with maximum slope is

$$\Gamma_{\eta_2}(E_t) = \frac{12}{E_t} + 0.025 \tag{5.15}$$

The skew η_2 resolution function with minimum slope is

$$\Gamma_{\eta_2}(E_t) = \frac{6}{E_t} + 0.14 \tag{5.16}$$

These resolution functions bracket all the systematic uncertainties in the η_2 resolution.

5.2 E_t and η_2 Resolution Unsmearing

E_t and η_2 resolution distorts the produced two jet differential cross section. We call this distortion *resolution smearing*. In this section we describe how the resolution smearing was estimated, and the raw two jet differential cross section was corrected, in a procedure which we call *resolution unsmearing*.

5.2.1 Produced Distribution and Smearing Feeddown

The number of jets measured to be in a bin of E_t and $|\eta_2|$, is not the same as in the produced $2 \rightarrow 2$ distribution of jets. The finite resolution of the calorimeters, and QCD radiation and higher order processes, cause fluctuations in the measured E_t and η_2 of the two jet system. The steeply falling E_t spectrum, which becomes increasingly steeper with increasing $|\eta_2|$, combined with these fluctuations to produce a *feeddown* effect in which lower energy jets fluctuated down the steeply falling spectrum and were found in higher E_t bins. This feeddown increased with increasing $|\eta_2|$. The jets in the produced $2 \rightarrow 2$ distribution fluctuated into both higher and lower E_t bins, however the steeply falling spectrum resulted in many more jets fluctuating from low E_t into high E_t bins, than there were jets at high E_t which fluctuated into low E_t bins. Thus, the net effect of resolution smearing was a feeddown. Each bin in the raw two jet differential cross section contained more jets than were originally produced, the total extra number of jets originated from smaller E_t than our lowest bin. The measured distribution is different in shape and magnitude from the original produced $2 \rightarrow 2$ distribution.

We have *unsmeared* the measured distribution and found the produced $2 \rightarrow 2$ distribution. We started with a parameterized $2 \rightarrow 2$ distribution function, smeared it in E_t and η_2 with known resolution functions, and then varied the parameters of the parameterization until the smeared distribution matched the measured distribution. In this way the best values of the parameters for the parameterization of the produced $2 \rightarrow 2$ distribution were determined. The ratio of the parameterized $2 \rightarrow 2$ distribution to the smeared distribution was used as a multiplicative correction to the raw two jet differential cross section to scale it back to the original produced two jet differential cross section.

The modified Single Effective Subprocess approximation, described in section 2.3.2, was chosen as the parameterization of the produced $2 \rightarrow 2$ distribution. The modified SES approximation is a reasonable approximation of lowest order QCD, as shown in appendix A.1. Equation (2.28) with a parameterization for $F(x)$

was smeared with the measured resolution functions, and fit to the measured distribution. The best fit gave the most likely values of the parameters of $F(x)$. Our result for the proton effective structure function is compatible with DIS structure functions [10,11,12,13] evolved to CDF's higher Q^2 (see section 6.2). The good fit (see section 6.1.1) and the reasonable result for $F(x)$ indicate that the modified SES approximation is a reasonable approximation. Thus, the final results of our analysis supports our approximation of the produced $2 \rightarrow 2$ distribution.

5.2.2 Details of Unsmearing Method

To fit the smeared parameterization to the data, we used the maximum likelihood method [71]. To reduce computing time a "bin by bin" log likelihood method was used. The method is to calculate the likelihood function L, for the resolution smeared theoretical prediction, with parameterized structure function, for the data sample, and then vary the parameters of the structure function until the function $(-\ln L)$ is minimized. Define the likelihood function for N bins in which bin i contains n_i events of mean transverse energy $\overline{E}_{t,i}$ and mean probe jet pseudorapidity $\overline{\eta}_{2,i}$ by

$$L = \prod_{i=1}^{N} [P_i(\overline{E}_{t,i}, \overline{\eta}_{2,i})]^{n_i} \tag{5.17}$$

where P_i is the normalized probability of getting an event in bin i in our data sample. Write P_i in terms of a normalized probability density ρ^{norm} as

$$P_i(\overline{E}_{t,i}, \overline{\eta}_{2,i}) = \rho^{norm}(\overline{E}_{t,i}, \overline{\eta}_{2,i})(\Delta E_t \Delta \eta_2)_i \tag{5.18}$$

where $(\Delta E_t \Delta \eta_2)_i$ is just the area of bin i. The normalized probability density is nothing more than the total probablilty density for an event to occur normalized to one within the limits of this analysis:

$$\rho^{norm}(E_t, \eta_2) = \frac{\rho^{smeared}(E_t, \eta_2)}{\int_{E_t'} \int_{\eta_2'} \rho^{smeared}(E_t', \eta_2') dE_t' d\eta_2'}. \tag{5.19}$$

The total probability density is denoted by $\rho^{smeared}$, because the total probability density is the produced probability density smeared with the E_t and η_2 resolution

functions:

$$\rho^{smeared}(E_t,\eta_2) = \int_{E_t'}\int_{\eta_2'} \rho(E_t',\eta_2') R_{E_t}(E_t,E_t') R_{\eta_2}(\eta_2,\eta_2') dE_t' d\eta_2'. \qquad (5.20)$$

The E_t resolution used is Gaussian with E_t dependent width $\sigma(E_t)$ (see section 5.1.1):

$$R_{E_t}(E_t,E_t') = \frac{\exp\left[\frac{-(E_t'-E_t)^2}{2\sigma(E_t')^2}\right]}{\sqrt{2\pi}\,\sigma(E_t')}. \qquad (5.21)$$

The η_2 resolution used is a truncated Lorentzian with E_t dependent Full Width at Half Maximum $\Gamma(E_t)$ (see section 5.1.2):

$$R_{\eta_2}(\eta_2,\eta_2') = \frac{1}{2\arctan\left[\frac{4}{\Gamma(E_t')}\right]} \frac{\Gamma(E_t')/2}{(\eta_2-\eta_2')^2 + [\frac{\Gamma(E_t')}{2}]^2}. \qquad (5.22)$$

The produced probability density for the $2 \rightarrow 2$ scattering of partons is just the two jet rate in the modified Single Effective Subprocess approximation of equation (2.28), namely

$$\begin{aligned} \rho(E_t,\eta_2) &= \frac{d^3\sigma}{dE_t d\eta_1 d\eta_2}\Delta\eta_1 Lum_i \\ &= \frac{9\pi\alpha_s^2}{\hat{s}^2} F(x_A)F(x_B)E_t J(\chi)\Delta\eta_1 Lum_i \end{aligned} \qquad (5.23)$$

where Lum_i is the luminosity for bin i, and $\Delta\eta_1$ is the pseudorapidity range of the trigger jet ($\Delta\eta_1 = 1.2$). Equations (5.17) to (5.20), and (5.23) are written as functions of E_t and η_2 alone, since there is only one η_1 bin. We've done this analysis both by integrating over η_1 in equation (5.20), and by setting $\eta_1 = 0$, with less than 2% difference in any of the final results. We used the expression for $\alpha_s(Q^2)$ in appendix A.2 with $Q^2 = {E_t}^2$. The systematic uncertainty in the value of Q^2, important for the extraction of F, was estimated by varying the value of Q^2 between $4{E_t}^2$ and ${E_t}^2/4$ as discussed in appendix A.2.

The parameterization of the proton effective structure function was chosen to be

$$F(x) = \frac{A(1-x)^{P_1}}{x^{P_2}}. \qquad (5.24)$$

This is a conventional choice[13] for a simple parameterization of structure functions. It goes to zero at $x = 1$ and it models the expected low x behavior of the gluon distribution. The parameters P_1 and P_2 were determined by maximizing the likelihood distribution. Once the parameters P_1 and P_2 were found, the amplitude A was found by normalizing the smeared theoretical prediction to the data:

$$\sum_{i=1}^{N} n_i = \int_{E_t} \int_{\eta_2} \rho^{smeared}(E_t, \eta_2) dE_t d\eta_2. \tag{5.25}$$

After the parameters of the produced $2 \rightarrow 2$ distribution were found, the correction factor for scaling the raw two jet differential cross section back to the produced two jet differential cross section was calculated. Define C_i, the multiplicative correction factor for bin i, as the ratio of the produced $2 \rightarrow 2$ distribution in bin i to the total number of events expected in bin i after resolution smearing. Then

$$C_i = \frac{\rho(\overline{E}_{t,i}, \overline{\eta}_{2,i})}{\rho^{smeared}(\overline{E}_{t,i}, \overline{\eta}_{2,i})}. \tag{5.26}$$

The raw two jet differential cross section before correction is

$$\frac{d^3\sigma_i^{\ measured}}{dE_t d\eta_1 d\eta_2} = \frac{n_i}{Lum_i(\Delta E_t \Delta\eta_2)_i \Delta\eta_1} \tag{5.27}$$

and the corrected two jet differential cross section is

$$\frac{d^3\sigma_i^{\ corrected}}{dE_t d\eta_1 d\eta_2} = C_i \frac{d^3\sigma_i^{\ measured}}{dE_t d\eta_1 d\eta_2}. \tag{5.28}$$

In summary, the unsmearing serves two functions. First, it produces corrections for the raw two jet differential cross section, which scale the measured cross section back to the produced $2 \rightarrow 2$ cross section. Second, it extracts from the data the most likely values of the parameters in the chosen parameterization of the proton effective structure function. The proton effective structure function is related to the gluon, quark and antiquark structure functions in equation (2.5).

5.2.3 Statistical Issues

For a bin with n_i measured events the statistical error on the contents of the bin is $\sqrt{n_i}$. Once the correction constant C_i has been applied to the contents of

the bin, the statistical error on the corrected contents of the bin scales to $C_i\sqrt{n_i}$. This statistical uncertainty is given in Table 6.2.

At values of $|\eta_2|$ higher than 2.8, over 80% of the events are from smearing feeddown. These events contain little or no information on the corrected cross section. Thus events with $|\eta_2| > 2.8$ are dropped from the final plots and tables of this analysis. However, the events with $|\eta_2| > 2.8$ contain information on the shape and magnitude of the smearing feeddown. So three bins with $|\eta_2| > 2.8$ were retained to help the accurate determination of the smearing feeddown correction. These three bins are not listed in any of the tables but are displayed as the three points at highest $|\eta_2|$ of figure 6.1, and also contribute to the residuals distribution in figure 6.2. A few bins with higher $|\eta_2|$ contained fewer than 10 events each, and for convenience in calculating statistics were dropped. Those bins contained only smearing feeddown, but did not have enough statistics to contribute significantly to the measurement of the smearing feeddown, and hence were completely useless.

Chapter 6

Results

6.1 Two Jet Differential Cross Section

6.1.1 Raw Cross Section and Fit

As outlined in section 5.2, a parameterization of the produced $2 \rightarrow 2$ cross section was smeared with the measured E_t and η_2 resolution and fit to the raw cross section. The raw two jet differential cross section and smeared fit are shown together in figure 6.1. There were thirty-three degrees of freedom in the maximum likelihood fit and the chi-square per degree of freedom (χ^2/DOF) was 1.2. The χ^2/DOF was not minimized in the fit, instead the likelihood function was maximized, so the χ^2/DOF is only given as an indicator of the "goodness" of the maximum likelihood fit. The values of the fit are plotted at the discrete $|\eta_2|$ locations of the data and joined with straight lines. The distribution of the residuals, shown in figure 6.2, has a mean of zero and an RMS deviation of one; this indicates a good fit.

The fit, a successful completion of the smearing procedure, indicates that our parameterization is an acceptable estimate of the produced $2 \rightarrow 2$ distribution. The parameters of the effective structure function, extracted in the fit, are presented and discussed in section 6.2. These parameters, combined with the modified SES approximation discussed in section 2.3.2, parameterize the produced two jet differential cross section.

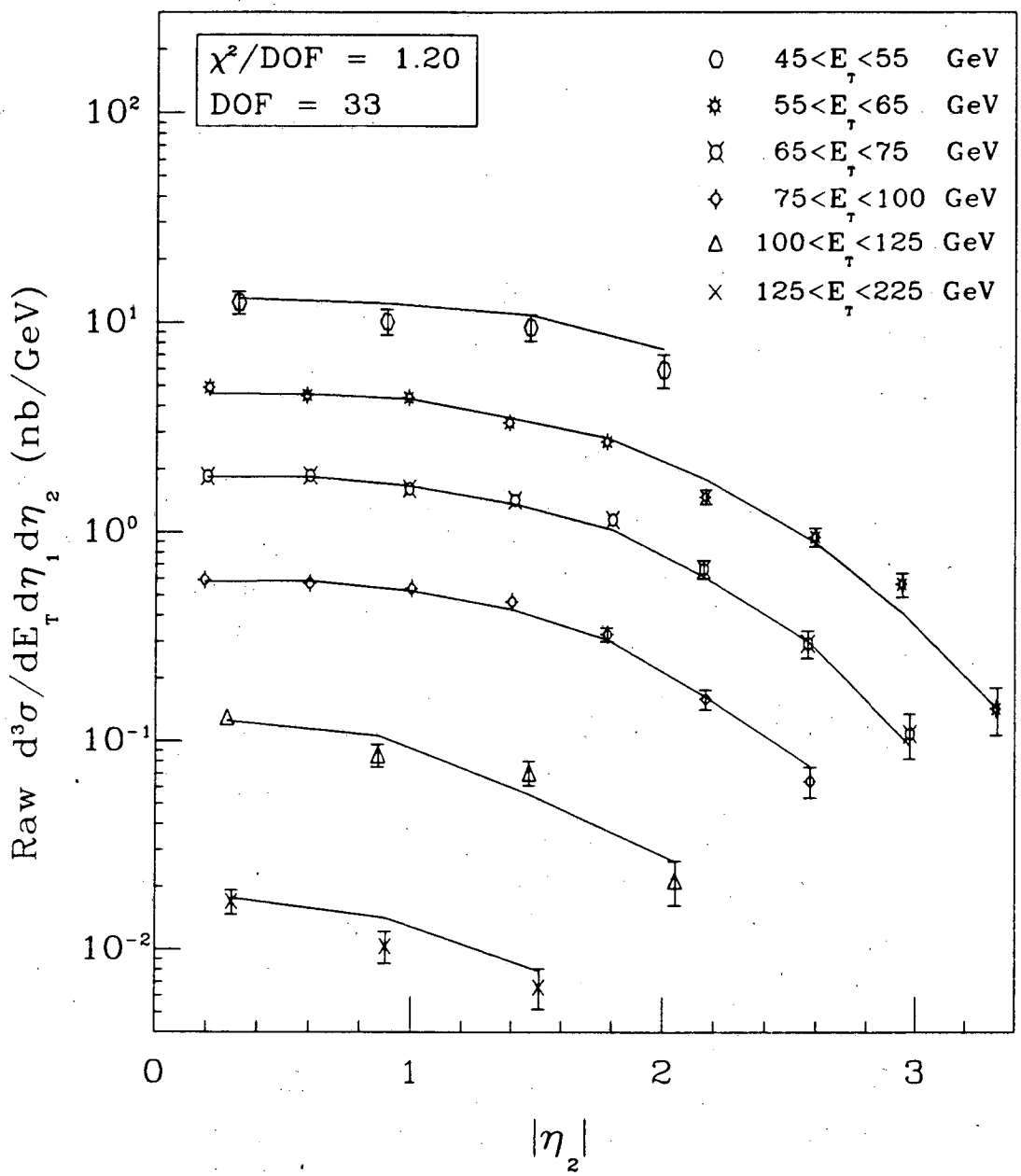

Figure 6.1: The raw two jet differential cross section (points) and a resolution smeared fit (line). The modified SES approximation, in which we parameterized the effective structure function, was smeared with E_t and η_2 resolution functions to produce the fit.

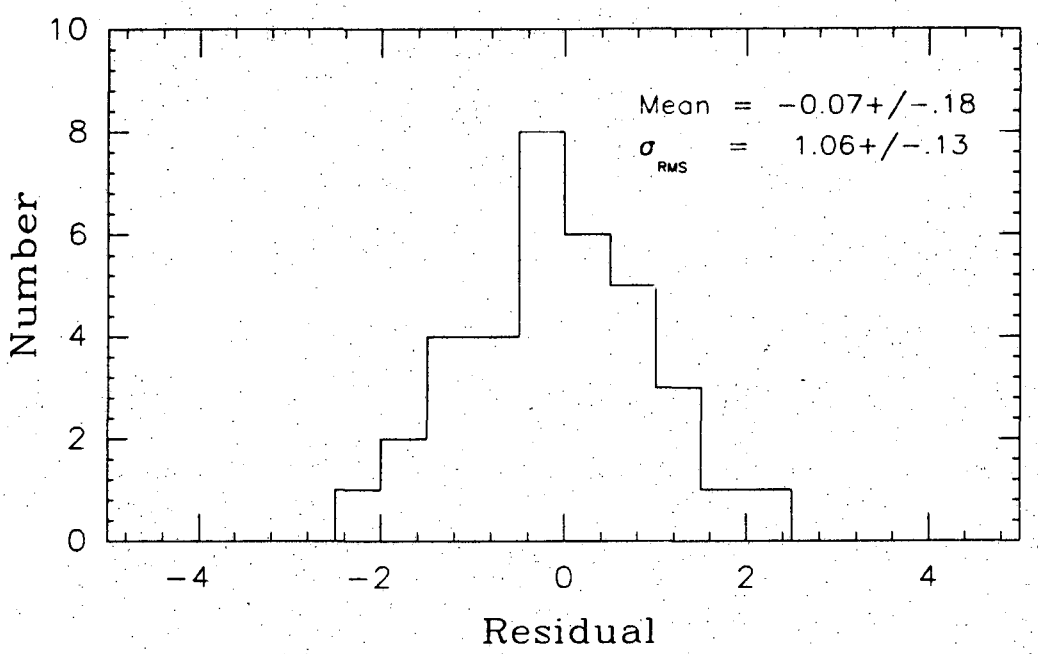

Figure 6.2: The distribution of residuals between the raw two jet differential cross section and the smeared fit. The residuals, defined as the difference between the data and the fit divided by the square root of the fit, are distributed statistically, indicating a good fit.

6.1.2 Two Jet Differential Cross Section

Resolution Smearing Corrections

Resolution smearing corrections are multiplicative correction factors which were applied to the raw cross section to obtain the corrected two jet differential cross section. The smearing corrections, defined in equation (5.26), are shown in figure 6.3 and listed in table 6.1, along with a summary of the raw number of jets and the luminosity. The smearing correction is equal to the average fraction of trigger jets in a bin of E_t and $|\eta_2|$ which physically originated in that bin before resolution smearing. This multiplicative correction was always less than one because there were always more jets at lower E_t feeding down the steeply falling spectrum into a given E_t bin than fluctuated out of the given E_t bin into other bins. At low $|\eta_2|$, the multiplicative correction factor decreased with decreasing E_t. This is

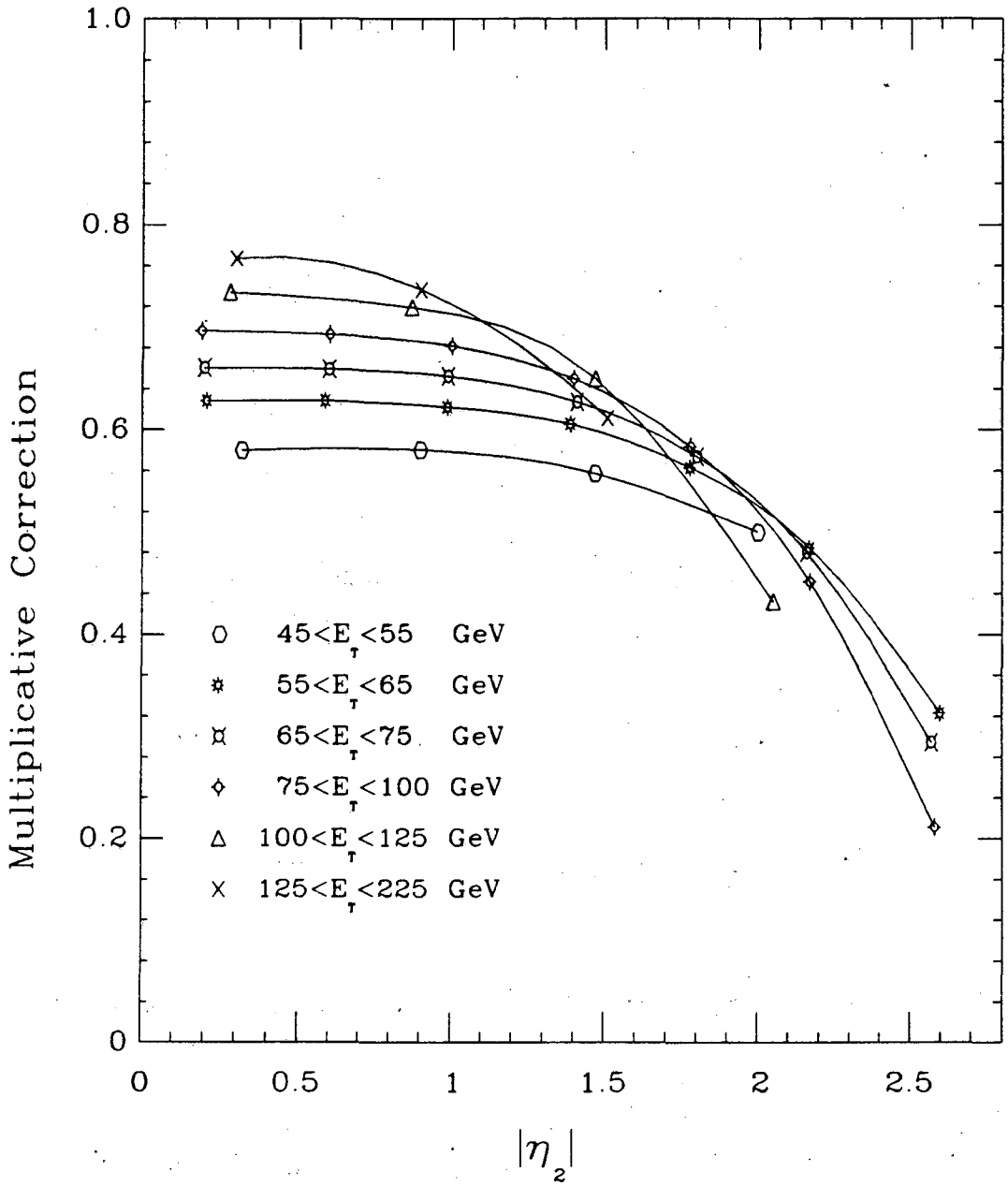

Figure 6.3: Multiplicative corrections to the raw two jet differential cross section for the effects of E_t and η_2 resolution smearing. The corrections, determined using jet data sample, are the average fraction of trigger jets which originated in a bin of E_t and $|\eta_2|$ before resolution smearing.

Bin #	E_t Range (GeV)	$\|\eta_2\|$ Range	Jets	$\int L$ (nb^{-1})	Smearing Correction
1	45– 55	0.0–0.6	63	0.35	0.580
2	45– 55	0.6–1.2	51	0.35	0.580
3	45– 55	1.2–1.8	48	0.35	0.557
4	45– 55	1.8–2.4	30	0.35	0.500
5	55– 65	0.0–0.4	512	10.88	0.628
6	55– 65	0.4–0.8	469	10.88	0.628
7	55– 65	0.8–1.2	457	10.88	0.622
8	55– 65	1.2–1.6	347	10.88	0.605
9	55– 65	1.6–2.0	282	10.88	0.563
10	55– 65	2.0–2.4	154	10.88	0.484
11	55– 65	2.4–2.8	99	10.88	0.323
12	65– 75	0.0–0.4	289	16.30	0.660
13	65– 75	0.4–0.8	291	16.30	0.659
14	65– 75	0.8–1.2	252	16.30	0.652
15	65– 75	1.2–1.6	222	16.30	0.627
16	65– 75	1.6–2.0	179	16.30	0.574
17	65– 75	2.0–2.4	104	16.30	0.480
18	65– 75	2.4–2.8	46	16.30	0.294
19	75–100	0.0–0.4	313	22.06	0.696
20	75–100	0.4–0.8	302	22.06	0.693
21	75–100	0.8–1.2	284	22.06	0.681
22	75–100	1.2–1.6	246	22.06	0.650
23	75–100	1.6–2.0	172	22.06	0.583
24	75–100	2.0–2.4	83	22.06	0.451
25	75–100	2.4–2.8	33	22.06	0.211
26	100–125	0.0–0.6	103	22.06	0.734
27	100–125	0.6–1.2	68	22.06	0.719
28	100–125	1.2–1.8	56	22.06	0.650
29	100–125	1.8–2.4	17	22.06	0.432
30	125–225	0.0–0.6	54	22.06	0.767
31	125–225	0.6–1.2	33	22.06	0.736
32	125–225	1.2–1.8	21	22.06	0.611

Table 6.1: The bin ranges, number of trigger jets per bin, integrated luminosity, and smearing corrections. The trigger jet was restricted to $|\eta_1| < 0.6$. The smearing correction is the fraction of observed jets which were actually produced in the given range of E_t and η_2 before resolution smearing.

because the E_t spectrum became steeper and the fractional E_t resolution became worse with decreasing E_t. Thus the lower E_t bins had a larger smearing feeddown and needed correspondingly smaller multiplicative correction factors. At higher $|\eta_2|$ the E_t spectrum is steeper and the effects of smearing are greater. Thus the multiplicative correction factor decreased with increasing $|\eta_2|$. In figure 6.3 the correction is plotted at the bin locations for this analysis, and corrections within the same E_t band are joined with a smooth curve to display the way the correction changes with E_t and $|\eta_2|$.

Corrected Two Jet Differential Cross Section

A summary of the corrected two jet differential cross section with statistical and total systematic uncertainties is given in table 6.2. The results are plotted in figure 6.4. Outer error bars are the sum of statistical and systematic uncertainties in quadrature; this does not include E_t and $|\eta_2|$ independent systematic uncertainties, common to all points, shown as the "normalization uncertainty" in figure 6.4. The total uncertainty for any cross section value is the sum of its outer error bar and the normalization uncertainty in quadrature. The upper "normalization uncertainty" is 41% and the lower "normalization uncertainty" is 30%, which is the total systematic uncertainty on the cross section value for bin 30. Also plotted is a $2 \rightarrow 2$ analytic QCD calculation, including all lowest order diagrams, for one particular structure function (EHLQ[10] set 2) and three values of Q^2: the upper curves in each band are for $Q^2 = {E_t}^2/4$, the middle curves are for $Q^2 = {E_t}^2$, and the lower curves are for $Q^2 = 4{E_t}^2$. We performed the QCD calculation using equation (2.22).

The corrected two jet differential cross section and the lowest order QCD prediction agree within theoretical and experimental systematic uncertainties. The theoretical systematic uncertainty on the QCD calculation, illustrated by the width of the band, is smaller than the experimental systematic uncertainty. The agreement demonstrates that the corrected two jet differential cross section for the inclusive process $\bar{p}p \rightarrow$ jet1 + jet2 + X, can be approximately understood as a convolution of structure functions and $2 \rightarrow 2$ lowest order QCD subprocess cross sections. The

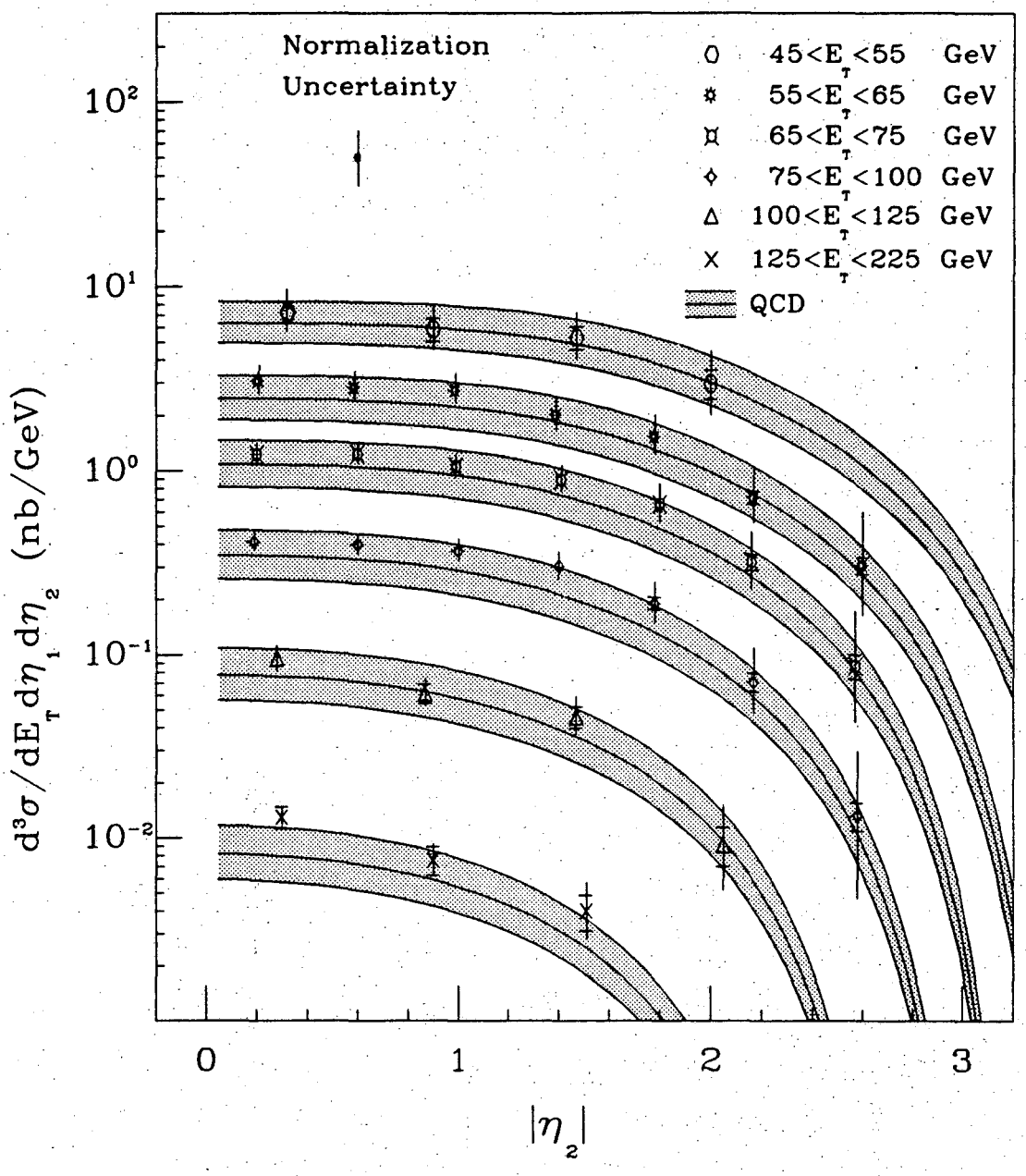

Figure 6.4: The measured and corrected two jet differential cross section (points) compared to a lowest order QCD prediction (shaded). Outer error bars include E_t and $|\eta_2|$ dependent systematic uncertainties and statistical uncertainties (inner error bars). An E_t and $|\eta_2|$ independent systematic uncertainty, common to all points, is shown as the overall normalization uncertainty. The QCD prediction uses EHLQ set 2 structure functions, and was calculated for three different values of Q^2: the upper curves in each band are for $Q^2 = {E_t}^2/4$, the middle curves are for $Q^2 = {E_t}^2$, and the lower curves are for $Q^2 = 4{E_t}^2$.

Bin #	$\overline{E_t}$ (GeV)	$\overline{\lvert\eta_2\rvert}$	$d^3\sigma/dE_t d\eta_1 d\eta_2$ (nb/GeV)	Stat. Err. (%)	↑ Sys. Err. (%)	↓ Sys. Err. (%)
1	49.6	0.32	7.24	± 13	+ 52	− 36
2	49.7	0.90	5.86	± 14	+ 52	− 36
3	49.2	1.47	5.30	± 14	+ 53	− 36
4	49.3	2.00	2.97	± 18	+ 62	− 41
5	59.4	0.21	3.08	± 4	+ 45	− 33
6	59.3	0.59	2.82	± 5	+ 46	− 33
7	59.1	0.99	2.72	± 5	+ 46	− 33
8	59.7	1.39	2.01	± 5	+ 47	− 34
9	59.2	1.78	1.52	± 6	+ 51	− 36
10	59.5	2.17	0.714	± 8	+ 61	− 39
11	59.2	2.60	0.306	± 10	+ 103	− 55
12	69.6	0.20	1.22	± 6	+ 42	− 31
13	69.2	0.60	1.23	± 6	+ 42	− 31
14	69.4	0.99	1.05	± 6	+ 43	− 32
15	69.6	1.41	0.889	± 7	+ 44	− 32
16	69.1	1.80	0.656	± 7	+ 49	− 35
17	69.4	2.16	0.319	± 10	+ 60	− 40
18	68.7	2.57	0.0866	± 15	+ 106	− 57
19	84.6	0.19	0.411	± 6	+ 42	− 31
20	84.0	0.60	0.395	± 6	+ 43	− 32
21	84.1	1.00	0.365	± 6	+ 43	− 32
22	83.8	1.40	0.302	± 6	+ 44	− 32
23	83.0	1.78	0.189	± 8	+ 50	− 36
24	83.2	2.17	0.0707	± 11	+ 65	− 43
25	81.0	2.58	0.0132	± 17	+ 132	− 69
26	109.2	0.28	0.0952	± 10	+ 42	− 32
27	109.6	0.87	0.0616	± 12	+ 43	− 32
28	112.5	1.47	0.0458	± 13	+ 47	− 34
29	108.2	2.05	0.00925	± 24	+ 70	− 48
30	149.1	0.30	0.0130	± 14	+ 41	− 30
31	148.4	0.90	0.00765	± 17	+ 42	− 31
32	145.6	1.51	0.00404	± 22	+ 53	− 37

Table 6.2: Two jet differential cross section results and uncertainties.

two jet differential cross section exhibits a slight rapidity plateau at low $|\eta_2|$ and then decreases with increasing $|\eta_2|$, as expected from the decrease of the structure functions with parton fractional momentum x.

6.1.3 Systematic Uncertainties

The total systematic uncertainty on the two jet differential cross section is dominated by the systematic uncertainty on the jet E_t measurement and correction. The total systematic uncertainty was displayed on the cross section plot in figure 6.4 and listed in table 6.2. The total upper systematic bound on the cross section varied from 41% for the lowest $|\eta_2|$ bin of the highest E_t bin to 132% for the highest $|\eta_2|$ bin of the 75–100 GeV E_t bin. The total lower systematic bound on the cross section varied from -30% to -69%, and came from the same two bins as mentioned above. For a single E_t interval, the total systematic uncertainty broken down into all contributing systematic uncertainties is displayed in figure 6.5. This illustrates that the uncertainty on the jet E_t measurement and correction is the dominant systematic uncertainty. For each bin in the two jet differential cross section, a breakdown of the total systematic uncertainty is given for upper systematic bounds in table 6.3 and for lower systematic bounds in table 6.4. The individual systematic uncertainties are discussed in order of importance in this section

Jet E_t

The systematic uncertainty on the jet energy measurement and correction, discussed in section 4.4 and displayed in figure 4.2, are the work of reference [47]. The systematic uncertainty on $\sin\theta$ within the region $|\eta_1| < 0.6$ is negligible, so the jet energy uncertainty is the jet E_t uncertainty. The uncertainties were 8.5%, 7.6%, 7.0%, 6.8%, 6.6% and 6.1% for the six E_t bins with mean jet energies of 52, 62, 73, 88, 116, and 156 GeV respectively. To calculate the effect on the cross section of this systematic uncertainty in the energy scale, we used the slopes of the E_t spectrum of the trigger jet as a function of the pseudorapidity $|\eta_2|$ of the probe

jet. The E_t spectrum had different slopes as a function of $|\eta_2|$ as was shown in figure 4.11. The change in rate produced by a change in jet E_t was calculated from the measured slope of the E_t spectrum. For the sake of completeness the exact procedure is indicated below.

The E_t spectrum obeys the approximate power law

$$\frac{dN}{dE_t} = A\left(\frac{1}{E_t}\right)^p. \tag{6.1}$$

The expected number of events in a bin of E_t, with low edge $E_{t,min}$ and high edge $E_{t,max}$ was obtained by integrating equation (6.1):

$$N(E_t) = \frac{A}{p-1}\left(\frac{1}{{E_{t,min}}^{p-1}} - \frac{1}{{E_{t,max}}^{p-1}}\right). \tag{6.2}$$

If the energy of a jet is changed by a factor of $(1 \pm f_E)$, where f_E is the fractional uncertainty in the jet energy scale, the new transverse energy of the jet is

$$E_t' = (1 \pm f_E)E_t \tag{6.3}$$

and the ratio of the new number of trigger jets to the old number of trigger jets, R_N, is obtained by substituting equation (6.3) into equation (6.2) and dividing by the original number of events in the bin, giving

$$R_N = \frac{N(E_t')}{N(E_t)} = \frac{1}{(1 \pm f_E)^{(p-1)}}. \tag{6.4}$$

The E_t spectrum was steeper at higher values of $|\eta_2|$ because of the natural decrease of the structure functions with $|\eta_2|$. This was illustrated in figure 4.11 and discussed in section 4.8.2. The value of p as a function of $|\eta_2|$ was found by fitting the E_t spectrum of the trigger jet for different bins of $|\eta_2|$. The resulting power as a function of $|\eta_2|$ was fit to a smooth curve. The explicit powers used for the narrow $|\eta_2|$ bins ($\Delta|\eta_2| = 0.4$) were

$$p = \begin{cases} 6.0 & if \quad |\eta_2| < 1.6 \\ 6.2 & if \quad 1.6 \leq |\eta_2| < 2.0 \\ 6.6 & if \quad 2.0 \leq |\eta_2| < 2.4 \\ 8.2 & if \quad 2.4 \leq |\eta_2| < 2.8 \\ 9.6 & if \quad 2.8 \leq |\eta_2| < 3.2 \end{cases} \tag{6.5}$$

The explicit powers used for the wide $|\eta_2|$ bins ($\Delta|\eta_2| = 0.6$) were

$$p = \begin{cases} 6.0 & if \quad |\eta_2| < 1.8 \\ 6.5 & if \quad 1.8 \leq |\eta_2| < 2.4 \\ 8.5 & if \quad 2.4 \leq |\eta_2| < 3.0 \end{cases} \tag{6.6}$$

Using these powers as a function of $|\eta_2|$, and f_E for each E_t interval, R_N was calculated for each bin of E_t and $|\eta_2|$. The raw cross section in each bin was then multiplied by R_N. Then the complete unsmearing analysis discussed in section 5.2 was repeated, and new results were found. This was done for both the upper and lower systematic bounds on the energy scale, producing lower and upper bounds respectively on the cross section. This also gave lower and upper bounds for the effective structure function.

This procedure produced slightly different systematic uncertainty estimates than just multiplying the factors R_N directly into the final cross section result. This is because the multiplicative smearing correction factors derived from the unsmearing analysis changed by up to 10% when the number of events was scaled by R_N. The net effect was to reduce the cross section uncertainty at low $|\eta_2|$ and increase it at high $|\eta_2|$. For example, applying equation (6.4) to bin 1, $f_E = 0.085$ and $p = 6.0$ gives $R_N = 1.56$, but the actual uncertainty due to the energy scale listed in Table 6.3 is +48% (or 1.48). The systematic uncertainties, calculated by changing the rate and performing the unsmearing analysis again, are more valid than just applying the factor of R_N directly to the final cross section result. The uncertainty analysis was performed using the former method, which simultaneously estimates systematic uncertainties in the effective structure function.

The systematic uncertainty in the total cross section due to systematic uncertainty in the jet energy are listed in tables 6.3 and 6.4 in the column labeled "E_t", and displayed graphically for a single E_t interval in figure 6.5 using the symbol labeled "E_t". The upper systematic bound on the total cross section due to systematic uncertainty in the jet energy scale varied from 37% for the lowest $|\eta_2|$ bin of the highest E_t bin (bin # 30), to 124% for the highest $|\eta_2|$ bin of the 75-100 Gev E_t bin (bin # 25). The corresponding lower systematic bound varied from

-25% to -52%, and came from the same two bins as mentioned above. Inspection of equation (6.4) reveals why the lower systematic bounds are closer to the mean result than the upper systematic bounds.

Luminosity

The systematic uncertainty on the luminosity for each hardware trigger threshold was discussed in section 4.1 and listed in table 4.1. The systematic uncertainty on the cross section from the luminosity measurement is 17% for the lowest E_t interval and 15% for the remaining E_t intervals.

E_t Resolution

The maximum likelihood unsmearing analysis, outlined in section 5.2, was performed with the "standard" E_t resolution of equation (5.6) and the four different worst case resolutions all given in section 5.1.1. For each bin, the upper bound systematic uncertainty due to resolution was calculated from the maximum value for that bin among the four worst case results, and the lower bound systematic uncertainty was calculated from the minimum value for that bin. The systematic uncertainty in the cross section was about 10% for low $|\eta_2|$, rising to about 25% at the highest $|\eta_2|$, which is a small uncertainty compared to the systematic uncertainty in the cross section caused by the systematic uncertainty in the jet E_t.

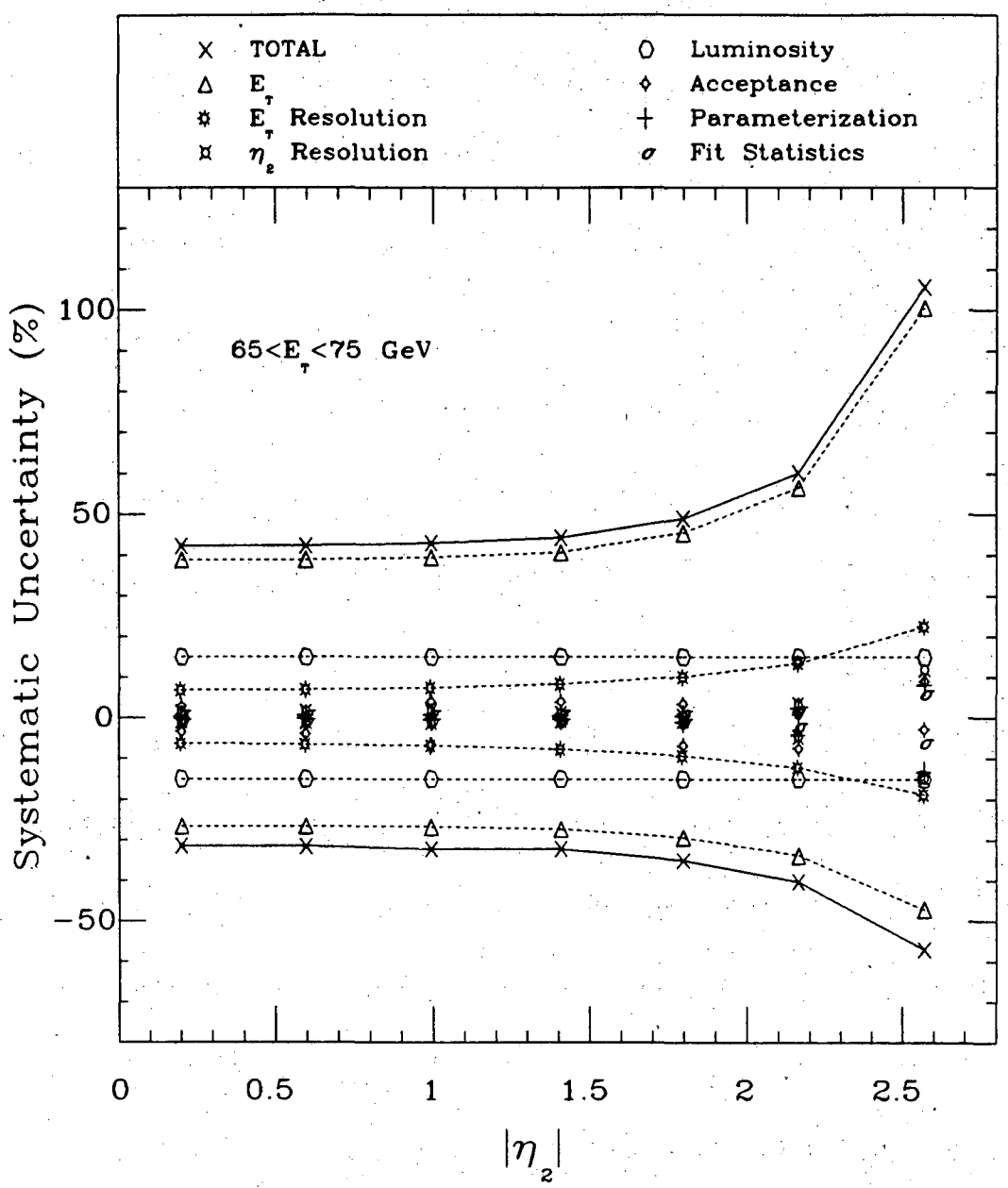

Figure 6.5: The systematic uncertainties on the two jet differential cross section are shown for a single E_t interval. For each $|\eta_2|$ value the independent sources of systematic uncertainty are shown and the total systematic uncertainty, from adding the individual uncertainties in quadrature, is also shown. Important systematic uncertainties are joined by dotted lines, and the total systematic uncertainty is joined by a solid line, to illustrate the way the uncertainty grows with $|\eta_2|$.

Bin #	E_t (%)	Lum (%)	E_t Res (%)	η_2 Res (%)	Acc (%)	Param (%)	Fit (%)	Total (%)
1	48	17	8	2	2	1	2	52
2	48	17	8	2	0	2	2	52
3	49	17	9	2	1	2	2	53
4	59	17	11	0	1	1	2	62
5	42	15	7	2	4	1	2	45
6	42	15	7	2	1	1	2	46
7	43	15	8	2	2	2	2	46
8	44	15	8	2	1	2	2	47
9	48	15	10	0	2	1	2	51
10	58	15	12	2	5	2	2	61
11	99	15	20	9	4	6	5	103
12	39	15	7	1	3	0	1	42
13	39	15	7	2	0	1	1	42
14	39	15	7	2	4	1	1	43
15	41	15	8	1	4	0	1	44
16	45	15	10	0	3	1	1	49
17	56	15	13	3	1	2	2	60
18	100	15	22	12	9	8	6	106
19	39	15	6	1	3	0	1	42
20	39	15	7	1	3	0	1	43
21	39	15	7	1	2	0	1	43
22	41	15	8	0	3	0	1	44
23	47	15	10	1	2	1	2	50
24	61	15	15	6	7	4	3	65
25	124	15	30	19	0	13	10	132
26	39	15	6	1	7	0	1	42
27	39	15	7	1	7	0	1	43
28	44	15	9	1	6	1	1	47
29	66	15	18	8	6	6	5	70
30	37	15	6	1	2	1	1	41
31	38	15	7	0	7	1	1	42
32	46	15	12	3	17	3	2	53

Table 6.3: Sources of the upper systematic bound on the two jet differential cross section. These independent systematic uncertainties, described in the text, were added in quadrature to form the total upper systematic uncertainty listed.

Bin #	E_t (%)	Lum (%)	E_t Res (%)	η_2 Res (%)	Acc (%)	Param (%)	Fit (%)	Total (%)
1	−31	−17	− 7	− 1	− 1	0	− 2	−36
2	−31	−17	− 7	− 2	− 3	− 1	− 2	−36
3	−31	−17	− 8	− 1	0	− 1	− 2	−36
4	−35	−17	−10	0	− 9	0	− 2	−41
5	−28	−15	− 7	− 1	− 4	− 1	− 2	−33
6	−28	−15	− 7	− 1	− 4	− 1	− 2	−33
7	−28	−15	− 7	− 1	− 4	− 1	− 2	−33
8	−29	−15	− 8	− 1	− 5	− 1	− 2	−34
9	−31	−15	− 9	0	− 5	− 1	− 2	−36
10	−34	−15	−11	− 3	0	− 3	− 2	−39
11	−47	−15	−17	−11	− 1	−10	− 5	−55
12	−27	−15	− 6	− 1	− 3	0	− 1	−31
13	−27	−15	− 6	− 1	− 4	0	− 1	−31
14	−27	−15	− 7	− 1	− 7	0	− 1	−32
15	−27	−15	− 8	− 1	0	0	− 1	−32
16	−29	−15	− 9	− 1	− 7	− 1	− 1	−35
17	−34	−15	−12	− 5	− 7	− 4	− 2	−40
18	−47	−15	−19	−15	− 3	−13	− 6	−57
19	−26	−15	− 6	− 1	− 3	0	− 1	−31
20	−27	−15	− 6	− 1	− 5	0	− 1	−32
21	−27	−15	− 7	− 1	− 4	0	− 1	−32
22	−27	−15	− 8	0	− 6	0	− 1	−32
23	−30	−15	−10	− 2	− 7	− 2	− 2	−36
24	−36	−15	−14	− 8	0	− 7	− 6	−43
25	−52	−15	−24	−23	−13	−21	−10	−69
26	−26	−15	− 6	− 1	− 9	− 1	− 1	−32
27	−27	−15	− 7	0	− 3	0	− 1	−32
28	−29	−15	− 9	− 1	− 1	− 2	− 1	−34
29	−38	−15	−16	−11	−11	−10	− 5	−48
30	−25	−15	− 6	0	− 2	− 1	− 1	−30
31	−26	−15	− 7	0	− 3	− 1	− 1	−31
32	−30	−15	−11	− 5	− 9	− 5	− 2	−37

Table 6.4: Sources of the lower systematic bound on the two jet differential cross section. These independent systematic uncertainties, described in the text, were added in quadrature to form the total lower systematic uncertainty listed.

η_2 Resolution

The maximum likelihood unsmearing analysis, outlined in section 5.2, was performed with the "standard" η_2 resolution function of equation (5.12) and the four different worst case resolution functions given in section 5.1.2. For each bin, the upper bound systematic uncertainty due to resolution was calculated from the maximum value for that bin among the four worst case results, and the lower bound systematic uncertainty was calculated from the minimum value for that bin. The systematic uncertainty in the cross section was about 2% for low $|\eta_2|$, rising to about 15% at the highest $|\eta_2|$, which is a small uncertainty compared to the systematic uncertainty in the cross section due to the systematic uncertainty in the jet E_t.

Acceptance

The corrections made for the E_t response of the 90° crack and the η_1 dependent E_t response of the medium threshold sample were discussed in section 4.7.2. These corrections have a small affect on the acceptance of the sample. The systematic limits on the crack correction were applied to the data to measure the resulting systematic uncertainty on the cross section. The resulting systematic uncertainty in the cross section is small, varying from about 2% at low $|\eta_2|$ to as much as 15% at high $|\eta_2|$. The cross section was calculated with and without the medium threshold response correction, and the difference was taken to be the systematic uncertainty in the cross section. The systematic uncertainty was small, varying from about 1% at small $|\eta_2|$ to as much as 10% at large $|\eta_2|$. The systematic uncertainties in the cross section from the crack correction and the medium threshold response correction were combined in quadrature, and the resulting systematic uncertainty is listed in table 6.3 and 6.4 in the column labelled "Acc".

Parameterization

The systematic uncertainty in the choice of parameterization for the produced $2 \rightarrow 2$ distribution was bounded by the original SES approximation angular

distribution and the gluon-gluon angular distribution as discussed in appendix A.1. The unsmearing analysis of section 5.2 was performed with the "standard" effective angular distribution, and repeated using the two systematic bounds. The difference in the smearing correction was small; the systematic uncertainty in the corrected cross section varied between about 1% at low $|\eta_2|$ to about 10% at the highest $|\eta_2|$.

Fit

The statistical uncertainty in the maximum likelihood fit was obtained from the 1 σ contour. This systematic uncertainty in the cross section varied from around 1% for the low $|\eta_2|$ bins to about 7% for the highest $|\eta_2|$ bins.

6.1.4 Chi-Square Comparison

The two jet differential cross section can be compared with theoretical expectations in a more quantitative fashion by calculating a chi-square. Following the lead of reference [72] we divide the error on the cross section into three errors: an uncorrelated statistical error, an uncorrelated systematic error, and a correlated systematic error. The value of the chi-square is highly dependent on how much of the systematic uncertainty is correlated from bin to bin. For any particular complete correlation the shape of the two jet differential cross section would be highly constrained, and the chi-square between theory and experiment would be maximal. If all the systematic uncertainties were completely uncorrelated from bin to bin, then the shape of the two jet differential cross section would be much less constrained, and the chi-square between theory and experiment would be minimal. To avoid excluding structure function theories which may be valid, we tried to avoid overestimating the fraction of the systematic uncertainty which was correlated, and hence took a conservative approach.

Uncorrelated systematic uncertainties allow for maximal skewing of the shape of the two jet differential cross section, while correlated systematic uncertainties define rigidly how the shape can be altered. Systematic uncertainties which

are observed to raise one part of the two jet cross section, while lowering another part, have large potential for changing the shape of the two jet differential cross section. Since the inflection point between the region which is raised and the region which is lowered is not that well known, such skewing systematic uncertainties have the potential to produce a large ensemble of possible different shapes for the final cross section. This ensemble is bounded by the magnitude of the systematic uncertainty, but the shape of possible results within the bounds vary considerably. It is a conservative approach to take such skewing systematic uncertainties as completely uncorrelated from bin to bin, then the bin contents are allowed to fluctuate at random within the bounds of the skewing systematic uncertainty, and few possible shapes within these bounds are excluded.

As in the case of the single jet inclusive cross section [72], the systematic uncertainty in the cross section caused by the systematic uncertainty in the jet E_t and the luminosity is completely correlated from bin to bin: it raises all the bins together or lowers them all together. The systematic uncertainties in the cross section caused by the the systematic uncertainty in the acceptance and choice of parameterization is also highly correlated from bin to bin. The systematic uncertainties that have the potential to raise one part of the differential cross section while lowering another are the systematic uncertainties on the resolution functions.

The systematic bounds on the E_t resolution function, given in equation (5.9) and equation (5.10), slightly skew the final corrected two jet differential cross section. The systematic bounds on the η_2 resolution functions, given in equation (5.13) and (5.14), also slightly skew the final corrected two jet cross section though less than the E_t resolution bounds do. The effects of these four resolution functions are used to estimate an uncorrelated component of the systematic uncertainty in the cross section. In addition the statistical error on the fit contributes to the uncorrelated component of the the systematic uncertainty. These uncertainties were combined in quadrature to obtain an estimate of the total uncorrelated systematic uncertainty. For $|\eta_2| < 2.0$ the uncorrelated systematic uncertainty ranged from 2% to 5%, while for the highest $|\eta_2|$ bins the uncorrelated systematic uncertainty

Theory	$Q^2 = 4E_t^2$	$Q^2 = E_t^2$	$Q^2 = \frac{E_t^2}{4}$
DO 1	0.7	0.8	1.3
DO 2	1.6	0.7	1.2
EHLQ 1	0.7	0.8	1.2
EHLQ 2	0.8	0.9	1.3
DFLM 1	0.8	0.8	1.0
DFLM 2	0.8	0.9	1.1
DFLM 3	0.9	1.0	1.5
MRS 1	0.8	0.7	0.9
MRS 2	0.7	1.2	2.8
MRS 3	1.0	1.1	1.6
MRS B	0.9	0.8	1.0
MRS E	0.8	0.7	0.9

Table 6.5: Chi-square per degree of freedom between QCD theories and CDF data (32 degrees of freedom). The theoretical prediction was calculated using lowest order QCD, with the structure function and Q^2 scale given in the table.

was in the range 10% to 25%. These systematic uncertainties are a small fraction of the total systematic uncertainty, which is predominantly correlated from bin to bin because the E_t uncertainty is correlated from bin to bin. The correlated uncertainty squared was obtained by subtracting the uncorrelated systematic uncertainty squared from the total systematic uncertainty squared.

Once the correlated systematic uncertainty had been estimated, we followed the procedure outlined in reference [72], and calculated the full error matrix for the 32 bins in the two jet differential cross section. The error matrix is a square symmetric 32 × 32 matrix. A diagonal element of the error matrix, σ_{ii}^2, is the total uncertainty for bin i squared. An off-diagonal element of the error matrix, σ_{ij}^2, is the correlated systematic uncertainty for bin i times the correlated systematic uncertainty for bin j. The error matrix was inverted, and the residuals between QCD and the corrected two jet differential cross section were calculated. The inner product of the inverse error matrix and the residual vectors was calculated, resulting in a chi-square. The chi-square was calculated for twelve different possible structure

functions, using three different values of the Q^2 scale, and the χ^2/DOF are listed in table 6.5. In this table *theory* means an analytic $2 \rightarrow 2$ QCD calculation, using the given structure function, and the given value of the Q^2 scale. The strong coupling, α_s, was calculated using the expression in appendix A.2.

From inspection of this table we see that the two jet differential cross section is in good agreement with QCD for a wide range of structure functions and Q^2 scales. The only significant exception is for the structure function MRS[13] set 2 when $Q^2 = E_t^2/4$, which is excluded at over 99% confidence level. This exclusion is for a lowest order QCD calculation, α_s as defined in appendix A.2, and $Q^2 = E_t^2/4$; we note that MRS set 2 has more partons at $x > 0.1$ than the other structure function theories checked. Three combinations, DFLM set 3 for $Q^2 = E_t^2/4$, DO set 2 for $Q^2 = 4E_t^2$, and MRS set 3 for Q^2=$E_t^2/4$ had marginal χ^2 (47, 50, and 53 for 32 degrees of freedom). The remaining 32 combinations are in good agreement with our measurement. We see that the two jet differential cross section, after correction for resolution smearing, agrees with most QCD lowest order calculations using DIS structure functions.

6.2 Effective Structure Function of the Proton

The similarity of parton subprocess cross sections made it possible to extract an effective structure function of the proton

$$F(x) \approx G(x) + \frac{4}{9}(Q(x) + \overline{Q}(x)) \tag{6.7}$$

as discussed in section 2.3.2. In brief, the structure function was parameterized by

$$F(x) = \frac{A(1-x)^{P_1}}{x^{P_2}} \tag{6.8}$$

and used in the modified SES approximation to calculate the produced $2 \rightarrow 2$ cross section. The produced cross section was smeared with E_t and η_2 resolution functions and fit to the raw two jet differential cross section, as described in section 5.2.2. From the fit, shown in figure 6.1, we found the parameters of $F(x)$. The effective

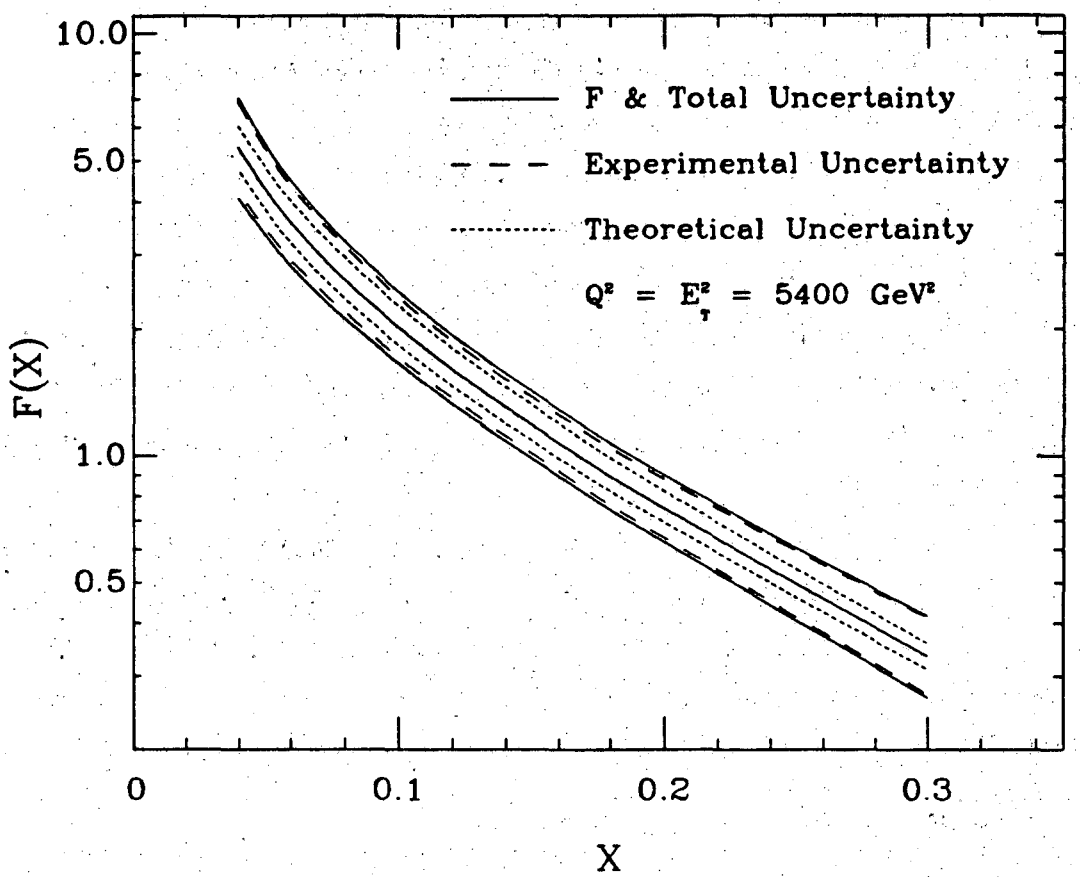

Figure 6.6: The proton effective structure function, $F(x) \approx G(x) + \frac{4}{9}(Q(x) + \overline{Q}(x))$, is shown as the central solid curve. Experimental, theoretical, and total uncertainties are also shown as curves bracketing the central solid curve. The mean value of Q^2 was 5400 GeV^2.

structure function is displayed and compared to DIS measurements in section 6.2.1. The parameter values, uncertainties, and correlations are given and discussed in section 6.2.2.

6.2.1 $F(x)$

Results

The proton effective structure function is displayed in figure 6.6 as the central solid curve. Theoretical and experimental uncertainties are displayed as dotted

and dashed curves. The total uncertainty, displayed as solid curves bracketing the result, was obtained by adding the experimental and theoretical uncertainties in quadrature. The uncertainties are bounds estimated at the 1 σ level.

The experimental uncertainty was calculated by adding the statistical uncertainty and the experimental systematic uncertainty in quadrature. The statistical uncertainty was the envelope of the 1 σ contour from the maximum likelihood fit. The experimental systematic uncertainty was estimated by varying each uncertain factor (jet E_t, resolutions, luminosities, ...) separately, repeating the unsmearing analysis, and extracting new values for the parameters of the structure function. Then, the envelopes of each systematic bound on $F(x)$, calculated using the parameters found, were added in quadrature. The experimental uncertainty was dominated by the systematic uncertainty on the jet energy scale. A theoretical uncertainty was estimated by varying the angular distribution, and by varying the Q^2 scale, as discussed in appendix A.1 and A.2. The theoretical systematic uncertainty is smaller than the experimental systematic uncertainty.

Comparison

The effective structure functions is compared to standard parameterizations for the proton effective structure function evolved from deep inelastic scattering (DIS) measurements in figure 6.7. The three structure functions shown in the figure are those of Duke and Owens[11] set 1 (abbreviated by DO 1), those of Eichten, Hinchliffe, Lane and Quigg [10] set 1 (abbreviated by EHLQ 1), and those of Diemoz, Ferroni, Longo, and Martinelli [12] set 1 (abbreviated by DFLM 1). The magnitude of our result (labeled CDF) agrees with the DIS structure functions within the systematic uncertainties. The CDF result at low x is slightly higher than the DIS predictions (20% to 10% between $x = .05$ and $x = .1$). However, this difference is within the systematic uncertainties on the measurement. This is the same information as was presented in figure 6.4, which showed that the two jet differential cross section was slightly higher than the QCD and DIS prediction for $Q^2 = {E_t}^2$.

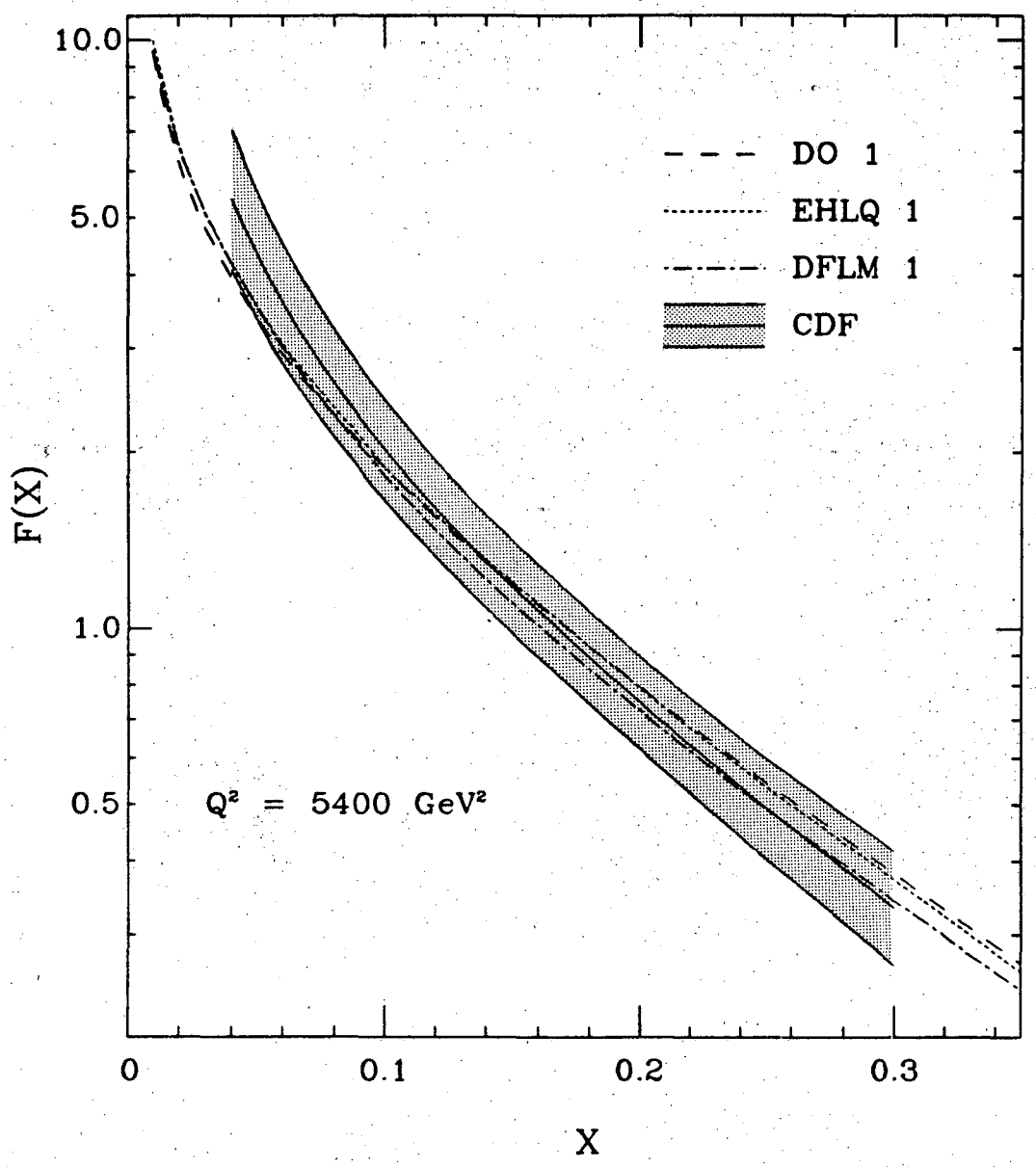

Figure 6.7: Our result for the proton effective structure function (band labeled CDF), is compared to predictions for $F(x) = G(x) + \frac{4}{9}(Q(x) + \overline{Q}(x))$ from QCD evolutions of deep inelastic scattering measurements.

Range of x

Our result is only shown in the x range $0.04 < x < 0.3$, because this is the range of x covered by the data with reasonable statistics. The $55 < E_t < 65$ GeV bin, which contains most of the data, corresponds to $x = 0.06$ when $|\eta_2| = 0.0$. The same E_t bin corresponds to a low x of $x_B = 0.038$, and a high x of $x_A = 0.28$, when $|\eta_2| = 2.0$ (see equation 2.12 and 2.13). That was the original motivation for the chosen x range. Looking at the low x end of our sample, there are around 500 partons between $x = 0.035$ and $x = 0.045$ and the number falls off sharply at lower x both because of the E_t cut and the increased smearing with η_2. Looking at the high x end, there are about 250 events between $x = 0.25$ and $x = 0.30$, with around 30 of those events between $x = 0.29$ and $x = 0.30$. Beyond the x range shown there are few partons and most of the data in a bin is from smearing feeddown, and so we conservatively show the structure function results only in the range $0.04 < x < 0.3$. Beyond that range the $F(x)$ results are not valid.

The measured effective structure function over the given range of x is insensitive to variations in $Q^2 = {E_t}^2$. The CDF result is for an average Q^2 of 5400 GeV^2. From low x to high x the Q^2 varied from about 4000 GeV^2 to about 7000 GeV^2 Over this range of Q^2 variation, very little variation in the structure function is expected. For example, the evolution in F (given by EHLQ set 1), between the average Q^2 over the entire data sample and the mean value of Q^2 for a single value of x in the data sample, varies between 0% at $x = 0.04$ to 2% at $x = 0.3$, which is small compared to other systematic effects.

6.2.2 Parameters of $F(x)$

The proton effective structure function parameter values, uncertainties, and correlations are given in table 6.6. The experimental uncertainties were estimated by varying each uncertain experimental variable (see section 6.1.3) and extracting new values for the parameters A, P_1, and P_2. Then all the experimental systematic uncertainties were added in quadrature. The systematic uncertainty

Param.	Value	Uncertainties			Correlations		
		Stat.	Systematic				
			Exp.	Theory	A	P_1	P_2
A	.45	$\pm.07$	$\pm.17$	$^{+.15}_{-.06}$	—	+1	−1
P_1	3.6	$\pm.25$	$\pm.9$	$^{+.6}_{-.3}$	+1	—	−1
P_2	.82	$\pm.05$	$\pm.17$	$^{+.03}_{-.07}$	−1	−1	—

Table 6.6: The parameter values, uncertainties, and approximate correlation coefficients for the proton effective structure function $F(x) = \frac{A(1-x)^{P_1}}{x^{P_2}}$.

on the jet E_t scale dominated the experimental systematic uncertainty on the parameters. The theoretical systematic uncertainties were estimated by changing the angular distribution of the modified SES approximation as discussed in appendix A.1, and by changing the Q^2 scale as discussed in appendix A.2, and adding the resulting uncertainties in quadrature. The correlation between P_1 and P_2 was estimated by MINUIT[73] to be -0.985. These results are only valid for $0.04 < x < 0.3$, as discussed in the previous section.

The parameter A is the amplitude of the effective structure function, the parameter P_1 is related to the slope at high x and the parameter P_2 is related to the slope at low x. The parameters are highly correlated, as indicated in table 6.6. The upper bound on A corresponds to the upper bound on P_1 and the lower bound on P_2. This correlation between A and the other parameters is a consequence of normalizing the total predicted number of events to the number of events in the data. However, the parameters P_1 and P_2 are extracted during the likelihood maximization procedure, which fits the smeared parameterization to the shape of the data. The parameters P_1 and P_2 are anti-correlated regardless of the normalization of the data, while A is correlated to P_1 and P_2 by normalizing the total predicted number of events to the number of events in the data.

6.3 Gluon Structure Function of the Proton

The inclusive jet cross section at $\sqrt{s} = 1.8$ TeV is predicted to be dominated by quark-gluon and gluon-gluon scattering[74]. Thus, it is expected that the two jet differential cross section is primarily the result of interactions containing gluons in the initial state. This provided us with a natural laboratory for measuring the gluon structure function of the proton. Unfortunately, we are unable to distinguish quarks from gluons and identify a specific subprocess. We can, however, estimate the gluon structure function of the proton, within the framework of lowest order QCD and the parton model, if we assume values for the quark and anti-quark structure functions.

The gluon structure function of the proton was parameterized in the same way as equation(5.24), namely

$$G(x) = \frac{A_G(1-x)^{P_{1G}}}{x^{P_{2G}}}. \tag{6.9}$$

With this parameterization of $G(x)$, and using EHLQ[10] set 1 for the quark and antiquark structure functions, we have calculated the lowest order QCD prediction for the two jet differential cross section and fit it to our measured and corrected two jet differential cross section. The fit had a χ^2/DOF of 1.25 for 30 degrees of freedom. Once again the parameters P_{1G} and P_{2G} were varied in the fit, and the parameter A_G came from the normalization of our result, though this time the fit was achieved by minimizing the chi-square.

The gluon structure function is displayed in figure 6.8 as the central solid curve. The total uncertainties are displayed as solid curves bracketing the central solid curve. Theoretical and experimental uncertainties are displayed as dotted and dashed curves respectively. The uncertainties are estimates of 1 σ uncertainties. This estimate of the gluon structure function of the proton is shown in comparison to DIS predictions in figure 6.9.

The CDF result and the DIS predictions agree within the systematic uncertainties on the CDF measurement. Since EHLQ set 1 was used for the quark and

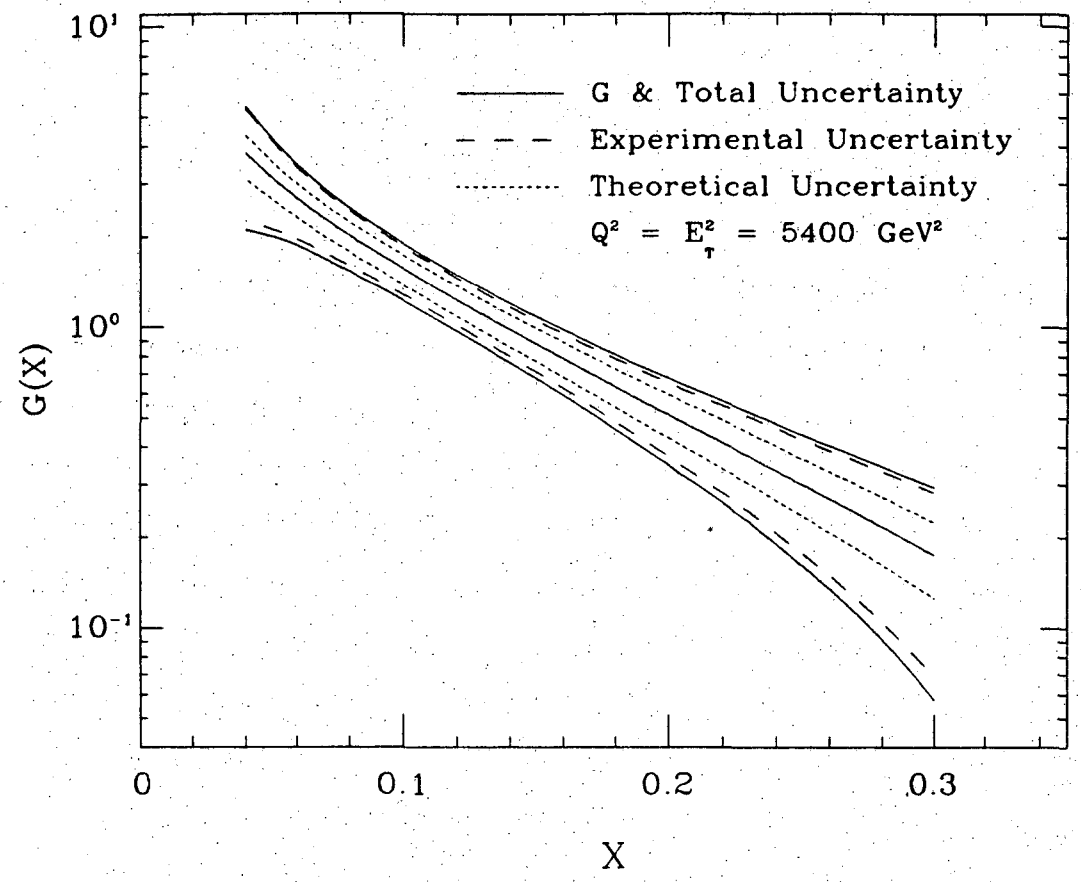

Figure 6.8: The gluon structure function of the proton is shown as the central solid curve. Experimental, theoretical, and total uncertainties are also shown as curves bracketing the central solid curve.

anti-quark structure functions we take particular note of the comparison between our estimate of $G(x)$ and that of EHLQ set 1. Our estimate of $G(x)$ has a nearly identical shape to that of EHLQ set 1, but has slightly higher magnitude (around 15% higher at $x = 0.05$). The slightly higher magnitude is the same information as the small excess in cross section above the QCD prediction (using $Q^2 = E_t{}^2$) in figure 6.4. This slightly higher magnitude for $G(x)$ is also the same information as the excess in $F(x)$ above the DIS predictions at small x in figure 6.6, within the systematic uncertainties on the two extraction methods.

As for the proton effective structure function, the gluon structure function over the given range of x is insensitive to variations in Q^2 present in the measure-

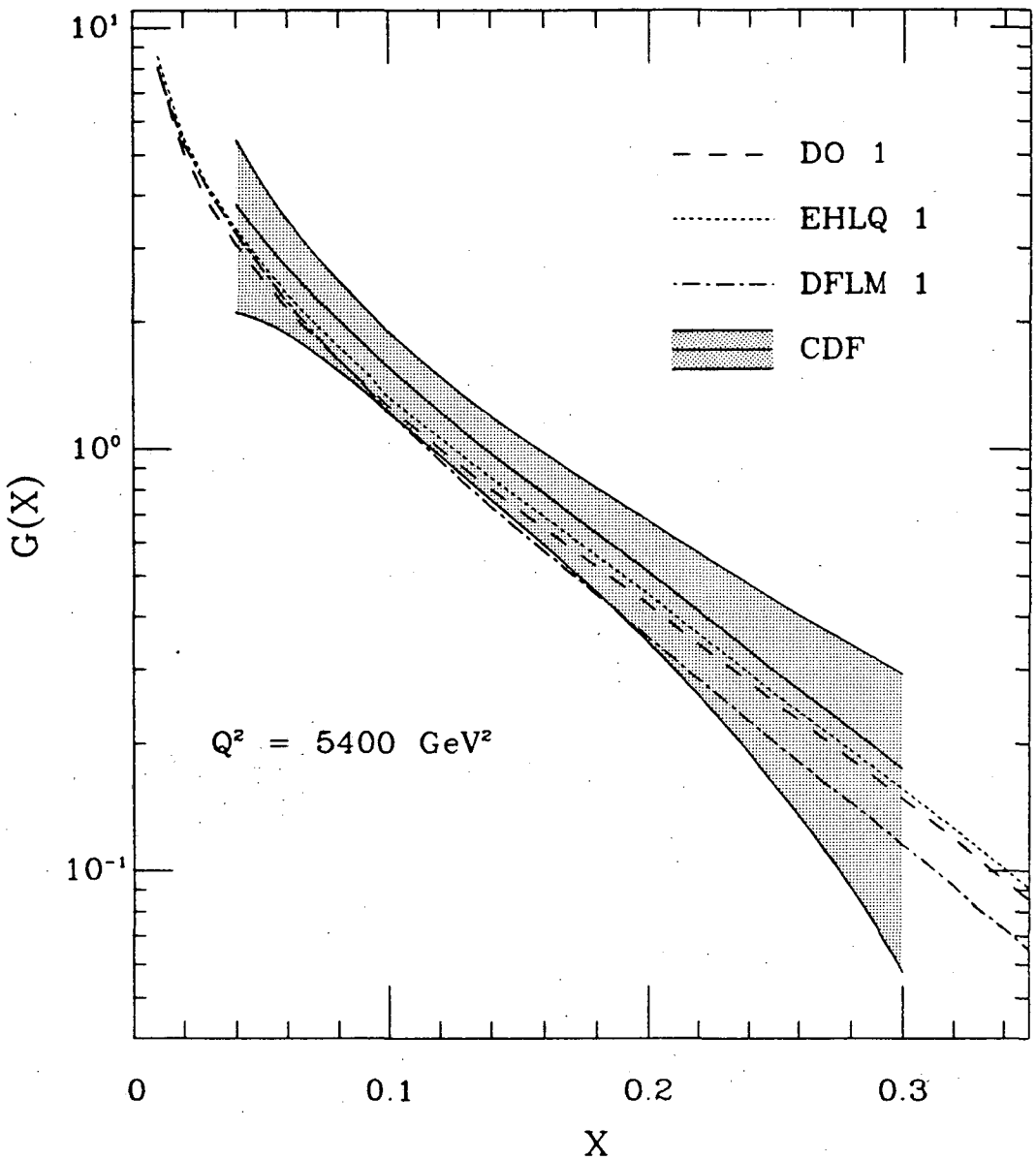

Figure 6.9: An estimate of the gluon structure function (band labeled CDF) compared to predictions from QCD evolutions of deep inelastic scattering measurements.

Param.	Value	Uncertainties			Correlations		
		Stat.	Systematic				
			Exp.	Theory	A	P_1	P_2
A_G	.96	$\pm.06$	$+8$ $-.66$	$+.9$ $-.36$	—	$+1$	-1
P_{1G}	6.5	$\pm.2$	$+6$ -3.1	$+2.0$ -1.2	$+1$	—	-1
P_{2G}	.51	$\pm.04$	$+0.42$ -0.8	$+.14$ $-.25$	-1	-1	—

Table 6.7: The parameter values, uncertainties, and approximate correlation coefficients for the gluon structure function of the proton $G(x) = \frac{A_G(1-x)^{P_{1G}}}{x^{P_{2G}}}$.

ment. From low x to high x the Q^2 varied from about 4000 GeV^2 to about 7000 GeV^2, which corresponds to a predicted variation between 0% at $x = 0.04$ to 4% at $x = 0.3$. This is a small variation compared to other systematic effects.

The values found for the parameters, uncertainties, and correlations are given in table 6.7. The experimental uncertainties were estimated by changing each uncertain experimental variable and extracting new values for the parameters A_G, P_{1G}, and P_{2G}. Then all of the experimental systematic uncertainties were added in quadrature. The systematic uncertainty on the jet E_t scale dominates the total experimental systematic uncertainty on the parameters. The theoretical systematic uncertainties were estimated by varying the quark and antiquark structure functions between two other structure functions which use the same value of Λ as EHLQ 1 (DO 1 and MRS B), and by changing the Q^2 scale between ${E_t}^2/4$ and $4{E_t}^2$, and adding the resulting uncertainties in quadrature. These results are only valid for $0.04 < x < 0.3$, as discussed in the previous section.

As with the effective structure function parameterization, the systematic uncertainties on A_G and P_{1G} are highly correlated, and the systematic uncertainties on P_{1G} and P_{2G} are highly anti-correlated. The lower bound on the gluon structure function corresponds to the upper bound on A_G, the upper bound on P_{1G}, and the lower bound on P_{2G}. The upper bound on the gluon structure function corresponds

to the lower bound on A_G, the lower bound on P_{1G}, and the upper bound on P_{2G}. It is important to pay attention to these correlations when interpreting the uncertainties on the parameters given in table 6.7.

The systematic uncertainties on the parameters A_G, P_{1G}, and P_{2G} are much larger than the systematic uncertainties on the parameters A, P_1 and P_2. This is because, when evaluating the uncertainties on the gluon structure function, we are fixing the quark and anti-quark structure functions and putting all the uncertainty in the cross section into an uncertainty in the gluon structure function. Since the parameters are highly correlated, the parameter values can change a lot, though the integral of the gluon structure function from $x = 0.04$ to $x = 0.3$ doesn't change as much. The integral of the gluon structure function is

$$\int_{.04}^{.3} G(x)dx = .27 \pm .01 \pm .07 \pm .04 \tag{6.10}$$

where the first error is the statistical uncertainty, the second is the experimental systematic uncertainty, and the third is the theoretical systematic uncertainty. Adding the three errors in quadrature we confirm the existence of gluons to 3.3 standard deviations. Our mean result predicts that 27% of the momentum of the proton comes from gluons with fractional momentum between $x = 0.04$ and $x = 0.3$.

6.4 Conclusions

Data from the 1987 run of the Collider Detector at Fermilab has been used to measure the two jet differential cross section $d^3\sigma/dE_t d\eta_1 d\eta_2$ in proton anti-proton collisions at $\sqrt{s} = 1.8$ TeV. In this measurement, one jet was in the central region ($|\eta_1| < 0.6$), where η_1 and η_2 are the pseudorapidity of the two jets with largest transverse energy in the event, and E_t is the transverse energy of the centrally produced jet. Lowest order QCD and the similarity of subprocess angular distributions in the modified SES approximation have been used to extract from the data a parameterization of the proton effective structure function. Using lowest order QCD, and quark and anti-quark structure functions evolved from deep inelas-

tic scattering (DIS) measurements, the gluon structure function of the proton has been estimated from the measured two jet differential cross section. The two jet differential cross section, effective structure function, and gluon structure function are all in agreement with leading order QCD and DIS expectations.

We have compared the corrected two jet differential cross section with an analytic lowest order QCD calculation using twelve different structure function theories and three different values of the Q^2 scale. We can only exclude the single structure function MRS[13] set 2 when used with $Q^2 = {E_t}^2/4$ ($\chi^2 = 90$ for 32 degrees of freedom). Three combinations, DFLM[12] set 3 for $Q^2 = {E_t}^2/4$, DO[11] set 2 for $Q^2 = 4{E_t}^2$, and MRS[13] set 3 for $Q^2={E_t}^2/4$ had marginal χ^2 (47, 50, and 53 for 32 degrees of freedom). Each of the remaining thirty-two combinations are in good agreement with our measurement. We have used simple parameterizations for the effective structure function and the gluon structure function of the proton, and have extracted values for the parameters, listed in table 6.6 and table 6.7. The existence of gluons within the proton has been confirmed to 3.3 standard deviations.

In conclusion, high transverse energy jet production in $\bar{p}p$ collisions at $\sqrt{s} = 1.8$ TeV is well described by the parton model. In particular, lowest order QCD calculations using DIS structure functions are sufficient to describe the measured cross section.

Appendix A

Theoretical Details

A.1 Angular Distributions

In the original SES approximation[20] the effective angular distribution was the t-channel gluon exchange term:

$$J_t(\chi) = \chi^2 + \chi + 1 + \chi^{-1} + \chi^{-2} \tag{A.1}$$

where $\chi = \hat{u}/\hat{t} = e^{\eta_1 - \eta_2}$. This angular distribution, predicted for quark scattering with different flavors ($q_i q_j \rightarrow q_i q_j$), is the largest term in five out of eight subprocess angular distributions (see table 2.2). However, at $\sqrt{s} = 1.8$ TeV the two subprocesses $qg \rightarrow qg$ and $gg \rightarrow gg$ dominate the overall $\bar{p}p \rightarrow$ jet + X cross section for $P_t < 200$ GeV [74], and a better choice for the effective angular distribution is the $qg \rightarrow qg$ angular distribution

$$J(\chi) = J_t(\chi) + \frac{2}{9}(\chi + 3 + \chi^{-1}). \tag{A.2}$$

Equation (A.2) was used as the effective angular distribution in our modified SES approximation, presented in section 2.3.2. The $gg \rightarrow gg$ angular distribution

$$J_{gg}(\chi) = J_t(\chi) + 2 - \frac{\chi}{(\chi+1)^2} \tag{A.3}$$

served as a systematic upper bound and $J_t(\chi)$ served as a systematic lower bound on the effective angular distribution.

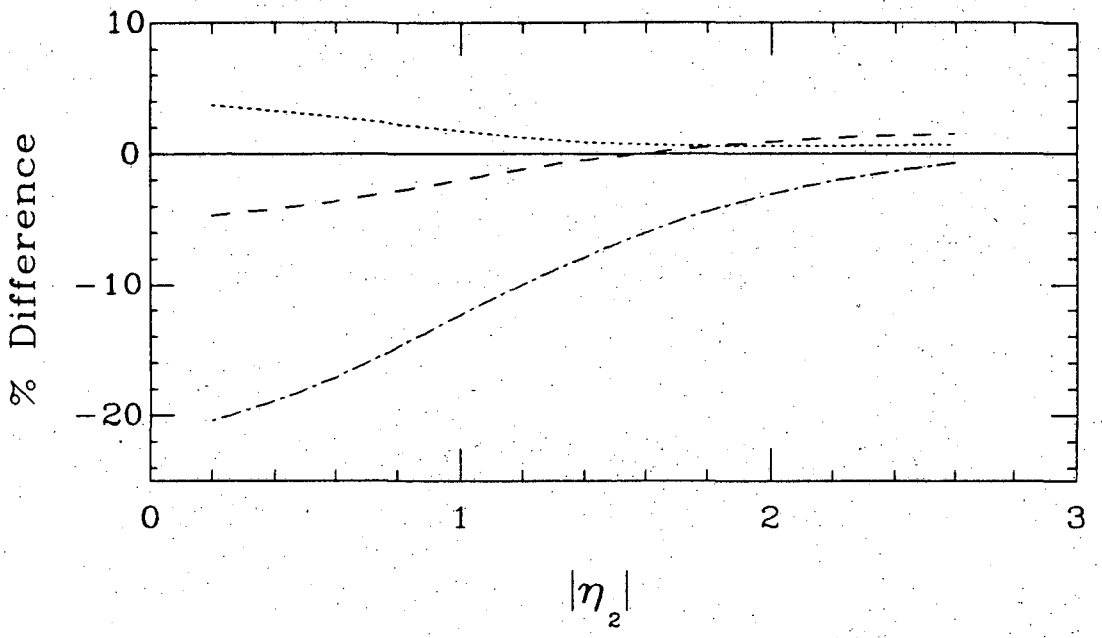

Figure A.1: The percent difference in two jet cross section between lowest order QCD and three SES approximations. The approximation using the $gg \rightarrow gg$ angular distribution (dots) is always slightly higher than QCD (solid), while the original SES approximation (dot-dashed) is lower than QCD. Our modified SES approximation (dashed), using the $qg \rightarrow qg$ angular distribution, approximates lowest order QCD. The calculation was for $75 \leq E_t \leq 100$ GeV and used EHLQ set 1 structure functions.

In figure A.1 we compare the differences in the two jet cross section, between three different SES approximations and lowest order QCD, as a function of probe jet pseudorapidity. Note that our modified SES approximation is within 5% of lowest order QCD, and is clearly a much better approximation than the original SES approximation. The calculation, done for a single E_t interval, used EHLQ set 1 structure functions and $Q^2 = E_t^2$. The comparison depends on the structure functions used, so it would be unwise to tune the effective angular distribution to match lowest order QCD precisely. At one extreme, if there were only gluons in the proton then the $gg \rightarrow gg$ distribution would be the natural choice. At the other extreme, if there were only quarks in the proton, then $J_t(\chi)$ would be a good choice. However, there are both quarks and gluons in the proton, and the $qg \rightarrow qg$ angular

distribution is a reasonable choice for the effective angular distribution, while $J_t(\chi)$ and the $gg \rightarrow gg$ angular distribution bracket our systematic uncertainty.

The mean result for the effective structure function, $F(x)$, came from using the $qg \rightarrow qg$ angular distribution of equation (A.2) for the unsmearing procedure outlined in section 5.2. $F(x)$ extracted using the $gg \rightarrow gg$ angular distribution was everywhere within -3% of our mean result, and $F(x)$ extracted using $J_t(\chi)$ was everywhere within $+8\%$ of our mean result. This difference was combined in quadrature with the difference arising from uncertainties in the Q^2 scale (See Appendix A.2) to form the total theoretical uncertainty on the effective structure function result.

A.2 α_s

The convention we have adopted for the calculation of the strong coupling constant is the one accepted by the Particle Data Group [15]. The strong coupling constant α_s is calculated with an analytic expression in terms of the QCD coupling parameter Λ. In this convention Λ increases as Q^2 crosses quark mass thresholds, thereby taking into account the increased number of quark flavors that can partake in internal quark loops. This convention is outlined in reference [15], and one of its authors (I. Hinchliffe) has provided us with the appropriate equations to transform Λ from $\Lambda^{(n-1)}$ to $\Lambda^{(n)}$ as Q^2 crosses the nth quark flavor threshold. Note that what we call Q^2 throughout this thesis, is called μ^2 by the authors of reference [15]. We take $\Lambda^{(4)} = \Lambda^{(4)}_{\overline{MS}} = 0.2$ [15] as the QCD coupling parameter with four quarks flavors. The uncertainty in the measured value of $\Lambda^{(4)}$ is not as significant as the uncertainty in the Q^2 scale mentioned below, and we neglect it. The equation for increasing Λ as we cross the bottom mass threshold is given by

$$\Lambda^{(5)} = \Lambda^{(4)}\left(\frac{\Lambda^{(4)}}{m_b}\right)^{\frac{2}{23}}\left[\ln\left(\left[\frac{m_b}{\Lambda^{(4)}}\right]^2\right)\right]^{\frac{-963}{13225}} \tag{A.4}$$

and the equation for increasing Λ as we pass the top mass threshold is given by

$$\Lambda^{(6)} = \Lambda^{(5)}\left(\frac{\Lambda^{(5)}}{m_t}\right)^{\frac{2}{21}}\left[\ln\left(\left[\frac{m_t}{\Lambda^{(5)}}\right]^2\right)\right]^{\frac{-321}{3381}} \tag{A.5}$$

where we take $m_b = 5.0$ GeV and $m_t = 50.0$ GeV. The final value of α_s would be only 2% less if we chose m_t as high as 200 GeV, and this difference is insignificant compared to the uncertainty in the Q^2 scale discussed below.

Since our jet E_t is always greater than m_b, the value of Λ we use in calculating α_s is given by

$$\Lambda = \begin{cases} \Lambda^{(5)} & if \quad Q^2 < {m_t}^2 \\ \Lambda^{(6)} & if \quad Q^2 > {m_t}^2 \end{cases} \tag{A.6}$$

where we take $Q^2 = {E_t}^2$. Then the value of α_s is given at next to lowest order by [15]

$$\alpha_s(Q^2) = \frac{12\pi}{(33-2n_f)\ln(Q^2/\Lambda^2)}\left[1 - \frac{6(153-19n_f)}{(33-2n_f)^2}\frac{\ln[\ln(Q^2/\Lambda^2)]}{ln(Q^2/\Lambda^2)}\right] + \ldots. \tag{A.7}$$

The value of α_s is very sensitive to our choice of Q^2. Once higher order corrections are calculated the theoretical prediction should be less sensitive to variations in the choice of Q^2 scale, as partial calculations indicate[75], but until then we have to live with a large uncertainty in subprocess cross section. We chose $Q^2 = {E_t}^2$ which is both a conventional choice, and a physically reasonable choice. Conventional, because it was chosen by UA2 in their structure function analysis [23]. Physically reasonable because ${E_t}^2$ characterizes the "scale" of the interaction, in the sense that parton interactions with higher E_t are less likely. There are, however, many other possible choices for Q^2 which have been used and can be made to agree with $\bar{p}p$ data by varying the value of the structure functions; afterall, only the product of structure functions and subprocess cross sections is measured.

A reasonable range of Q^2 is ${E_t}^2/4 < Q^2 < 4{E_t}^2$[10,74,75]. We use this range to bracket our systematic uncertainty in Q^2 when calculating systematic uncertainties in the extracted structure function. If $Q^2 = {E_t}^2/4$ then α_s is approximately 10% larger than it is when $Q^2 = {E_t}^2$; if $Q^2 = 4{E_t}^2$ then α_s is approximately 10% smaller. The resulting uncertainty in the extracted effective structure function is approximately the same but is in the opposite direction: if $Q^2 = {E_t}^2/4$ then $F(x)$ is everywhere within -11% of the mean result, and if $Q^2 = 4{E_t}^2$ then $F(x)$ is everywhere within +11% of the mean result. The resulting uncertainty in the extracted

gluon structure function is similar at low x but rises at high x: $G(x)$ is $\pm 14\%$ off the mean result at $x = 0.04$ and rises to $\pm 22\%$ off the mean result at $x = 0.3$.

As mentioned in Appendix A.1, the systematic uncertainty from the Q^2 scale is combined in quadrature with the systematic uncertainty from the effective angular distribution, to give the total theoretical systematic uncertainty in the effective structure function. The theoretical uncertainty, shown in figure 6.6, is small compared to the experimental uncertainty.

A.3 η_2 Resolution and $K_{t_\perp}$ Resolution

We have measured the $K_{t_\perp}$ resolution in the central calorimeters, and have estimated from that resolution a measurement of the η_2 resolution. The relation between the two resolutions was given in equation (5.5) of section 5.1 without proof or much discussion. Here is a simple derivation of that relation.

First, consider a two jet system with equal and opposite E_t vectors in the transverse plane. Then assume that the effects of calorimeter resolution and QCD radiation can be treated as a perturbation on the E_t and η_2 of that system. Then assume that the perturbation is azimuthally symmetric with respect to the jet axis, hence the perturbation which kicks a jet off its original axis produces the same rotation in the ϕ direction as it does in the θ direction, where θ and ϕ are the angles in spherical polar coordinates with the beam line as the z-axis. Then there are two possible momentum kicks that the second jet receives, one is the kick within the transverse plane, ΔP_{t_2}, and the other is the kick perpendicular to that plane, ΔP_{z_2}, which are equal by the assumption of azimuthal symmetry. The transverse momentum kick received by each jet of the two jet system should sum in quadrature to change the $K_{t_\perp}$ of the two jet system by a total of $\Delta K_{t_\perp}$, so the transverse momentum kick received by the second jet is given by

$$\Delta P_{t_2} = \frac{\Delta K_{t_\perp}}{\sqrt{2}} = \Delta P_{z_2} \tag{A.8}$$

Equation (A.8) contains the assumption of azimuthal symmetry of perturbations

with respect to the jet axis. Equation (A.8) also contains the assumption that the fluctuations in $K_{t_\perp}$ arise from independent fluctuations in each of the two jets which then sum in quadrature to give the total $\Delta K_{t_\perp}$ measured.

The relation between the η_2 resolution and the $K_{t_\perp}$ resolution is derived by considering the η_2 deviation, $\Delta\eta_2$, resulting from a transverse momentum deviation, ΔP_{t_2}, and a longitudinal momentum deviation, ΔP_{z_2},

$$\Delta\eta_2 = \sqrt{(\frac{\partial\eta_2}{\partial P_{t_2}})^2(\Delta P_{t_2})^2 + (\frac{\partial\eta_2}{\partial P_{z_2}})^2(\Delta P_{z_2})^2}. \tag{A.9}$$

Substituting the value of ΔP_{t_2} and ΔP_{z_2} from equation (A.8) into equation (A.9) gives

$$\Delta\eta_2 = \frac{\Delta K_{t_\perp}}{\sqrt{2}}\sqrt{(\frac{\partial\eta_2}{\partial P_{t_2}})^2 + (\frac{\partial\eta_2}{\partial P_{z_2}})^2}. \tag{A.10}$$

We can write η_2 as

$$\eta_2 = \frac{1}{2} ln \frac{P_2 + P_{z_2}}{P_2 - P_{z_2}} \tag{A.11}$$

and after performing the partial derivatives we have

$$\frac{\partial\eta_2}{\partial P_{t_2}} = -\frac{\tanh\eta_2}{P_{t_2}} \tag{A.12}$$

and

$$\frac{\partial\eta_2}{\partial P_{z_2}} = \frac{1}{P_{t_2}\cosh\eta_2}. \tag{A.13}$$

Substituting equation (A.12) and equation (A.13) into equation (A.10) and using a hyperbolic identity gives

$$\Delta\eta_2 = \frac{\Delta K_{t_\perp}}{\sqrt{2}\ P_{t_2}} \tag{A.14}$$

and with the $2 \rightarrow 2$ kinematic association $P_{t_2} = E_t$ equation (A.14) is the η_2 resolution relation given in equation (5.5) of section 5.1. Of course, this expression is intuitively obvious if one simplifies the argument by saying we are in effect using the ϕ resolution for the η resolution. Then, since $\Delta K_{t_\perp} \approx E_t \Delta\phi_{12}$ equation A.14 immediately follows from assuming the ϕ fluctuations for the two jets sum in quadrature.

This analysis measured the $K_{t_\perp}$ resolution in the central calorimeter, and used equation (5.5) of section 5.1 to relate this resolution to the η_2 resolution in

the central. The η_2 resolution in the plug and forward calorimetry was taken to be equal to the η_2 resolution in the central calorimetry. We assumed that QCD radiation and higher order processes are a larger effect on the η_2 resolution than is the roughly constant η segmentation of the calorimeter. This appears to be quite valid, because the η_2 resolution in the central is equivalent to a gaussian RMS deviation of about .1 for 50 GeV jets and we know from comparing the jet axis with the mean track axis that our experimental η resolution on the axis of a single jet is better than $2°(\sim 0.03$ units of pseudorapidity). Thus, the effects of QCD radiation must dominate the η_2 resolution, and the η_2 resolution should be similar at large $|\eta_2|$ and small $|\eta_2|$. In any case, this analysis uses very conservative bounds when estimating the uncertainty on the η_2 resolution function, and the systematic uncertainty in the cross section is not significantly increased. The uncertainty in the cross section due to the uncertainty in the jet E_t scale is around a factor of 10 larger than the uncertainty in the cross section due to the uncertainty in the η_2 resolution function.

Appendix B

Gas Gain

The basic measuring element of CDF gas calorimeters is the proportional tube. A charged particle passing through the tube ionizes the gas, freeing *primary electrons* to accelerate toward a central anode wire maintained at high voltage. These primary electrons become sufficiently energetic to ionize other atoms, freeing *secondary electrons* to do the same and thus creating an electron cascade. The ions created in this cascade drift radially outward away from the anode. These drifting ions induce a signal in the anode wire of the proportional tube and on the cathode pad of the proportional chamber. The integrated signal is proportional to the initial energy the charge particle deposited in the gas. The constant of proportionality is referred to as the gas gain.

The gain of a gas calorimeter is constant only if the density of the gas and the applied high voltage is constant. In a naive model [76], the gas gain, GG, is a function of fractional changes in the density $\Delta\rho/\rho$ and voltage $\Delta V/V$

$$GG = ae^{b\frac{\Delta V}{V}}e^{-c\frac{\Delta\rho}{\rho}} \tag{B.1}$$

where a, b, and c are positive constants. Thus, the gas gain increases when either the voltage increases, or the density of the gas decreases. Gas composition also affects the gas gain. The CDF calorimeters are maintained at a constant voltage, but the gas density is not controlled and fluctuates with atmospheric pressure and temperature. We monitor the changes in gas gain, produced primarily by changing

pressure and temperature, using proportional gas gain *monitoring tubes*. For CDF calorimeters and monitoring tubes $b \sim 20$ and $c \approx 9$ are good rules of thumb.

B.1 Gas Gain System

A schematic overview of the gas gain system is shown in figure B.1. The system can be roughly broken down into four stages: monitoring tubes on (or in) each calorimeter, electronics, data acquisition, and databasing and online calibration software.

B.1.1 Monitoring Tubes with ^{55}Fe Sources

CDF gas calorimeters used three kinds of monitoring tubes. All gas calorimeters used cylindrical aluminum monitoring tubes called BRD tubes. The BRD tubes were mounted in thermal contact with the calorimeters and within the gas flow to accurately reflect calorimeter gas temperature and pressure variations. Two BRD tubes were placed on each quadrant of the FEM, and two on each quadrant of the FHA, one on the gas inlet and one on the gas outlet of the chamber at shower maximum. A dozen BRD tubes were used by the PHA, and a few BRD tubes were used by the PEM. Each BRD tube was equipped with a temperature and pressure transducer to monitor gas temperature and pressure. A special *Gas Quality* system used a single BRD tube at constant temperature and pressure to monitor the entire gas supply inlet and detect gas composition changes. The Gas Quality system was upgraded in subsequent runs (1988) to feedback on the gas composition and maintain a stable gas composition.

In addition to BRD tubes, the PEM also used monitoring tubes within the calorimeter gas vessel (KEK tubes) of the same dimensions and material as the calorimeter's normal tubes. There were twenty-four KEK tubes inside each endplug, located around the perimeter of the gas volume at $|\eta| = 1.1$, spaced every 30° in ϕ, at two longitudinal depths. The PHA also used monitoring tubes of the same composition and dimensions as the calorimeter's normal tubes (LBL tubes),

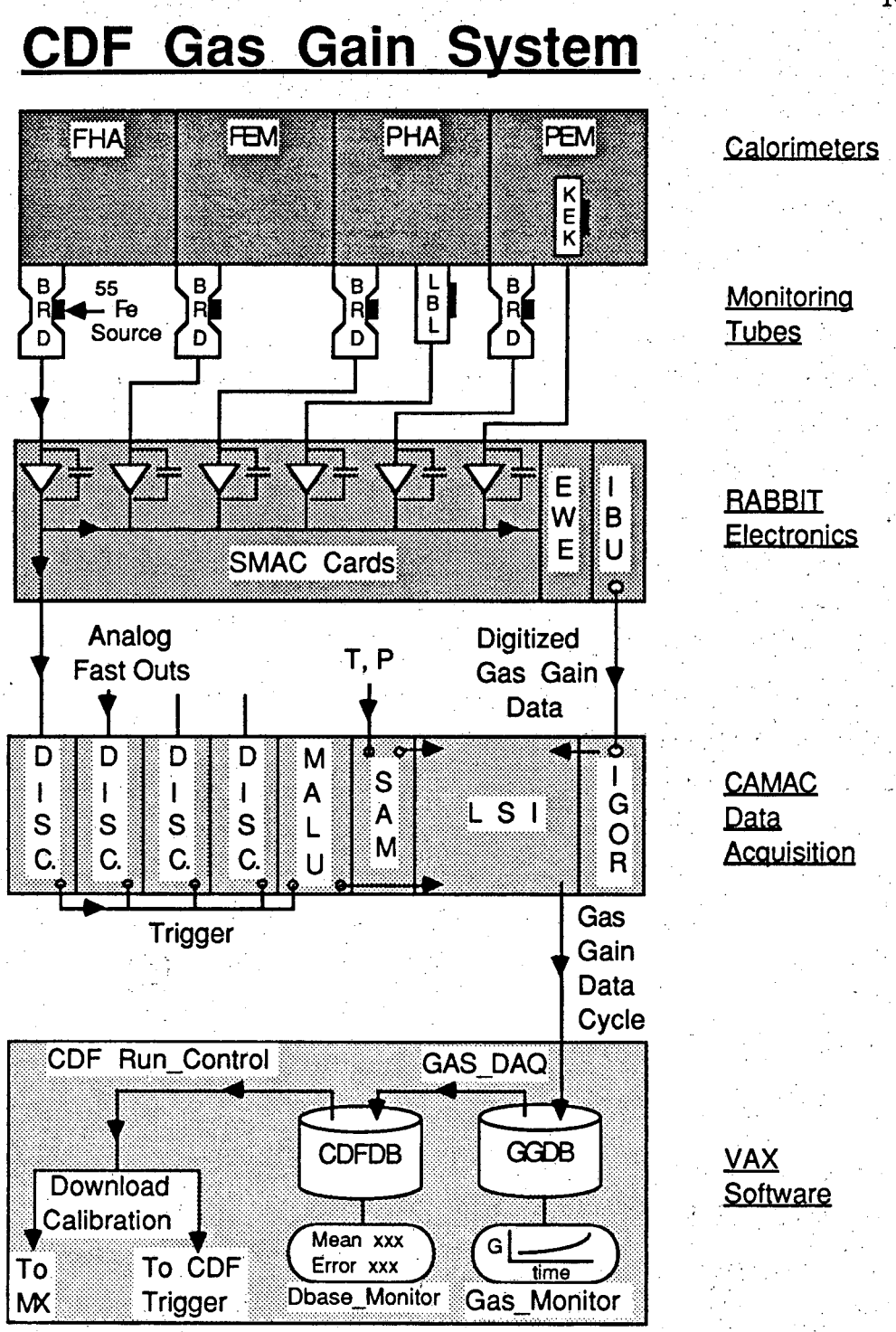

Figure B.1: Four stages of the CDF gas gain system are shown schematically. Gas gain monitoring tubes on (or in) gas calorimeters, electronics, data acquisition, and gas gain monitoring and calibration software.

shown in figure 3.8a. All monitoring tubes had gold plated tungsten wires of 50 μm diameter, the same wires as used by the gas calorimeters.

To produce a gas gain calibration signal of known energy, all tubes employed ^{55}Fe radioactive sources. A 6 KeV atomic x-ray, resulting from K-shell electron capture in the ^{55}Fe source, was completely absorbed by the gas in the monitoring tube. During the absorption process, the x-ray liberated approximately 200 primary electron-ion pairs. The probability of ionization was Poisson distributed, resulting in a gaussian peak with approximately 7% fractional width. We collected the signal from the resulting electron cascade, and fit the 6 KeV peak to a gaussian. The position of the peak was a measurement of the gas gain.

B.1.2 Electronics and Data Acquisition

The following paragraph is a brief description of the CDF gas gain electronics and data acquisition system; for full technical details see reference [77]. The ^{55}Fe source signal was integrated by a charge integrating amplifier in a SMAC (Source Monitoring Amplifier Card). The SMACs were in RABBIT crates (Redundant Analog Bus Based Information Transfer), located by the calorimeter in the collision hall. The integrated signal was split in two, half was sent to the trigger via analog outputs (Fast Out's) and half was delayed before being bussed to the EWE (an Analog to Digital Converter in the RABBIT crate). The delay provided time for the trigger to decide whether to read out the digitized signal. The trigger consisted of discriminators which received the Fast Out's, and a MALU (Majority Logic Unit), in CAMAC crates in the counting room. The MALU latched the input pattern from firing discriminators and set a LAM (Look At Me) in the CAMAC crate. An LSI processor, which was also the CAMAC crate controller, controlled the trigger and data acquisition. The LSI received the LAM, read the MALU hit pattern determining which tubes had received source signals, and commanded an IGOR (Input Gated/Output Register) module to fetch the digitized signal. The communication between CAMAC and RABBIT took place between the IGOR module in

the CAMAC crate and the IBU module in the RABBIT crate. The digitized signal was entered into a histogram in the LSI memory, one histogram per tube. The histograms, each containing about a thousand counts underneath the 6 KeV peak, were fit with a gaussian, and then refit out to 1.5 σ to obtain an accurate measurement of the mean. Every 15 minutes, four LSI's in four separate camac crates have accumulated and fit ^{55}Fe spectra for over 100 monitoring tubes, completing a single *gas gain data cycle.* In addition, temperature and pressure transducers located in the monitoring tubes, were read out by SAMs (Smart Analog Monitors) at the beginning and end of each gas gain data cycle. The gas gain data from the fit (gaussian mean, error on the mean, width, error on the width, number of bins, and chisquare) and the tube temperature and pressure were saved in the LSI awaiting transfer to the VAX cluster.

B.1.3 Databasing and Calibration Software

A menu driven computer program (GAS_DAQ), run on a VAX 750, downloaded instructions to the CAMAC based LSIs to begin and end gas gain data cycles or simply to cycle continuously. GAS_DAQ coordinated communication between the VAX and LSI, uploaded the results of a gas gain data cycle, and placed the data in the Gas Gain Data Base (GGDB). The GGDB [78] automatically stored gas gain data on disk, updated lists of the date and time of each gas gain data cycle, and updated strip charts of the gas gain as a function of time for each tube. A package of computer routines [79] allowed easy FORTRAN access to the data base. A user-friendly monitoring program (GAS_MONITOR), permitted quick listing of gas gain data from any date and time, and automatic histogramming and analysis of gas gain data between any two dates and times. When a new CDF physics data run was about to start, and new gas gain calibration constants were needed, GAS_DAQ calculated the new calibration from gas gain data stored in the GGDB. The calibration constants were placed in the CDF Data Base (CDFDB). The CDFDB saved calibration data as a function of CDF run number, while the

GGDB saved gas gain data as a function of time. The calibration constants were automatically fetched by Run_Control (the program which coordinated CDF online data acquisition) and were downloaded to the CDF trigger and the MX (a scanner which reads out calorimeter data from the front end electronics). The CDF trigger applied the calibrations to the calorimeter analog signals before triggering. The MX applied the calibrations to the calorimeter digitized signal, converting the measured charge directly into energy units before the data was written to tape.

B.2 Maintenance of Calibration

To maintain the test beam calibration of the gas calorimeters we related the calorimeter response to the response of monitoring tubes in the CDF collision hall. When each calorimeter was being calibrated in the test beam, there was also a gas gain monitoring tube present. Test beam measurements found a linear relation between the response of the calorimeter and the response of the test beam monitoring tube. To relate the response of the test beam monitoring tube to the response of a monitoring tube in the CDF collision hall, a series of relative *cross calibrations* were performed. Cross calibrations were needed to relate the test beam monitoring tube's intrinsic gain to the intrinsic gain of any tube. Other cross calibrations were needed to relate the gain of a test beam monitoring tube's electronics to the gain of any given tube's electronics. Using the measured relation between detector response and tube response, and using the cross calibrations relating total response from one tube to total response from another, we obtained a relation between the response of any given monitoring tube and the response of the calorimeter[80]. Measurements of the monitoring tube response were then used to maintain the test beam calibration of the gas calorimeters.

Studies of the monitoring tubes [81] indicated that during the 1987 run the gas gain system monitored endplug gas gain to within 3.5%. Thus an estimated 3.5% systematic uncertainty on the gas calorimeter absolute energy scale was expected from this source. Most of this systematic uncertainty can be contributed to the

many steps of the cross calibration procedure. The response of a given monitor tube generally *tracked* (correlated with) the response of another monitor tube to better than 1% over the course of the run. The response of a given monitor tube also tracked the inverse density to within about 2% (this larger variation possibly being caused by changes in gas composition as a function of time). If systematic variations due to cross calibration and changes in gas mixture are eliminated, the gas gain system monitors gains to within 1% or better.

Appendix C

Gas Calorimeter Energy Corrections

This appendix is a technical description of gas calorimeter energy corrections produced by this author and applied offline by the CDF collaboration.

C.1 Dead Wire Planes

During the 1987 run some of the wire planes in the gas calorimeters were dead. This resulted in a mismeasurement of the energy in the plug and forward calorimeters on the order of 10% for jets, with large quadrant to quadrant variations. A correction method was devised and a correction module (DEDWIR) was written to apply these run dependent corrections.

C.1.1 Tower Correction Algorithm

Define

Sector = 90 degree quadrant of PEM, FEM, FHA or 30 degree sector of PHA.

f_l = Fraction of sector energy deposited in lth wire plane on average.

$\{dl\}$ = Set of all dead layers in sector (no voltage on wire).

The simplest method of correcting TOWE was to use the average longitudinal energy profiles. The average longitudinal energy profiles were measured using 25 GeV jets (uncorrected E_t, cone radius of 0.6). In figure C.1, we show the average longitudinal profiles in percent versus layer number. These profiles were used to define f_l for the gas calorimeters. We corrected the energy of all towers within a sector by multiplying those towers by

$$Multiplier = \frac{1}{1 - \sum_{l=\{dl\}} f_l}$$

C.1.2 Wire Correction Algorithm

Define

$\{dc\}$ = Set of all dead electronic channels on wire cards for sector.

$E_{GS,pad}$ = Energy of gas spikes subtracted from sector towers by FILT_GAS.

P/W = Average pad over wire of sector.

E_{GS} = Energy of gas spikes in wires of sector= $\frac{E_{GS,pad}}{P/W}$.

E_l = Energy in wire plane l before corrections.

E'_l = Energy in wire plane l after corrections.

E_{good} = Sum of energy in good wire planes in sector before corrections.

$(E_{good} = \sum_{\substack{l \neq \{dl\} \\ l \neq \{dc\}}} E_l)$

Correcting the wire element banks was a bit more complicated. We had to account for dead wire planes, dead electronic channels on the wire cards, and gas spike energy in the wires; FILT_GAS subtracted this energy from the sector pads. If the wire plane was not HV dead and not electronically dead (good layers) we replaced the layer energy in the appropriate wire element bank with:

$$E'_l = E_l - (\frac{E_l}{E_{good}})E_{GS}$$

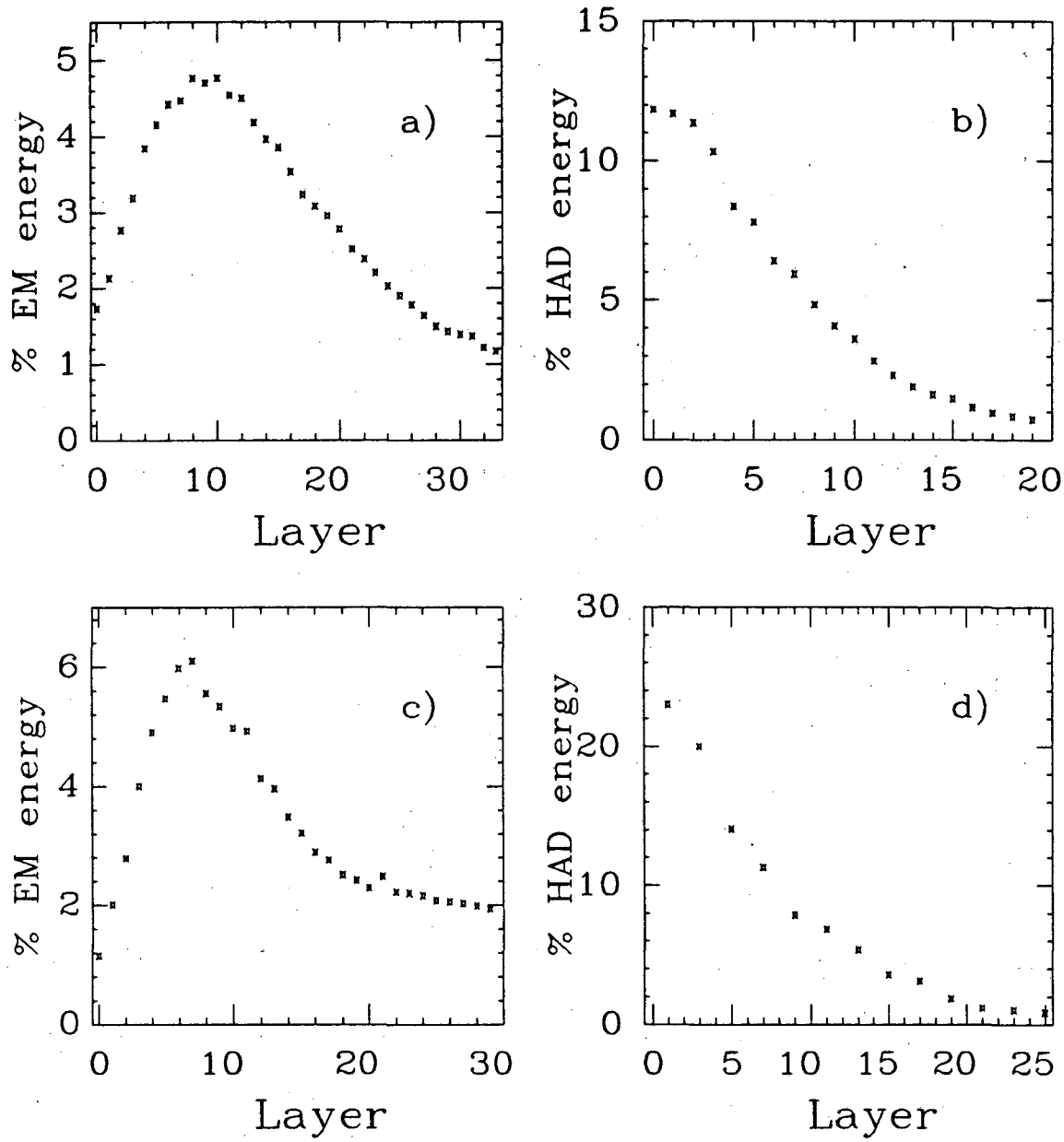

Figure C.1: Average longitudinal energy profiles for each of the four gas calorimeters: **a)** PEM, **b)** PHA, **c)** FEM, **d)** FHA. The vertical axis is the average percent of total anode energy deposited in that calorimeter by jets with 25 GeV total E_t. The horizontal axis is the gas proportional layer number.

If the wire plane was HV dead or electronically dead ($l \in \{dl\} or \{dc\}$) we replaced the layer energy in the appropriate wire element bank with:

$$E_l' = \frac{(E_{good} - E_{GS}) f_l}{(1 - \sum_{\substack{l=\{dl\} \\ l=\{dc\}}} f_l)}$$

The original version of DEDWIR did wire corrections for endplug calorimeters only.

C.2 PHA Sector Response Map

As described in section 3.3.2, all the PHA pads were initially calibrated with radioactive sources. From these pad response maps, tower response maps were calculated by averaging the response of the twenty pads in a tower. From the tower response maps sector response maps were calculated by averaging the forty inner towers of a PHA sector. The response of the thirty-two towers on the boundary of a PHA sector were not used, a more detailed study of PHA response would have to include the response of these towers as well as losses in the cracks between sectors. The average response of the twenty-four PHA sectors is listed in table C.1. The response is normalized to a nine tower average of the source response about the standard tower used to set the PHA energy scale (sector 0, row 8, column 4). The error listed is a statistical error, the RMS deviation of the forty tower responses divided by $\sqrt{40}$. The sectors were intentionally arranged with only slight variations in response between adjacent sectors, however the sectors on the west (0-11) have lower average response than the sectors on the east (12-23). This response map was available in the software module CALORIMETRY to correct the energy of PHA towers.

Sector	Response	Error
0	0.990	.007
1	1.003	.005
2	0.991	.005
3	0.971	.005
4	0.975	.005
5	0.978	.005
6	0.941	.005
7	0.969	.005
8	0.900	.005
9	0.889	.005
10	0.858	.005
11	0.825	.005
12	1.191	.006
13	1.115	.005
14	1.106	.005
15	1.098	.005
16	1.083	.004
17	0.992	.007
18	1.050	.005
19	0.987	.005
20	1.011	.006
21	1.036	.005
22	1.041	.005
23	1.069	.005

Table C.1: PHA sector mean response to Cd^{109} sources.

Bibliography

[1] M. Banner *et al.*, *Observation of Very large Transverse Momentum Jets at the CERN $\bar{p}p$ Collider*, Phys. Lett. **118B**(1982)203.

[2] G. Arnison *et al.*, *Observation of Jets in High Transverse Energy Events at the CERN Proton Antiproton Collider*, Phys. Lett. **123B**(1983)115.

[3] The parton model is described at length by its originator R. P. Feynman in Photon-Hadron Interactions, Published by W. A. Benjamin, 1972. Some applications of the parton model to hadronic reactions were introduced by S. M. Berman, J. D. Bjorken, and J. B. Kogut in *Inclusive Processes at High Transverse Momentum*, Phys. Rev. **D4**(1971)3388.

[4] The original reference for QCD is H. Fritzsch, M. Gell-Mann and H. Leutwyler, *Advantages of The Color Octet Gluon Picture*, Phys. Lett. **B47**(1973)365. The perturbative approach to QCD has been reviewed by many authors including E. Reya, *Perturbative Quantum Chromodynamics*, Phys. Reports **69C**(1981)195.

[5] G. Altarelli and G. Parisi, *Asymptotic Freedom in Parton Language*, Nucl. Phys. **B126**(1977)298.

[6] For a review see J. Drees and H. E. Montgomery, *Muon Scattering*, Ann. Rev. of Nucl. Part. Sci. **33**(1983)383. Also, F. Eisele, *Structure Functions*, Journal De Physique, Colloque C3, **43**(1982)337.

[7] F. Abe, et al., *Measurement of the Inclusive Jet Cross Section in $\bar{p}p$ Collisions at $\sqrt{s} = 1.8$ TeV*, Phys. Rev. Lett. **62**(1989)613.

[8] M. Gell-Mann, *A Schematic Model of Baryons and Mesons*, Phys. Lett. **8**(1964)214.

[9] The *standard model* is a combination of the QCD description of the strong interactions and the Glashow-Weinberg-Salam theory description of electroweak interactions. S.L. Glashow Nucl. Phys. **22**(1961)579, and S. Weinberg Phys. Rev. Lett. **19**(1967)1264, and A. Salam in Elementary Particle Theory: Relativistic Groups and Analyticity (Nobel Symposium No. 8), edited by N. Svartholm (Almqvist and Wiksell, Stockholm), 1968, p. 367.

[10] E. Eichten, I. Hinchliffe, K. Lane and C. Quigg, *Supercollider Physics*, Rev. of Mod. Phys. **56**(1984)579.

[11] D. W. Duke and J. F. Owens, *Q^2-dependent parametrizations of parton distribution functions*, Phys. Rev. **D30**(1984)49.

[12] M. Diemoz, F. Ferroni, E. Longo and G. Martinelli, *Parton Densities from Deep Inelastic Scattering to Hadronic Processes at Super Collider Energies*, Z. Phys. **C39**(1988)21.

[13] A. D. Martin, R. G. Roberts and W. J. Sterling, *Structure-function analysis and ψ, jet, W, and Z production: Determining the gluon distribution*, Phys. Rev. **D37**(1988)1161.

[14] An example of how the gluon distribution is extracted from DIS data is given by H. Abramowicz, *et al.*, *Determination of the Gluon Distribution in the Nucleon from Deep Inelastic Neutrino Scattering*, Z. Phys. **C12**(1982)289.

[15] Particle Data Group, *Review of Particle Properties*, Phys. Lett. **B204**(1988), page 96.

[16] R. P. Feynman, Quantum Electrodynamics, Benjamin/Cummings, 1961.

[17] D.J. Gross and F. Wilczek, *Ultraviolet Behavior of Non-Abelian Gauge Theories*, Phys. Rev. Lett. **30**(1973)1343 and H.D. Politzer, *Reliable Perturbative Results for Strong Interactions?*, Phys. Rev. Lett. **30**(1973)1346.

[18] B. L. Combridge, J. Kripfganz and J. Ranft, *Hadron Production at Large Transverse Momentum and QCD*, Phys. Lett. **70B**(1977)234.

[19] J. F. Owens , *Direct Photon Production*, Rev. of Mod. Phys. **59**(1987)465, page 499.

[20] B. Combridge and C. Maxwell , *Untangling Large-P_T Hadronic Reactions*, Nucl. Phys. **B239**(1984)429, pages 442-444. Also see F. Halzen and P. Hoyer , *Jets in $\bar{p}p$ collider Events: Systematic Tests of the Hard Scattering Picture*, Phys. Lett. **130B**(1983)326.

[21] This can be seen from a comparison of the lowest order QCD predictions to the two jet $\cos\theta^*$ distribution in F. Abe *et. al*, *Dijet Angular Distributions from $\bar{p}p$ Collisions at $\sqrt{s} = 1800$ GeV.*, Phys. Rev. Lett. **62**(1989)3020.

[22] G. Arnison *et al.*, *Angular Distributions and Structure Functions from Two-Jet events at the CERN SPS $p\bar{p}$ Collider*, Phys. Lett. **136B**(1984)294.

[23] P. Bagnaia *et al.*, *Measurement of Jet Production Properties at the CERN $p\bar{p}$ Collider*, Phys. Lett. **144B**(1984)283.

[24] F. Abe *et al.*, *The CDF Detector: An Overview*, Nucl. Inst. and Meth. **A271**(1988)387.

[25] L. Balka *et al.*, *The CDF Central Electromagnetic Calorimeter*, Nucl. Inst. and Meth. **A267**(1988)351.

[26] T. Kamon *et al.*, *A New Scintillator and Wavelength Shifter*, Nucl. Inst. and Meth. **213**(1983)261.

[27] T. Devlin *et al.*, *Phototube Testing for CDF*, Nucl. Inst. and Meth. **A268**(1988)24.

[28] R. G. Wagner *et al.*, *Cosmic Ray Test of the CDF Central Calorimeters*, Nucl. Inst. and Meth. **A267**(1988)330.

[29] S. R. Hahn *et al.*, *Calibration Systems for the CDF Central Calorimeter*, Nucl. Inst. and Meth. **A267**(1988)351.

[30] S. Bertolucci *et al.*, *The CDF Central and Endwall Hadron Calorimeter*, Nucl. Inst. and Meth. **A267**(1988)301.

[31] J. Huth, *Jet Energy Measurement: CDF experience*, paper presented at the SSC Workshop on Calorimetry for the Super Collider March 13-17, 1989.

[32] R. Wigmans, *On The Energy Resolution of Uranium and Other Hadron Calorimeters*, Nucl. Inst. and Meth. **A259**(1987)389.

[33] P. Kesten and J. Proudfoot, *The CDFDB, a Reference Manual for the CDF Database*, CDF Note 473, 1987.

[34] A. Baden, *The CDF Calorimetry Module*, CDF Note 569, 1987.

[35] S. Behrends and S. Kuhlmann, *Checks of the CDFSIM Central Calorimeter Simulation*, CDF Note 684, 1988.

[36] Y. Fukui *et al.*, *CDF End Plug Electromagnetic Calorimeter Using Conductive Plastic Proportional Tubes*, Nucl. Instrum. Meth. **A267**(1988)280.

[37] C. Haber, *Hadronic Energy Calibration of the Endplug Calorimeters*, LBL/CDF 87-02, 1987.

[38] W. C. Carithers *et al.*, *Resistive Plastic Cathode Pad Readout Proportional Mode Chambers for CDF*, and W. C. Carithers *et al.*, *Performance and Calibration Studies of the CDF Endplug Calorimeter*, in Proceedings of the Gas Sampling Calorimetry Workshop II, Fermilab, 1985.

[39] M. E. B. Franklin, *Performance of the Gas Calorimetry at CDF*, in Proceedings of the 7th Topical Workshop on Proton-Antiproton Collider

Physics, June 1988, edited by R. Raja, A. Tollestrup, and J. Yoh (World Scientific). Also see, S. Cihangir *et al.*, *Neutron Induced Pulses in CDF Forward Hadron Calorimeters*, CDF Note 810, submitted to IEEE Symposium in Orlando, Florida, November, 1988.

[40] R. Drucker, *A Source Response Map Correction for the PHA*, CDF Note 973, 1989.

[41] J. S. T. Ng, *Gas Calorimetry Energy Scale Cross Calibration Using Texas Towers*, CDF Note 968, 1989.

[42] G. Brandenburg *et al.*, *An Electromagnetic Calorimeter for the Small Angle Regions of the Collider Detector at Fermilab*, Nucl. Instrum. Meth. **A267**(1988)257.

[43] S. Cihangir *et al.*, *The CDF Forward/Backward Hadron Calorimeter*, Nucl. Instrum. Meth. **A267**(1988)249.

[44] F. Snider *et al.*, *The CDF Vertex Time Projection Chamber System*, Nucl. Instrum. Meth. **A268**(1988)75.

[45] F. Bedeschi *et al.*, *Design and Construction of the CDF Central Tracking Chamber*, Nucl. Instrum. Meth. **A268**(1988)75.

[46] S. Behrends *et al.*, *Response of the Central Calorimeter to Low-Energy Charged Particles*, CDF Note 583, 1987.

[47] S. Kuhlmann, S. Behrends, J. Huth, B. Hubbard, and A. F. Garfinkel, *Central Jet Energy/Momentum Corrections*, CDF Note 686, 1988.

[48] D. Amidei *et al.*, *A Two Level FASTBUS Based Trigger System for CDF*, Nucl. Instrum. Meth. **A269**(1988)51.

[49] T. Liss, *Luminosity Monitoring and Beam-Beam Counter Performance*, CDF Note 552, 1988.

[50] M. M. Block and R. N. Cahn, *Fits To High Energy pp and $\bar{p}p$ Total Cross Sections and ρ Values*, Phys. Lett. **188B**(1987)143.

[51] M. Bozzo *et al.* (UA4 Collaboration), *Measurement of the Proton-Antiproton Total and Elastic Cross Sections at the CERN SPS Collider*, Phys. Lett. **147B**(1984)392.

[52] R. E. Ansourge *et al.* (UA5 Collaboration), *Diffraction Dissociation at the CERN Pulsed $p\bar{p}$ Collider at c.m. Energies of 900 and 200 GeV*, Z. Phys. **C33**(1986)175.

[53] G. Drake *et al.*, *CDF Front End Electronics: The RABBIT System*, Nucl. Instrum. Meth. **A269**(1988)68.

[54] E. Barsotti *et al.*, *FASTBUS Data Acquisition for CDF*, Nucl. Instrum. Meth. **A269**(1988)82.

[55] S. Kuhlmann, S. Hahn and Y. Tsay, *Run List for the Inclusive Jet Cross Section*, CDF Note 710, 1988.

[56] D. Brown, *A Search for Double Parton Interactions in* 1.8 *TeV Proton-Antiproton Collisions*, Ph.D Thesis, Harvard University, 1989.

[57] S. Kuhlmann and J. Yoh, *Filtering Jet Backgrounds in the CDF Central Detector*, CDF Note 548, 1987.

[58] G. Redlinger and Y. D. Tsay, *The Hadron TDC Filter for Main Ring And Cosmic Ray Events*, CDF Note 521, 1987.

[59] P. Hurst and M. E. B. Franklin, *Cable Noise Filter Description: PHA*, CDF Note 847, 1988.

[60] D. Brown and M. E. B. Franklin, *FILT_GAS*, CDF Note 696, 1988.

[61] D. Brown *et al.*, *Clustering algorithms and their performance*, CDF Note 605, 1988.

[62] S. Kuhlmann, Ph.D. Thesis, Purdue University, 1988.

[63] B. Flaugher and S. Kuhlmann, *Underlying Event Energy in Clusters*, CDF Note 685, 1988.

[64] S. Kuhlmann, *Central Jet Energy Corrections Due To Clustering Effects*, CDF Note 687, 1988.

[65] F. Paige and S. Protopopescu, in Proceedings of the Summer Study on the Physics of the Superconducting Supercollider,Snowmass, CO, 1986, edited by R. Donaldson and J. Marx, p. 320.

[66] R. D. Field and R. P. Feynman, *A Parametrization of the Properties of Quark Jets*, Nucl. Phys. **B136**(1978)1.

[67] D. Brown, S. Kannappan and M. Shapiro, *QFL Version 2: Improvements and Checks*, CDF Note 753, 1988.

[68] R. Carey, *Angular Distributions of Three Jet Events in Proton-Antiproton Collisions at the Fermilab Tevatron*, Ph.D Thesis, Harvard University, 1989.

[69] P. Bagnaia *et al.*, *Measurement of Production and Properties of Jets at the CERN $\bar{p}p$ Collider*, Z. Phys. **C20**(1983)117.

[70] R. St. Denis, *Dijet Angular Distributions in Proton-Antiproton Collisions at the Fermilab Tevatron*, Ph.D Thesis, Harvard University, 1988.

[71] J. Orear, *Notes on Statistics for Physicists, Revised*, Cornell Laboratory for Nuclear Studies note: CLNS 82/511, 1982.

[72] J. Huth and S. Behrends, *Statistics Issues for the Inclusive Jet E_t Paper*, CDF Note 747, 1988.

[73] F. James and M. Roos, *'MINUIT' A System For Function Minimization and Analysis of the Parameter Errors and Correlations*, Computer Physics Communications **10**(1975)343.

[74] A. D. Martin, R. G. Roberts and W. J. Sterling, *Benchmark Cross Sections for $p\bar{p}$ Collisions at 1.8 TeV*, Z. Phys. **C42**(1989)277.

[75] S. D. Ellis, Z. Kunszt, and D. E. Soper, *One-Jet Inclusive Cross Section at Order $\alpha_s{}^3$: Gluons Only*, Phys. Rev. Lett. **62**(1989)726.

[76] W. Carithers, *Primer on Models for Gas Gain in Proportional Tubes*, CDF/LBL Note 87-01, 1987.

[77] L. DeMortier, *The CDF Gas Gain Data Acquisition System*, CDF Note 533, 1988.

[78] R. M. Harris, *A description of the Gas Gain Data Base (GGDB)*, CDF Note 435, 1986.

[79] R. M. Harris, *GGDB Utility User's Guide and Programmers Reference Manual*, CDF Note 436, 1986.

[80] M. Gold and J. Siegrist, *Gas Calorimeter Energy Scale*, CDF/LBL Note 87-02, 1987.

[81] A. Barbaro-Galtieri, *CDF Calorimeters: Studies Of Gas Gain Using The Monitoring Tubes*, CDF Note 551, 1987.

LAWRENCE BERKELEY LABORATORY
TECHNICAL INFORMATION DEPARTMENT
1 CYCLOTRON ROAD
BERKELEY, CALIFORNIA 94720